



UNDERGRADUATE PROJECT REPORT

Project Title:	Solar Panel Anomaly Classification using SARNet Model
Surname:	Li
First Name:	Xiang
Student Number:	202118010105
Supervisor Name:	Dr Grace Ugochi Nneji
Module Code:	CHC 6096
Module Name:	Project
Date Submitted:	May 6, 2025

Chengdu University of Technology Oxford Brookes College

Chengdu University of Technology

BSc (Single Honours) Degree Project

Programme Name: Computer Science

Module No.: CHC 6096

Surname: Li

First Name: Xiang

Project Title: Solar Panel Anomaly Classification using SARNet Model

Student No.: 202118010105

Supervisor: Dr Grace Ugochi Nneji

Declaration

Student Conduct Regulations:

Please ensure you are familiar with the regulations in relation to Academic Integrity. The University takes this issue very seriously and students have been expelled or had their degrees withheld for cheating in assessment. It is important that students having difficulties with their work should seek help from their tutors rather than be tempted to use unfair means to gain marks. Students should not risk losing their degree and undermining all the work they have done towards it. You are expected to have familiarized yourself with these regulations.

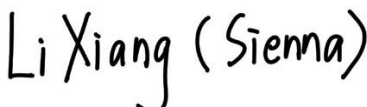
<https://www.brookes.ac.uk/regulations/current/appeals-complaints-and-conduct/c1-1/>

Guidance on the correct use of references can be found on www.brookes.ac.uk/services/library, and also in a handout in the Library.

The full regulations may be accessed online at
<https://www.brookes.ac.uk/students/sirt/student-conduct/>

If you do not understand what any of these terms mean, you should ask your Project Supervisor to clarify them for you.

I declare that I have read and understood Regulations C1.1.4 of the Regulations governing Academic Misconduct, and that the work I submit is fully in accordance with them.


Signature Date6th May 2025.....

REGULATIONS GOVERNING THE DEPOSIT AND USE OF OXFORD BROOKES UNIVERSITY MODULAR PROGRAMME PROJECTS AND DISSERTATIONS

Copies of projects/dissertations, submitted in fulfillment of Modular Programme requirements and achieving marks of 60% or above, shall normally be kept by the Oxford Brookes University Library.

I agree that this dissertation may be available for reading and photocopying in accordance with the Regulations governing the use of the Oxford Brookes University Library.

Li Xiang (Sienna)

Signature

Date 6th May 2025.....

Acknowledgment

I would like to express my heartfelt gratitude to my supervisor, Dr. Grace Ugochi Nneji, whose unwavering support and expert guidance were invaluable throughout my research on applying deep learning to classify anomalies in solar panels using infrared and electroluminescence images. Her insightful feedback and meticulous attention to detail greatly enriched the quality of my work and helped me navigate the challenges of this project with clarity and confidence.

I am also deeply thankful to Mr. Joojo Walker, my Module Leader, for his invaluable assistance during the course of this project. While his teaching laid the foundation for academic development, it was his guidance on the structure, clarity, and academic rigor of my dissertation that truly made a difference. His advice greatly supported my writing process and helped ensure the coherence and quality of my final report.

My sincere appreciation also goes to Chengdu University of Technology and Oxford Brookes University for providing the academic platform, resources, and a stimulating learning environment that made this project possible. The interdisciplinary exposure and institutional support I received from both universities were fundamental to the completion of this work.

Lastly, I am profoundly grateful to my family and friends for their constant encouragement, patience, and understanding. Their emotional support and belief in my abilities have been a source of strength and motivation throughout this journey.

Table of Contents

Declaration	iii
Acknowledgment.....	v
Table of Contents	vi
List of Figures	ix
List of Tables	i
Abstract.....	ii
Abbreviations.....	iii
Glossary.....	v
Chapter 1 Introduction	8
1.1 Background	8
1.1.1 Risk and Factor	9
1.1.2 Challenge	10
1.2 Aim	11
1.3 Objectives	11
1.4 Project Overview	12
1.4.1 Scope	12
1.4.2 Audience	14
Chapter 2 Background Review	15
2.1 Solar Panel Anomaly Classification Using Traditional Methods	15
2.2 Solar Panel Anomaly Classification Using Machine Learning Technologies	16
2.3 Solar Panel Anomaly Classification Using Deep Learning Technologies	18
2.3.1 CNN Methods	18
2.3.2 Attention Mechanism	19
2.3.3 Hybrid Attention-CNN Methods	20
Chapter 3 Methodology	25
3.1 Approach	25
3.2 Dataset	25
3.2.1 Dataset 1 – Infrared Solar Modules	25
3.2.2 Dataset 2 - Electroluminescence Photovoltaic (ELPV)	27
3.3 Data Preprocessing	28

3.3.1	Data Split.....	29
3.3.2	Data Balancing	31
3.3.3	Data Resize	32
3.3.4	Data Augmentation.....	32
3.4	Proposed Model Structure.....	33
3.4.1	StackNet.....	33
3.4.2	ResoNet (Resolution-aware module).....	34
3.4.3	Attention Mechanism- Squeeze and Excitation (SE) module	36
3.4.4	SRNet (StackNet-ResoNet Model).....	36
3.4.5	SARNet (StackNet-Attention Mechanism-ResoNet Model).....	39
3.5	Experimental Setup & Technology	42
3.5.1	Experimental Setup	42
3.5.2	Technology	42
3.6	Model Performance Evaluation Metrics	43
3.6.1	Loss Function	43
3.6.2	Accuracy	43
3.6.3	Specificity (SP)	44
3.6.4	Sensitivity/Recall (SE)	44
3.6.5	Precision	44
3.6.6	F1 Score (Dice Score)	44
3.6.7	Confusion Matrix	44
3.6.8	Receiver Operating Characteristic (ROC)	45
3.6.9	Precision-Recall (PR)	45
3.7	Project Version Management	45
Chapter 4 Implementation and Result.....		46
4.1	Experiment 1 - StackNet.....	46
4.1.1	StackNet on Dataset 1- Binary Class	46
4.1.2	StackNet on Dataset 1- 6-Class	50
4.1.3	StackNet on Dataset 2- Binary Class	53
4.2	Experiment 2 - SRNet	57
4.2.1	SRNet on Dataset 1- Binary Class	57
4.2.2	SRNet on Dataset 1- 6-Class	61
4.2.3	SRNet on Dataset 2- Binary Class	65

4.3	Experiment 3 - SARNet.....	69
4.3.1	SARNet on Dataset 1- Binary Class	69
4.3.2	SARNet on Dataset 1- 6-Class	72
4.3.3	SARNet on Dataset 2- Binary Class	75
4.4	Current Experiments Results Summary	80
4.5	Model Explainability	84
4.6	Model Visualization - GUI Design	88
Chapter 5 Professional Issues		92
5.1	Project Management	92
5.1.1	Activities	92
5.2	Schedule	94
5.2.1	Project Data Management	95
5.2.2	Project Deliverables	95
5.3	Risk Analysis	95
5.4	Professional Issues	96
5.4.1	Legal Issues	96
5.4.2	Social Issues	96
5.4.3	Ethical Issues	97
5.4.4	Environment Issues	97
Chapter 6 Conclusion		98
References		100

List of Figures

Figure 1. Factors of Solar Panel Anomaly	10
Figure 2. Project overview	13
Figure 3. Categories of solar panel anomaly classification traditional methods.....	15
Figure 4. Madani et al.[15] decision tree (DT) with AdaBoost algorithm.....	16
Figure 5. RK-RF Algorithm Flowchart by Dhibi et al. [16]	17
Figure 6. Yi and Etemadi [17] Algorithm Based on SVM.....	18
Figure 7. ResNet structure by Le et al.[19]	19
Figure 8. Park et al. [29] mentioned attention Mechanism.....	20
Figure 9. Lee et al.[21] proposed model 's overall AGDM detection process	21
Figure 10. Few sample categories in the Infrared Solar Modules Dataset.....	27
Figure 11. The distribution of the PV cells per class in the original ELPV dataset.....	28
Figure 12. Selected EL images (from the ELPV dataset)	28
Figure 13. Data separation of dataset 1 (Binary Classification)	29
Figure 14. Data separation of dataset 1 (6-Class Classification)	30
Figure 15. Data separation of dataset 2 (4-Class Classification).....	30
Figure 16. Balanced Data of Dataset 1 (Binary Classification).....	31
Figure 17. Balanced Data of Dataset 1 (6-Class Classification).....	31
Figure 18. Balanced Data of Dataset 2 (Binary Classification).....	32
Figure 19. Residual block structure diagram for each stage	34
Figure 20. The proposed StackNet Structure	34
Figure 21. The Architecture of ResoNet.....	35
Figure 22. Attention Mechanism- Squeeze and Excitation (SE) module	36
Figure 23. The Improved Residual Block Incorporating ResoNet.....	37
Figure 24. Overview of SRNet Structure	38
Figure 25. ResoNet Combined SE Block (Updated ResoNet)	39
Figure 26. The Enhanced Residual Block Incorporating ResoNet and SE Block	40
Figure 27. Overall Architecture of the SARNet.....	41
Figure 28. (a) and (b) present StackNet model Accuracy and Loss Curve on Dataset 1 (Binary Class)	47
Figure 29. StackNet model Confusion Matrix for Dataset 1- Binary Class	48
Figure 30. (c) present StackNet model ROC Curve on Dataset 1- Binary Class	49
Figure 31. (d) present PR Curve on Dataset 1- Binary Class	50
Figure 32. (e) and (f) present StackNet model Accuracy and Loss Curve on Dataset 1 (6-Class)	51
Figure 33. StackNet model Confusion Matrix for Dataset 1(6-calss).....	51
Figure 34. (g) present StackNet model ROC Curve on Dataset 1(6-Class).....	52
Figure 35. (h) present StackNet model PR Curve on Dataset 1(6-Class).....	53
Figure 36. (i) and (j) present StackNet model Accuracy and Loss Curve Dataset 2	54
Figure 37. StackNet model Confusion Matrix for Dataset 2(Binary Class)	54
Figure 38. (k) present StackNet model ROC Curve on Dataset 2(Binary Class)	55
Figure 39. (l) present StackNet model PR Curve on Dataset 2(Binary Class).....	56
Figure 40. (m) and (n) present SRNet model ' s Accuracy and Loss Curve on Dataset 1 (Binary Class)	58
Figure 41. SRNet Model Confusion Matrix for Dataset 1- Binary Class	59
Figure 42. (o) present SRNet model ROC and PR Curve on Dataset 1(Binary Class)..	60
Figure 43. (p) present SRNet model ROC and PR Curve on Dataset 1(Binary Class)..	61
Figure 44. (q) and (r) present SRNet model ' s Accuracy and Loss Curve on Dataset 1	62
Figure 45. SRNet Model Confusion Matrix for Dataset 1(6-Class).....	63

Figure 46. (s) present SRNet model ROC Curve on Dataset 1(6-Class)	64
Figure 47. (t) present SRNet model ROC and PR Curve on Dataset 1(6-Class).....	65
Figure 48. (u) and (v) present SRNet model ’ s Accuracy and Loss Curve on Dataset 2 (Binary Class).....	66
Figure 49. SRNet Model Confusion Matrix for Dataset 2- Binary Class	66
Figure 50. (w) present SRNet model ROC Curve on Dataset 2(Binary Class).....	67
Figure 51. (x) present SRNet model PR Curve on Dataset 2(Binary Class).....	68
Figure 52. (y) and (z) present SARNet model Accuracy and Loss Curve on Dataset1 (Binary Class).....	70
Figure 53. SARNet model Confusion Matrix for Dataset 1- Binary Class	70
Figure 54. (aa) present SARNet model ROC Curve on Dataset 1- Binary Class	71
Figure 55. (bb) present SARNet model PR Curve on Dataset 1- Binary Class	72
Figure 56. (cc) and (dd) present SARNet model Accuracy and Loss Curve on	73
Figure 57. SARNet model Confusion Matrix for Dataset 1(6-Class).....	73
Figure 58. (ee) present SARNet model ROC Curve on Dataset 1(6-Class)	74
Figure 59. (ff) present SARNet model PR Curve on Dataset 1(6-Class)	75
Figure 60. (gg) and (hh) present SARNet model Accuracy and Loss Curve on Dataset 2 (Binary Class).....	76
Figure 61. SARNet model Confusion Matrix for Dataset 2-Binary Class	77
Figure 62.(ii) present SARNet model ROC Curve on Dataset 2- Binary Class	78
Figure 63. (jj) present SARNet model PR Curve on Dataset 2- Binary Class	79
Figure 64. Grad-CAM Visualization of Dataset 1 Binary class (Anomaly)	85
Figure 65. Grad-CAM Visualization of Dataset 1 Binary class (No-Anomaly)	85
Figure 66. Grad-CAM Visualization of Cell	86
Figure 67. Grad-CAM Visualization of Cracking	86
Figure 68. Grad-CAM Visualization of Diode	86
Figure 69. Grad-CAM Visualization of Offline-Module	87
Figure 70. Grad-CAM Visualization of Shadowing	87
Figure 71. Grad-CAM Visualization of Vegetation	87
Figure 72. Grad-CAM Visualization of Dataset 2 Binary class (Anomaly)	88
Figure 73. Instruction of the website part of Home page	89
Figure 74. Project Introduction part of Home page	89
Figure 75. Overview of model prediction page	90
Figure 76. Prediction example	91
Figure 77. Schedule Plan	94
Figure 78. The local folder structure	95

List of Tables

Table 1. Summary of Related Works	21
Table 2. Described each class in Infrared Solar Module Dataset	25
Table 3. Summary of Relevant Technology involved in this project	42
Table 4. Outcomes of Confusion Matrix	45
Table 5. StackNet Model Performance Metrics-1	56
Table 6. StackNet Model Performance Metrics-2	57
Table 7. SRNet Model's Performance Metrics-1	68
Table 8. SRNet Model's Performance Metrics-2	69
Table 9. SARNet Model's Performance Metrics-1	79
Table 10. SARNet Model's Performance Metrics-2	80
Table 11. Compare models' Performance Metrics-1	81
Table 12. Compare models' Performance Metrics-2	82
Table 13. Relevant Activities	92
Table 14. Risk Analysis	96

Abstract

Solar panel faults can significantly reduce energy output and reliability in renewable energy systems. Traditional fault detection methods often rely on manual inspection or rule-based systems, which struggle with accuracy and scalability. This project introduces a deep learning-based fault diagnosis system designed to automatically detect and classify solar panel anomalies using image data from two public datasets—*infrared (IR)* and *electroluminescence (EL)* images. This proposed SARNet model integrates StackNet, ResoNet and attention mechanisms to enable deep, multi-scale, and context-aware feature extraction. The model was trained and evaluated on IR images for both binary (fault and no-fault) and multi-class (six fault types) classification, as well as on the ELPV dataset for binary fault detection (fault and no-fault). Experimental results demonstrate high diagnostic performance: 91.7% accuracy and 91.4% F1-score on IR binary classification; 81.63% accuracy on IR multi-class classification; and 89.1% accuracy on binary classification of ELPV dataset. These outcomes validate the model's robustness across different imaging modalities and fault scenarios. A lightweight, web-based GUI was also developed, enabling real-time image upload and diagnosis. This bridges the gap between research and field application, offering practical deployment potential for solar maintenance. In summary, this project highlights the effectiveness of combining deep learning and attention mechanisms for reliable solar panel fault detection, contributing to more intelligent and automated renewable energy management.

Keywords: *Solar Panel Fault Detection, Deep Learning, Infrared Imaging, Electroluminescence Imaging, Renewable Energy, Attention Mechanism, ResNet-Inception, Image Classification*

Abbreviations

CNN	Convolutional Neural Network
DL	Deep Learning
ML	Machine Learning
k-NN	k-nearest neighbor
DT	Decision Tree
RF	Random Forest
SVM	Support Vector Machine
ResNet	Residual Network
InceptionNet	Inception Neural Network
StackNet	Stack Network
ResoNet Module	Resolution-aware Module
SRNet Model	StackNet-ResoNet Model
SARNet Model	StackNet-Attention Mechanism-ResoNet Model
SE Attention Mechanism	Squeeze-and-Excitation Attention Mechanism
IR Imaging	Infrared Imaging
IMI	Infrared/Thermal Imaging
EL imaging	Electroluminescence imaging
TP	True Positive
TN	True Negative
FP	False Positive
FN	False Negative
ReLU	Rectified Linear Unit

F1	F1-Score
Rec	Recall
AUC	Area Under Curve
ROC	Receiver Operating Characteristic
PRC	Precision Recall curve
LR	Learning Rate
L2	L2 Regularization
I-V	Current-Voltage
IVCA	Current-Voltage Characteristic Analysis
VTM	Visual and Thermal Imaging Method(s)
EBM	Electrical Detection Method(s)
Grad-CAM	Gradient-weighted Class Activation Mapping
GUI	Graphical User Interface

Glossary

Convolutional Neural Network: An architecture of network utilized for deep learning mission which are commonly used for computer vision projects

ResNet-18: A specific version of the Residual Network containing 18 layers, known for its balance between performance and computational efficiency.

Stack Network: A deep learning architecture that uses skip connections to prevent gradient issues in very deep networks.

Residual Block: A fundamental unit in StackNet architectures, consisting of convolutional layers and shortcut connections that help preserve gradient flow and improve learning stability.

ResoNet (Resolution-aware Network): A multi-branch convolutional structure that captures information at different scales using parallel convolutional layers, thereby enhancing feature diversity and spatial representation.

SRNet (StackNet-ResoNet Network): SRNet enhances the conventional residual block of the StackNet architecture by integrating the ResoNet module. This integration aims to improve the network's ability to capture multi-scale features.

SE (Squeeze-and-Excitation) Attention Mechanism: A channel-wise attention module that improves feature recalibration by adaptively weighting feature map channels based on global context. It comprises a 'squeeze' (global pooling) step and an 'excitation (gating) step.

SARNet (StackNet-Attention Mechanism-ResoNet): A neural network model that combines StackNet, attention mechanism, and ResoNet to improve feature representation and training stability.

Batch Normalization: A technique used to normalize layer inputs during training, which accelerates convergence and improves overall performance by reducing internal covariate shift.

ReLU (Rectified Linear Unit): A non-linear activation function defined as $f(x) = \max(0, x)$, commonly used in deep neural networks to introduce non-linearity and accelerate convergence.

Dropout: A regularization method where a fraction of neurons are randomly ignored during training to prevent overfitting and promote generalization.

Global Average Pooling: A pooling operation that computes the average of each feature map, reducing each channel to a single value, often used before fully connected classification layers.

Max Pooling: A downsampling operation that selects the maximum value within a kernel window, helping reduce spatial size while retaining important features.

Data Augmentation: A technique used to increase the diversity of data available for training models by applying random transformations to training images.

Data Separation: The process of dividing data into distinct sets, typically for training, validation, and testing purposes.

Data Balance: The concept of ensuring that each class in a dataset is equally represented to prevent model bias and improve generalization across different categories.

Resize: Changing the dimensions of an image, often to meet the input size requirements of a neural network.

Chapter 1 Introduction

1.1 Background

The consumption of energy is rising on a daily basis [1], so finding efficient ways to produce energy is becoming increasingly important. Compared with fossil fuels, renewable energy has lower greenhouse gas emissions, and the widespread adoption of it will help reduce environmental pollution [1]. As a renewable resource, solar energy does not cause global warming or damage ecosystems, thus helping to maintain ecological balance [1]. Solar panels use semiconductor materials and advanced technologies to convert solar radiation into electrical energy [1]. According to the National Renewable Energy Laboratory (NREL) [2], solar panels have a CO₂ emission rate of about 45 to 50 grams per kilowatt-hour, whereas coal-fired power plants emit 900 to 1,000 grams of CO₂. Therefore, promoting solar panels is considered an effective way to reduce both carbon dioxide emissions and environmental pollution [3].

Although solar panels are environmentally friendly and efficient, their performance is highly susceptible to various external and internal factors. Common faults, such as cracks, vegetation growth, soiling, diode failures, hot spots, pollution, fractures, and delamination [4]. These faults can seriously reduce energy conversion efficiency and shorten the lifespan of solar panels [5], impacting the stability and reliability of the entire solar energy system. For example, hot spots can cause localized overheating, while cracks and delamination may lead to permanent damage, reducing the overall output of the photovoltaic array. So timely identification and rectification of these issues are essential to maintain the consistent performance of solar panels and to prevent system-wide failures [6].

Currently, solar panel anomaly detection and classification primarily relies on visual inspection and electrical testing. Visual inspection is commonly conducted using infrared thermography (IRT) and electroluminescence (EL) imaging [7]. IRT detects thermal emissions from solar panel, identifying temperature anomalies that indicate potential faults such as hot spots and cell cracks [8]. In contrast, EL imaging captures the light emitted by solar panel under external voltage excitation, allowing visualization of internal electrical activity and enabling the detection of delamination and microcracks [9]. Electrical testing analyzes the electrical performance of solar panels to identify faults that affect efficiency and power output [10]. Among the commonly used methods, current-voltage (I-V) curve analysis measures the voltage and current characteristics of

the panel under varying loads, enabling the detection of power degradation, short circuits, and electrical mismatches [10]. Despite these methods boosting detection efficiency, they still have limitations, including low accuracy, high costs, restricted detection range, and dependence on environmental conditions.

In recent years, the application of CNN(Convolutional Neural Network) within deep learning has significantly advanced fault classification [4]. CNNs can automatically extract features from complex data and adapt to various fault types and data distributions. In solar panel anomaly classification, CNNs are particularly effective in processing infrared and electroluminescence (EL) images [10]. By learning from large-scale image datasets, CNN-based approaches provide an efficient and automated solution for fault classification, reduce manual intervention, and adapt to varying environmental conditions. Hence, leveraging CNNs for solar panel fault classification can improve the reliability and efficiency of solar systems, supporting intelligent operation and maintenance.

1.1.1 Risk and Factor

Solar panel faults arise from various environmental, mechanical, and electrical factors, affecting system efficiency and lifespan. The primary risks include performance degradation, energy loss, and increased maintenance costs. Key contributing factors are as follows and shows in Figure 1:

1. Environmental Factors

- Extreme weather conditions (hurricanes, hailstorms, heavy snowfall) can cause structural damage, cracks, or fractures, necessitating regular inspections to prevent long-term degradation [11].
- Dust, dirt, and pollutants accumulate on panel surfaces, obstructing sunlight and reducing energy conversion efficiency [11].
- Vegetation growth (shading from trees, vines attaching to panels) not only limits sunlight exposure but also exerts mechanical stress, leading to potential damage [11].
- High humidity and salt exposure accelerate corrosion and delamination, particularly in coastal regions where salt particles in the air increase degradation rates.

2. Mechanical Factors

- Improper installation (loose mounting, incorrect angling, poor fixation) can lead to structural instability, increasing the likelihood of panel deformation or failure [11].
- Physical impact from falling tree branches, maintenance tools, or accidental collisions may cause cracks, fractures, or surface damage.
- Shading from buildings or nearby objects can create localized current mismatches, leading to hotspot formation and power loss.

3. Electrical Factors

- Bypass diode failure, poor wiring connections, and inverter issues can result in localized overheating, leading to hot spots that degrade performance and may cause permanent damage.
- Inadequate cleaning practices (using abrasive materials or strong chemicals) can deteriorate the protective coating, reducing panel durability [11].

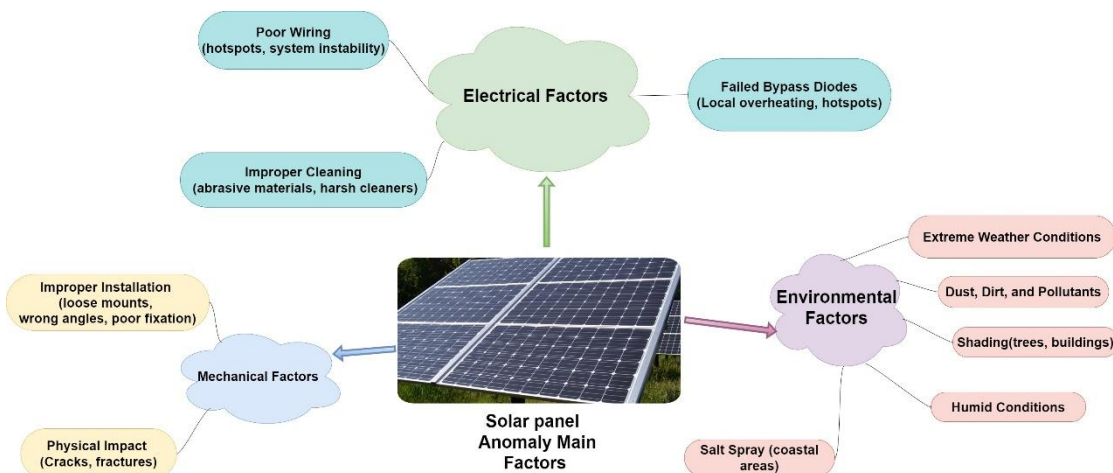


Figure 1. Factors of Solar Panel Anomaly

1.1.2 Challenge

Despite the growing importance of solar energy, existing anomaly detection methods still face several practical challenges, particularly during the inspection and maintenance of solar panels. These challenges include:

1. Low Detection Accuracy

- External Factors Impact: Traditional methods like infrared thermography (IRT), electroluminescence (EL) imaging, and I-V curve analysis are sensitive to environmental conditions, leading to inaccurate results.

- Complex Fault Behavior: These methods often miss early-stage faults, like microcracks or subtle temperature changes.
2. Misclassification of Anomalies
 - Visual Similarity Between Faults: Different faults (like hot spots vs. soiling, cracks vs. delamination) can appear visually similar, leading to misclassification.
 3. Delayed Fault Response
 - Manual Inspection Delays: Human inspections take time, especially in large or remote solar farms, delaying fault detection and repair.
 - Offline Analysis: Many fault analyses are done offline, further extending response times and leading to performance loss or equipment damage.
 4. High Maintenance and Inspection Costs
 - Labor Costs: Skilled technicians are required for inspections and analysis, adding to the overall cost.
 - Time and Logistical Costs: Inspections are time-consuming, especially in large or remote sites, increasing transportation and operational costs.
 5. Lack of Scalable and Standardized Inspection Systems
 - Lack of Automation: Traditional methods are manual and cannot scale efficiently for large installations.
 - Varied Conditions: Different panel types, manufacturers, and locations require customized inspection approaches, making standardization difficult and leading to inconsistent monitoring.

1.2 Aim

This project's aim is to develop a deep learning model for classify anomaly in solar panels using infrared imaging and Electroluminescence imaging (EI) data. The ultimate goal is to optimize maintenance schedules, prolong the lifespan of solar panels, and enhance overall energy efficiency.

1.3 Objectives

- A. Research on deep learning models for solar panel anomaly classify.
- B. Select feasible deep learning models for classify solar panel fault.
- C. Gather suitable infrared imaging and Electroluminescence imaging dataset for solar panel fault classify.
- D. Develop selected deep learning model.
- E. Evaluate the models using statistical techniques.

F. Summarize and finishing up.

1.4 Project Overview

This project integrates infrared (IR) and electroluminescence (EL) imaging technology with deep learning models to achieve automated fault classification, enhancing detection efficiency and accuracy and the overview is seen in Figure 2. The SARNet model will be trained on two large-scale datasets to accurately identify solar panel conditions. An attention mechanism will be incorporated to improve the model's focus on critical regions, enhancing fault detection precision. Additionally, Grad-CAM (Gradient-weighted Class Activation Mapping) will be utilized to visualize the model's decision-making process, generating heatmaps to highlight key fault areas and improve interpretability. A graphical user interface (GUI) will enable users to upload images and receive real-time analysis results, streamlining the maintenance process.

1.4.1 Scope

The purpose of this project is to optimize a convolutional neural network (CNN) model for solar panel anomaly classification by using infrared and electro-luminescence imaging data. Specifically, it will focus on enhancing the CNN model based on StackNet, ResoNet and incorporating an attention mechanism.

The significance of this project is as follows:

- Promote the development of renewable energy technology.
- Reduce maintenance costs.
- Improve energy production efficiency.
- Support sustainable development.
- Provide support for future research.

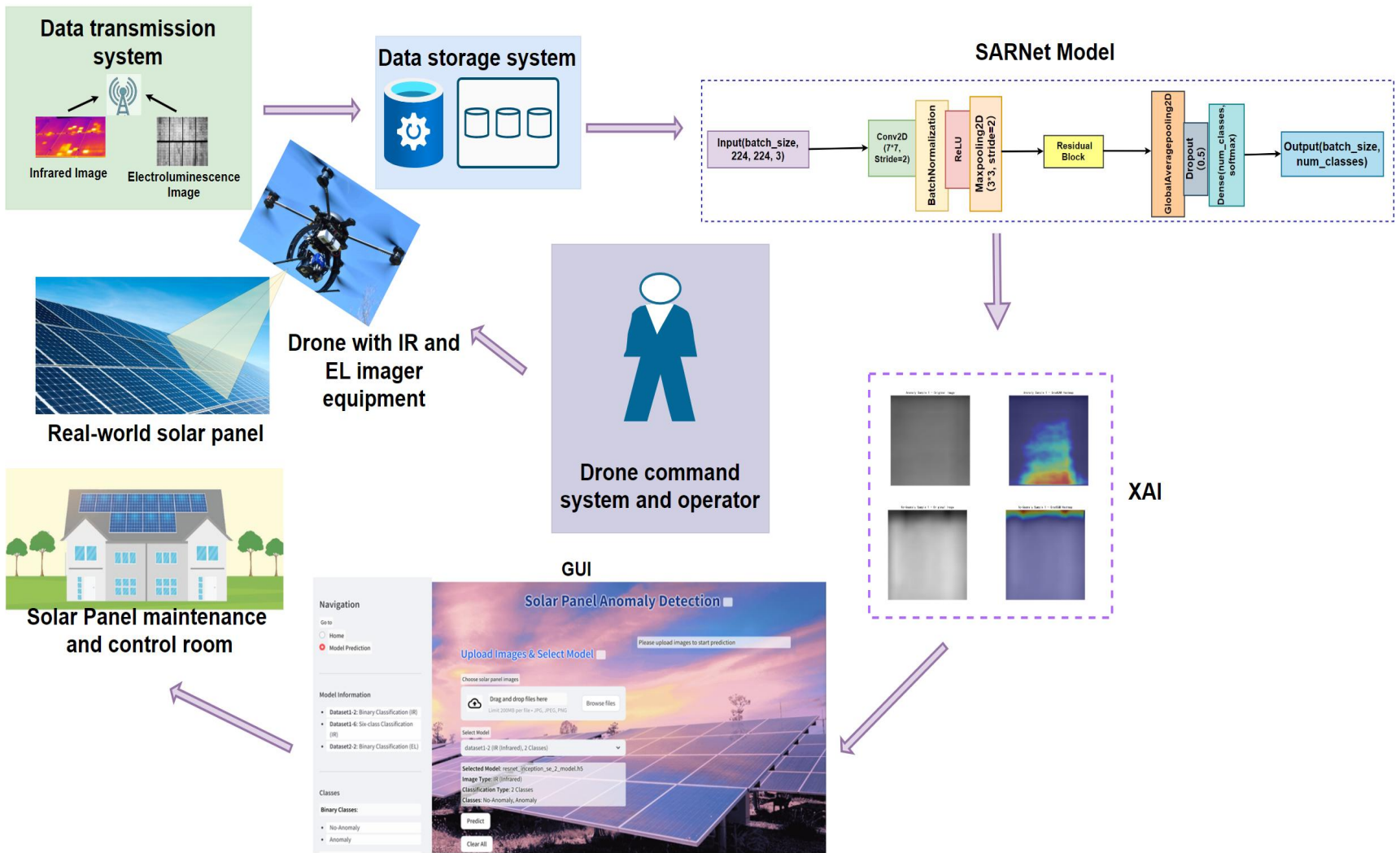


Figure 2. Project overview

1.4.2 Audience

The development of the deep learning-based model for solar panel anomaly classification using infrared imaging and Electroluminescence imaging will bring significant benefits to various stakeholders.

- Engineers and technicians: Enhance the efficiency and accuracy of fault detection, reducing downtime for solar systems.
- Solar panel owners and investors: Decrease maintenance costs, extend the lifespan of solar panels, and increase return on investment.
- Renewable energy companies and policymakers: Optimize operations and support policy decisions to improve energy production efficiency.
- Academic researchers: Provide valuable insights for researchers in computer science and energy systems, helping to advance the application of deep learning in the energy sector.

In summary, the proposed deep learning-based solar panel anomaly classification model using infrared and electro-luminescence images will provide significant benefits to various stakeholders in the energy industry. By enhancing the efficiency and accuracy of anomaly classification, reducing maintenance costs, and improving energy production, it will contribute to the sustainable development of solar energy and provide valuable support for future research.

Chapter 2 Background Review

This chapter provides a comprehensive review of various methods used for solar panel fault classification, highlighting the evolution from traditional techniques to more advanced machine learning and deep learning approaches.

2.1 Solar Panel Anomaly Classification Using Traditional Methods

The traditional methods for classifying anomalies in solar panels mainly include two categories: visual and thermal imaging methods (VTMs) and electrical detection methods (EBMs) [10]. Like Figure 3, each approach leverages distinct principles and tools to identify and classify faults, offering complementary strengths and addressing different diagnostic needs.

VTMs detect surface and internal faults in solar panels [11]. Infrared imaging identifies heat anomalies from electrical issues without extra sensors [12], offering a cost-effective solution for systems of all sizes. Visual inspection detects surface defects through direct observation, while electroluminescence imaging uses injected current to reveal internal issues like cracks and poor contacts with high accuracy [10]. These methods, though equipment-dependent, are essential for reliable fault detection.

EBMs analyze current and voltage characteristics to identify faults. I-V Curve Analysis detects issues like short circuits and shading by comparing normal and faulty curves [10]. Power Loss Analysis (PLA) locates problems such as hot spots and degradation by measuring output deviation. Current and Voltage Measurement identifies wiring faults or imbalances through deviations from expected electrical values [13].

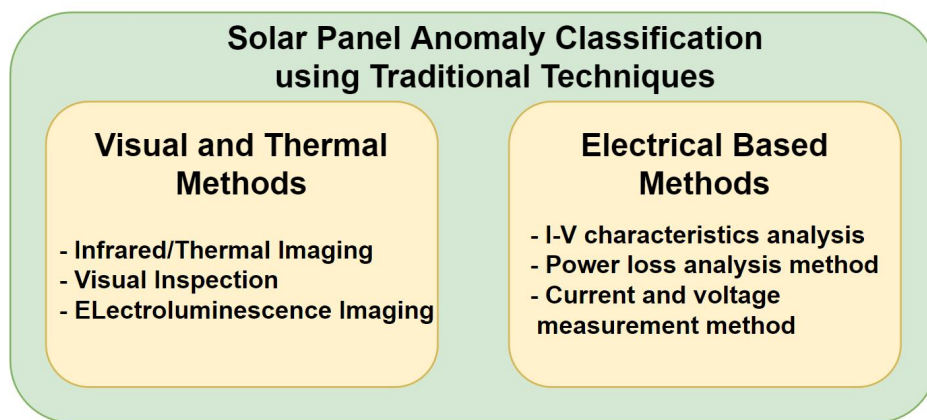


Figure 3. Categories of solar panel anomaly classification traditional methods.

2.2 Solar Panel Anomaly Classification Using Machine Learning Technologies

Various machine learning algorithms, such as k-nearest neighbor (k-NN), decision tree (DT), random forest (RF), and support vector machine (SVM), have been widely applied in anomaly detection and classification of solar panel systems [10].

The k-nearest neighbor (k-NN) algorithm is a simple yet effective method for detecting anomalies in solar panels, such as open-circuit, line-to-line, and partial shading issues. For instance, Madeti and Singh [14] used k-NN with experimental data and temperature variables, achieving 98.70% accuracy. Despite its simplicity, KNN's performance can be further improved by integrating fuzzy logic, enhancing adaptability in real-world conditions. The decision tree (DT) algorithm, known for simplicity and interpretability, is also commonly used for anomaly detection [10]. As shown in Figure 4, Madani et al.[15], combined DT with AdaBoost, enhancing its accuracy and robustness in dynamic environments.

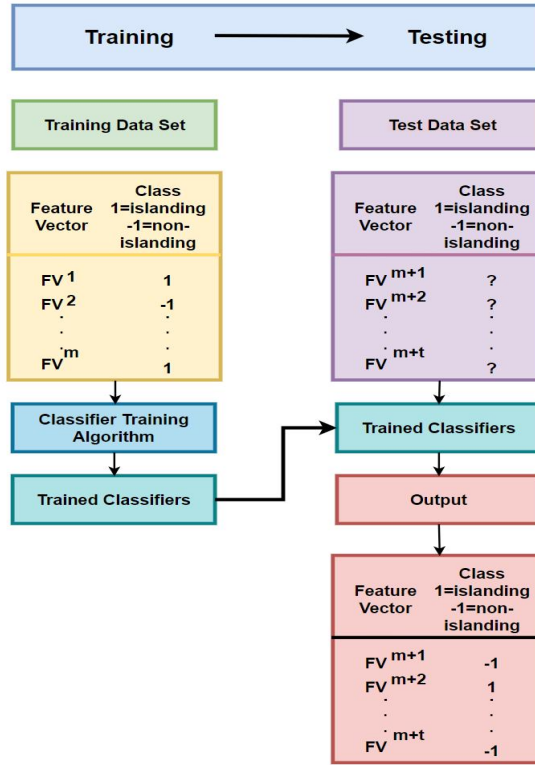


Figure 4. Madani et al.[15] decision tree (DT) with AdaBoost algorithm.

Unlike the deterministic nature of decision trees (DT), random forests (RF) use an ensemble learning approach, improving prediction accuracy and robustness [10]. As shown in Figure 5, Dhibi et al.[16] proposed reduced-kernel RF have improved feature

extraction and classification efficiency, showcasing the potential of RF in handling large-scale solar panel systems with diverse operating conditions.

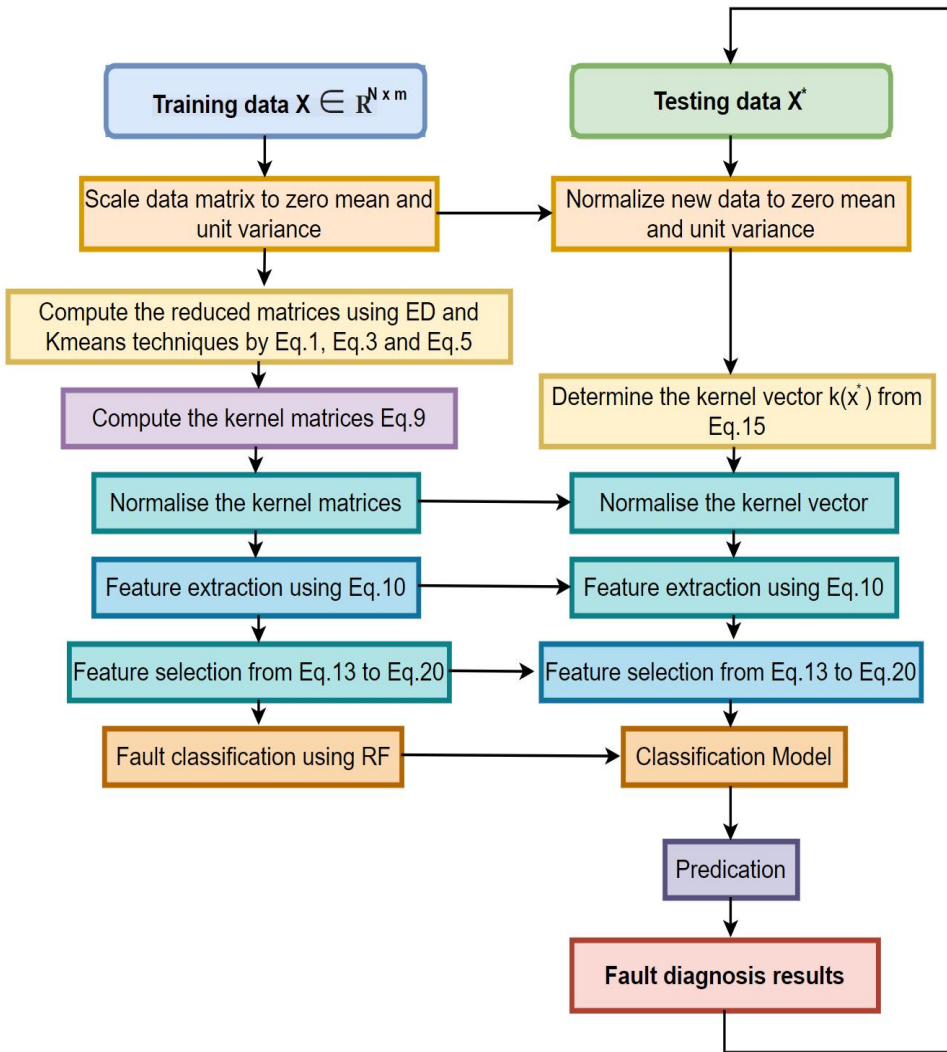


Figure 5. RK-RF Algorithm Flowchart by Dhibi et al. [16]

Among these algorithms, support vector machine (SVM) is particularly known for its strong classification in anomaly detection [10]. It handles high-dimensional data and separates classes clearly. As illustrated in Figure 6, Yi and Etemadi [17] combined multi-resolution signal decomposition (MSD) with SVM for line-to-line anomaly detection, achieving high accuracy.

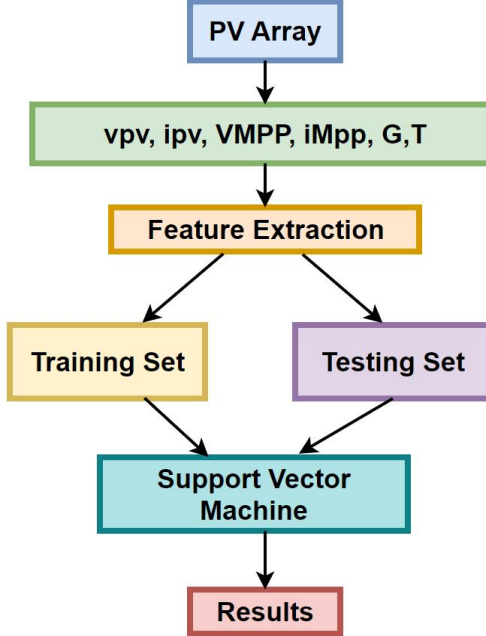


Figure 6. Yi and Etemadi [17] Algorithm Based on SVM.

2.3 Solar Panel Anomaly Classification Using Deep Learning Technologies

2.3.1 CNN Methods

Convolutional Neural Networks (CNNs) have become a dominant approach for solar panel anomaly classification, particularly due to their ability to automatically extract features from image data. This capability is crucial for monitoring large-scale solar panel systems, where datasets often include diverse modalities such as infrared (IR), electroluminescence (EL), and visible light images [10]. The adaptability of CNNs makes them effective for both binary and multi-class classification tasks.

For example, Alves et al.[18] used a CNN model with undersampling and oversampling to handle class imbalance, achieving 92.5% accuracy in binary classification, and accuracies of 66.43% and 78.85% for datasets with 12 and 8 fault types. Espinosa et al.[19] applied CNNs for semantic segmentation and classification from RGB images, attaining 75% accuracy for binary fault detection and 70% for four fault categories.

As CNN-based models advanced, Le et al.[19] further enhanced CNN-based approaches by incorporating a deep neural network with a residual network structure and ensemble techniques shows in Figure 7, achieving 94% accuracy for binary classification and 86% for classifying 12 anomaly types.

In a significant development, Korkmaz and Acikgoz [20] used a multi-scale CNN with transfer learning on thermographic images, achieving 93.51% accuracy for 11 anomaly types. Deitsch et al.[23] applied an end-to-end deep CNN to classify normal and abnormal categories in 1,968 EL extracted cells, reaching 88.42% accuracy. Otamendi et al.[20] employed a CNN for cell-level anomaly detection, attaining 84% accuracy in distinguishing defective modules.

These advancements show that CNNs are constantly improving, enhancing the accuracy and robustness of solar panel fault classification for various anomalies.

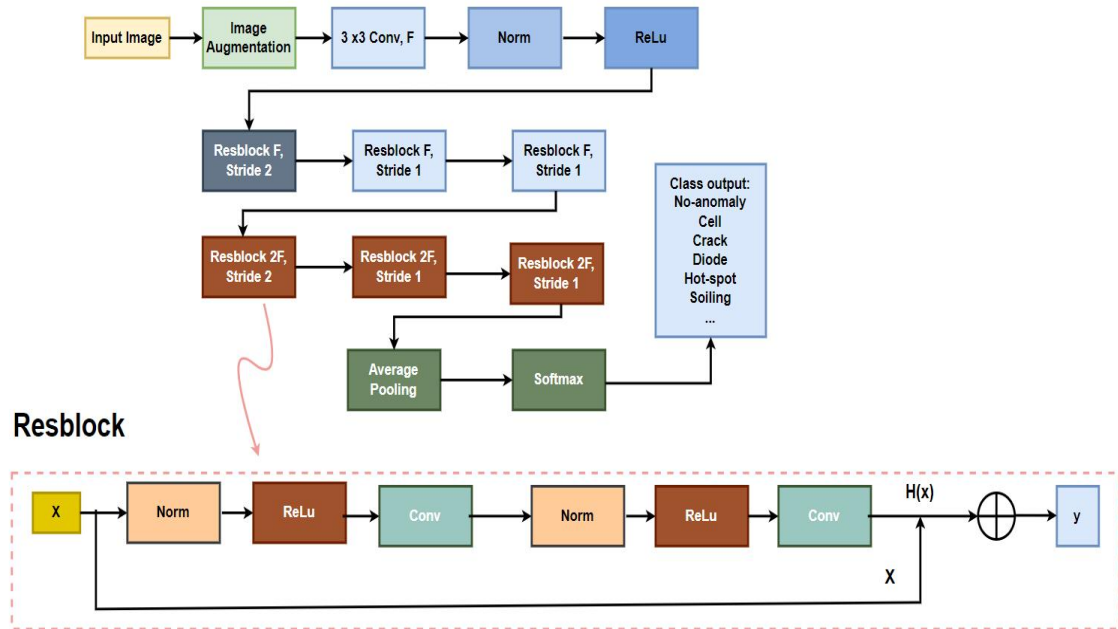


Figure 7. ResNet structure by Le et al.[19]

2.3.2 Attention Mechanism

Attention mechanisms have been increasingly utilized in solar panel anomaly classification due to their ability to focus on salient features and enhance representation learning [21]. Liu et al.[22] used attention-based masking to remove non - salient regions and focus on relevant features. Bozorgtabar and Mahapatra [27] applied attention-based learnable masks to detect and localize anomalies. Sim et al.[28] used attention masking to eliminate unnecessary background information, improving generalization. As shown in Figure 8, Park et al.[29] utilized attention masking for anomaly detection and inpainting techniques for defect identification. Overall, these studies show attention mechanisms boost solar panel anomaly detection model accuracy and reliability.

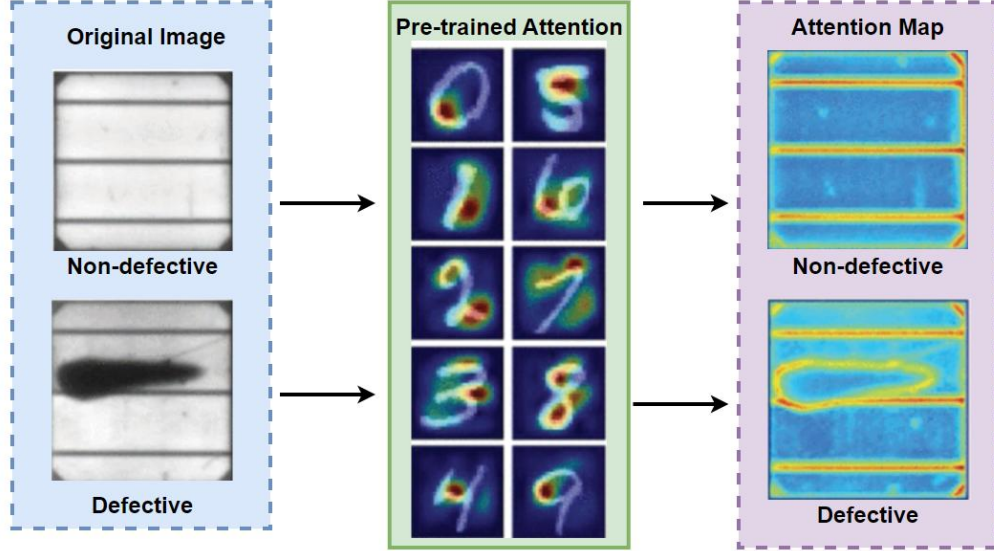


Figure 8. Park et al. [29] mentioned attention Mechanism.

2.3.3 Hybrid Attention-CNN Methods

The integration of attention mechanisms with CNN methods has proven highly effective in solar panel anomaly classification, offering improvements in defect detection. By leveraging attention mechanisms, models can focus on critical defect regions, enhancing the detection of fine-grained anomalies that traditional methods often miss. For instance, Zhang et al.[23] combined CNN with the CBAM attention module, achieving 95.22% accuracy across complex defect categories. In Figure 9, Lee et al.[21] proposed a lightweight solution with pre-trained attention mechanisms. Their dual-masking technique (AGDM) enhanced performance by efficiently extracting defect information, achieving an accuracy of 84.6% in binary classification (between normal and abnormal). Royal et al.[32] achieved an AUROC score of 0.97 in EL image anomaly detection, validating the potential of combining attention mechanisms with CNNs.

These methods collectively demonstrate that hybrid attention-CNN approaches excel in handling complex and diverse defect scenarios, offering high accuracy, efficiency, and adaptability for solar panel anomaly classification.

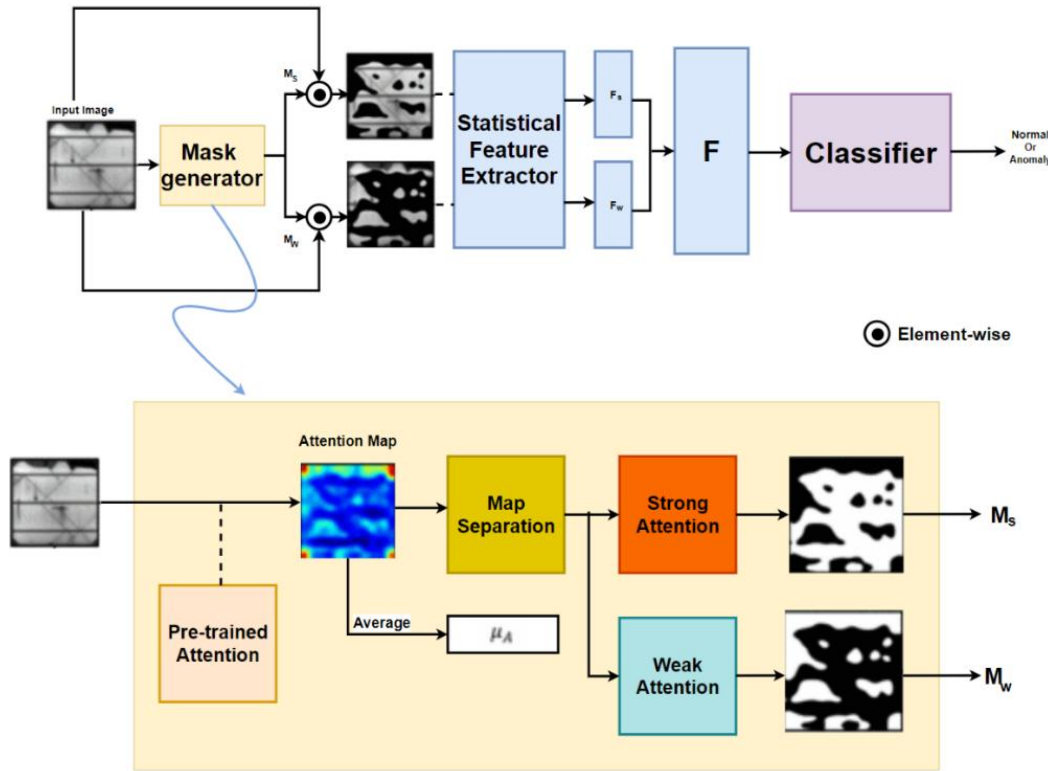


Figure 9. Lee et al.[21] proposed model 's overall AGDM detection process

A summary of the different researchers and their findings and possible results can be found in Table 1.

Table 1. Summary of Related Works

Author	Datasets	Limitations	Algorithm	Performance criteria
Madeti and Singh [14]	Solar Panel HT Instruments Solar I-V Data	The model relies on manufacturer data sheets, which may affect its generalizability.	k-nearest neighbor (k-NN)	Average fault classification accuracy of 98.70%.
Madani et al. [15]	Solar Panel Array Dataset	Dependence on specific	Decision Tree (DT) with	Improve classification

		environmental conditions, potential overfitting to dataset characteristics.	AdaBoost Algorithm	accuracy and robustness.
Dhibi et al. [16]	Emulated Grid-Connected Solar Panel System Data	Noncorrelation between variables, static information from process data, redundancy in samples.	Random Forest (RF)	High classification accuracy, low computation time.
Yi and Etemadi [17]	Solar Panel Array Data	Masking of L-L faults by MPPT, challenges under low irradiance or high fault impedance.	Support Vector Machine (SVM)	High classification accuracy.
Alves et al. [18]	Infrared Solar Module dataset	Class imbalance, leading to lower performance in multi-class classification.	CNN	92.5% accuracy in binary classification; 66.43% accuracy for 12 classification and 78.85% accuracy for 8 classification.
Le et al. [19]	Infrared Solar Module	Computationally expensive due	CNN	94% accuracy for binary

	Dataset	to deep network structure.		classification and 86% for classifying 12 anomaly types.
Korkmaz et al. [20]	Infrared Solar Module Dataset	Requires large-scale labeled data for effective transfer learning.	CNN with transfer learning	93.51% for classifying 11 anomaly types
Lee et al.[21]	ELPV Dataset	Requires high computational power.	EfficientNetB0 with Attention Network	84.6% Binary classify (normal and abnormal)
Zhang et al. [23]	Infrared Images	Requires high computational power due to EfficientNetB3 model complexity.	CNN (EfficientNetB3) with Attention network	95.22% accuracy across complex defect categories
Espinosa et al. [24]	Infrared Images	Limited dataset size, affecting generalization.	CNN	Accuracy of 75% for binary fault classify and 70% accuracy for four different fault types (no-fault, cracks, shadows, and dust).
Deitsch et al. [25]	1,968 EL Images	Small dataset size, potential	CNN	88.42% Binary classify (normal

		bias in classification.		and abnormal)
Otamendi et al. [26]	ELPV Dataset	Limited to cell-level analysis.	CNN	84% accuracy for classify defective from non-defective modules.
Park et al. [27]	EIPV Dataset	Limited performance in detecting subtle defects.	CNN with Attention Network	90.4% Binary classify (normal and abnormal)
Royal et al. [28]	EL images	Requires additional pre-processing for optimal results.	CNN with Attention Network	AUROC score of 0.97 in EL image anomaly detection

Chapter 3 Methodology

3.1 Approach

This chapter outlines the experimental design for evaluating the proposed models. It introduces the datasets used, the architecture of the proposed CNN model, and the data preprocessing procedures. The training setup, including hyperparameter configuration and training strategies, is then described. Finally, the evaluation section summarizes the metrics used to assess model performance across different classification tasks.

3.2 Dataset

This study uses two datasets to support model development. Dataset 1 (Infrared Solar Modules) serves as the primary dataset, providing infrared images of common fault types to build core classification capabilities. Dataset 2 (ELPV) is a supplementary dataset based on electroluminescence imaging, used to improve generalization by introducing data from a different modality.

3.2.1 Dataset 1 – Infrared Solar Modules

During the training process, the Infrared Solar Modules dataset [29] as shown in Table 2 and Figure 10, referred to as Dataset 1, will be the primary dataset used. It contains images captured with infrared cameras, focusing on detecting faults such as hot spots, cracks, and material degradation. The images in Dataset 1 have an initial resolution of 24 * 40 pixels. This dataset includes 12 classes: 11 anomaly classes and one class labeled ‘No-Anomaly’, representing the absence of faults. This enables effective classification and detection of various solar panel issues, improving the efficiency and longevity of photovoltaic systems.

Table 2. Described each class in Infrared Solar Module Dataset

Class Name	No. Images	Description
Cell	1,877	Hot spot occurring with square geometry in single cell.
Cell-Multi	1,288	Hot spots occurring with square geometry in multiple cells.

Cracking	940	Module anomaly caused by cracking on module surface.
Hot-Spot	249	Hot spot on a thin film module.
Hot-Spot-Multi	246	Multiple hot spots on a thin film module.
Shadowing	1,056	Sunlight obstructed by vegetation, man-made structures, or adjacent rows.
Diode	1,499	Activated bypass diode, typically 1/3 of module.
Diode-Multi	175	Multiple activated bypass diodes, typically affecting 2/3 of module.
Vegetation	1,639	Panels blocked by vegetation.
Soiling	204	Dirt, dust, or other debris on surface of module.
Offline-Module	827	Entire module is heated.
No-Anomaly	10,000	Nominal solar module.

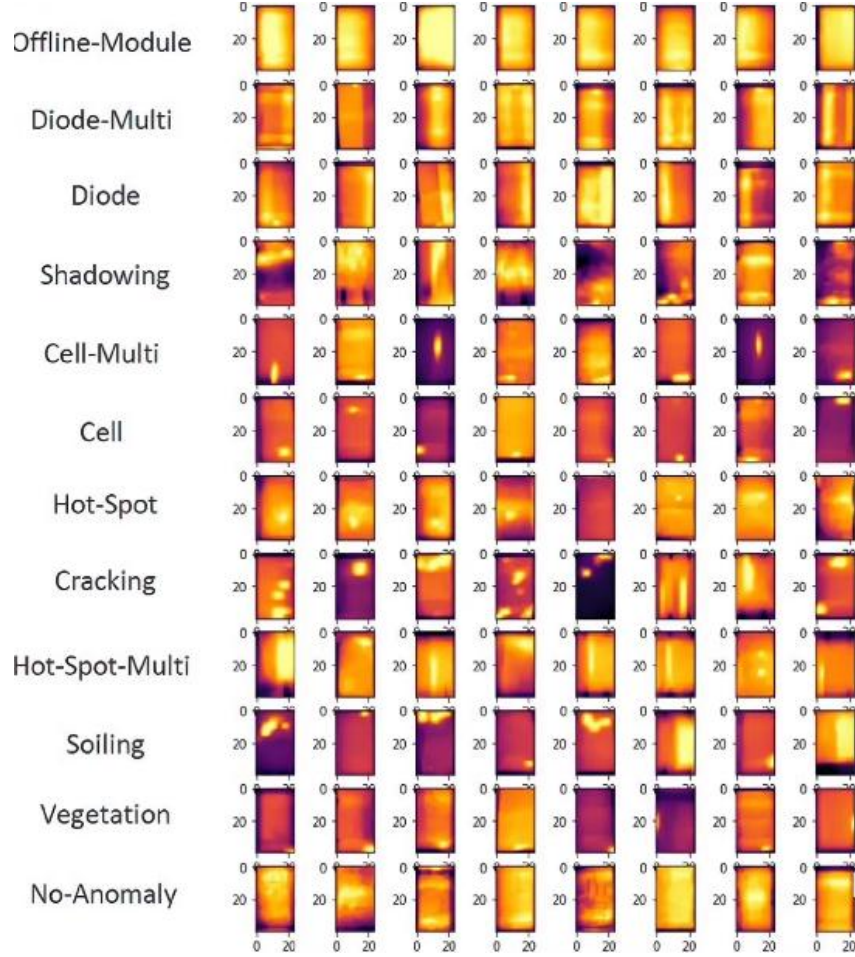


Figure 10. Few sample categories in the Infrared Solar Modules Dataset

3.2.2 Dataset 2 - Electroluminescence Photovoltaic (ELPV)

Additionally, the ELPV dataset [30], referred as the dataset 2, while used for supplementary training, is not the primary focus of this research. Dataset 2 uses Electroluminescence (EL) imaging to capture images, revealing defects such as cracks and soldering issues that can cause power loss [25]. The dataset includes 2,624 samples with an initial resolution of 300×300 pixels, classified into four categories showing in Figure 11: ND (non-defected), PN (possibly normal), PD (possibly defected), and DF (defected). As shown in Figure 12, the defects vary in severity, with probabilities assigned based on the expected damage for each cell.

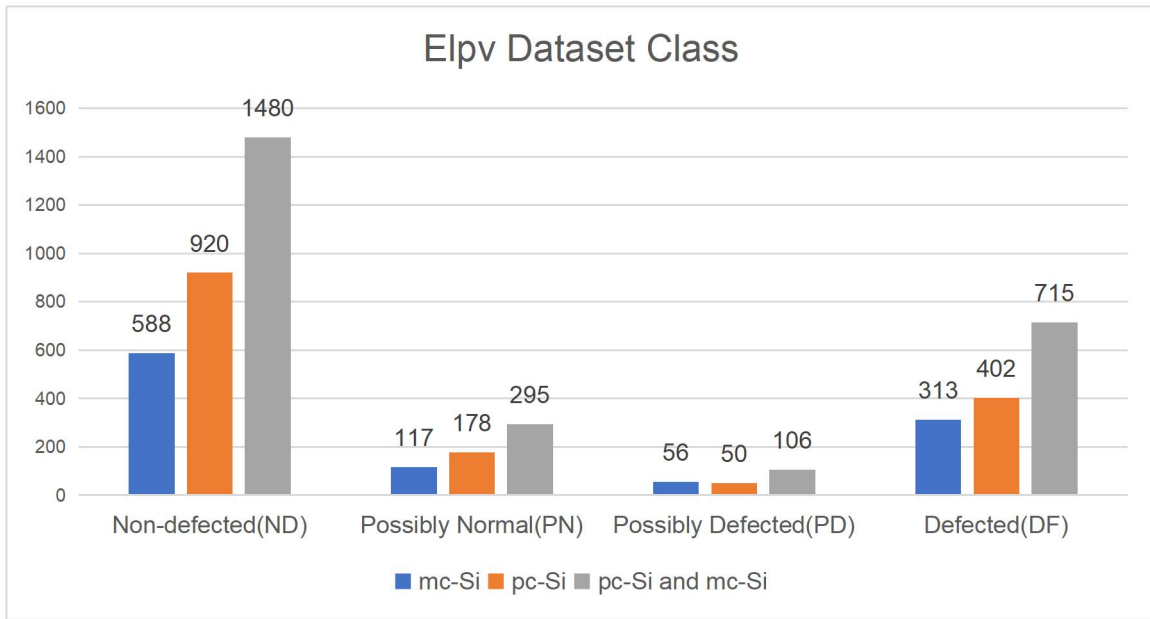


Figure 11. The distribution of the PV cells per class in the original ELPV dataset

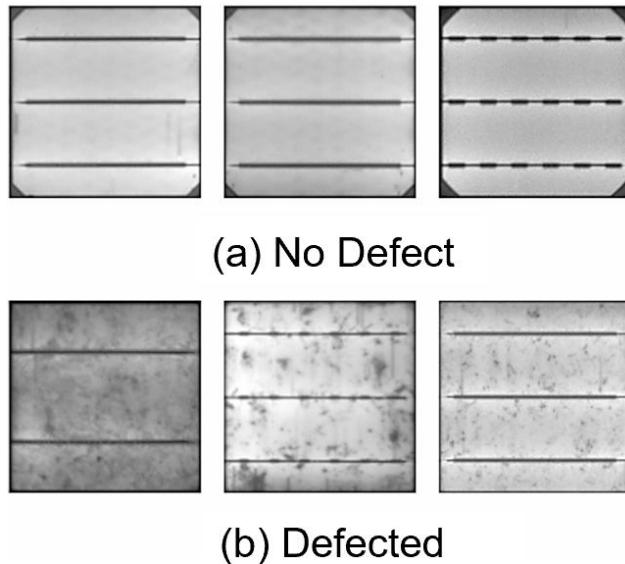


Figure 12. Selected EL images (from the ELPV dataset)

3.3 Data Preprocessing

Comprehensive preprocessing was conducted to ensure the datasets were suitable for model development. Key steps included data splitting, class balancing, resizing, and augmentation, which together produced standardized and diverse inputs, supporting both robust training and enhanced generalization across classification tasks.

3.3.1 Data Split

For this research, in Infrared Solar modules dataset 1, the data is divided into three subsets: training, validation, and test sets. As shown in Figure 13 and Figure 14, the training set comprises 70% of the data, while the validation and test set each account for 15%. The dataset is processed in both binary and multi-class formats. In binary classification, the task is to distinguish between ‘Anomaly’ and ‘No-Anomaly’. In the multi-class classification task, instead of using all 12 original categories, a subset of 6 representative classes was selected to address the issue of data imbalance. These include Vegetation, Shadowing, Cell, Diode, Cracking, and Offline-Module. This selection maintains defect diversity while ensuring a more balanced class distribution for effective model training. This structured split ensures effective training and evaluation for both classification tasks.

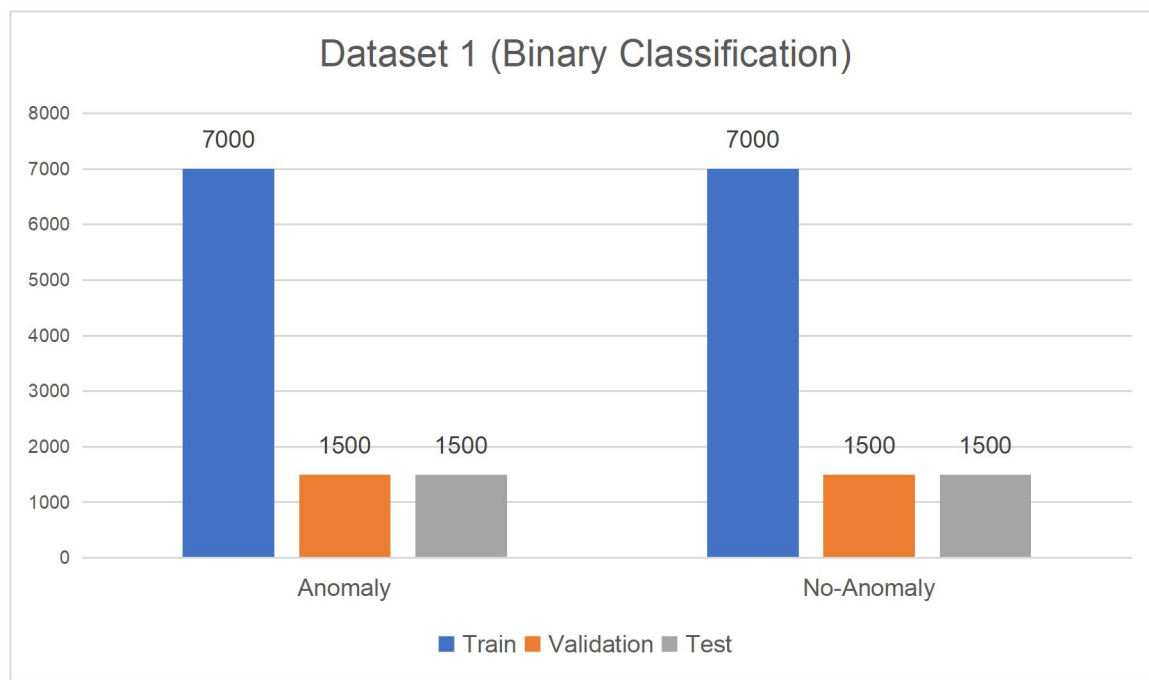


Figure 13. Data separation of dataset 1 (Binary Classification)

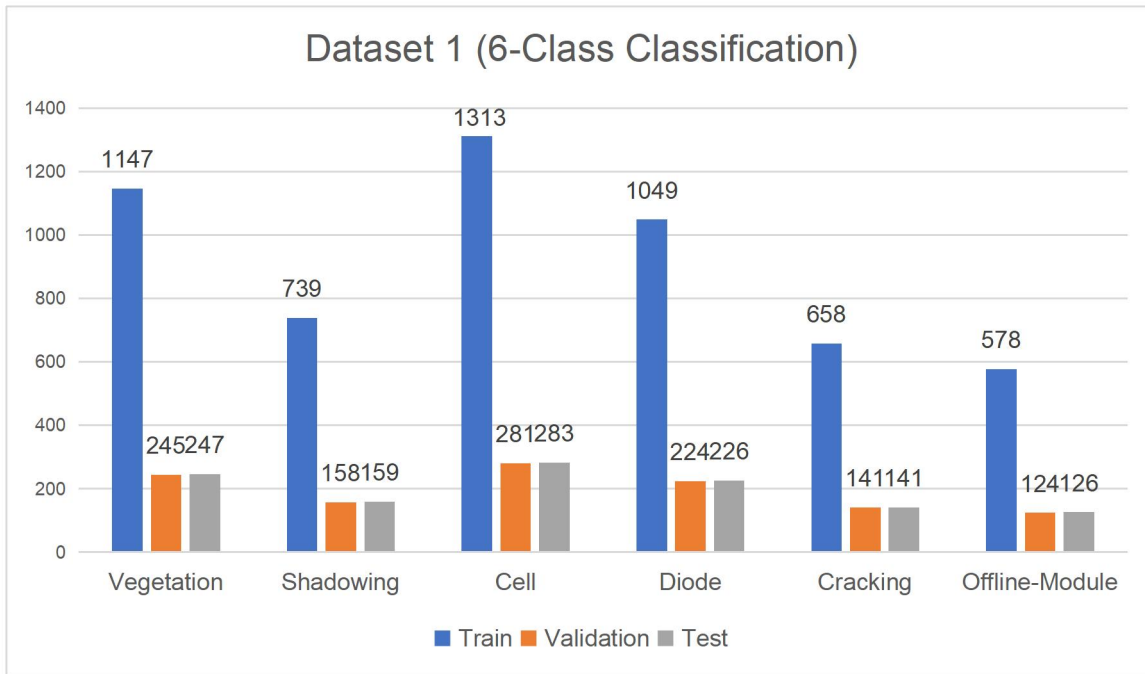


Figure 14. Data separation of dataset 1 (6-Class Classification)

Similarly, the ELPV dataset 2 shown in Figure 15 is split into training (70%), validation (15%), and test sets (15%). It's formatted for four-class classification: Non-Defected (ND), Defected (DF), Possibly Normal (PN), and Possibly Defected (PD). ND images have no visible faults; DF images have defects like micro-cracks; PN and PD images have uncertain conditions. This four-class approach allows more nuanced training, improving the model's ability to detect different defect severities in photovoltaic systems.

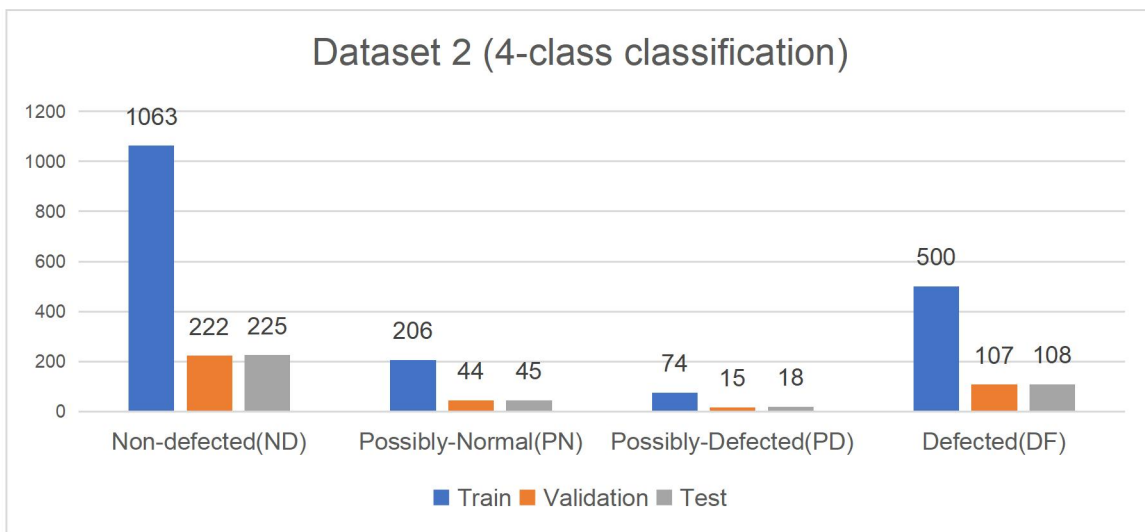


Figure 15. Data separation of dataset 2 (4-Class Classification)

3.3.2 Data Balancing

In this study, for the binary classification task of dataset 1, since the number of samples shows in Figure 16 for the anomaly class and the normal class are already balanced, no additional oversampling and undersampling is required, and the model can be directly trained.

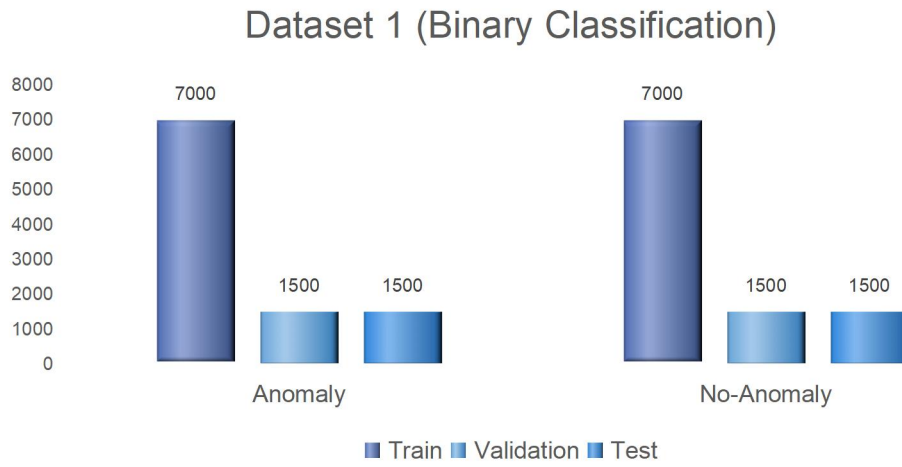


Figure 16. Balanced Data of Dataset 1 (Binary Classification)

To fix class imbalance in the six-class task, a hybrid sampling method blending random undersampling and oversampling was used. The six anomaly categories are Vegetation, Diode, Shadowing, Cell, Cracking, and Offline-Module, each set to have 1,000 samples. If a class had more images, random undersampling cut it to 1,000; if fewer, random oversampling brought it up. This balanced all six classes, curbing model bias. The balanced dataset in Figure 17 was then split into training, validation, and test subsets via stratified sampling to keep class ratios.

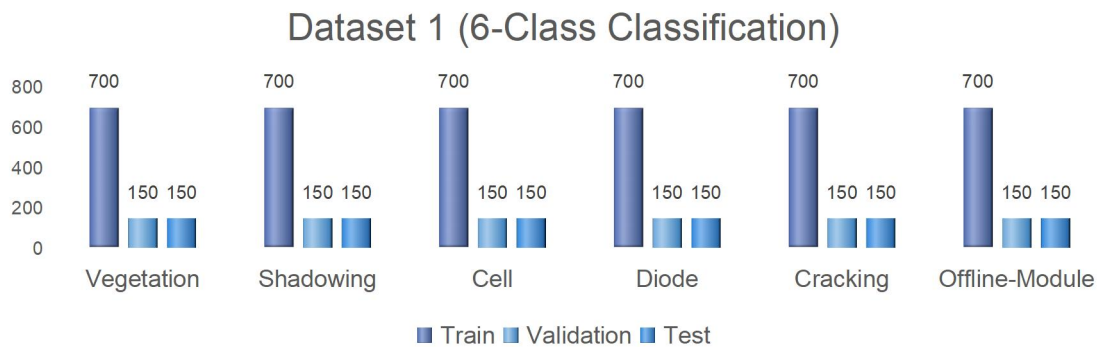


Figure 17. Balanced Data of Dataset 1 (6-Class Classification)

In dataset 2, due to the difficulty in distinguishing between the ‘Possibly-Normal (PN)’ and ‘Possibly-Defected (PD)’ categories, and the relatively small number of samples in these categories, they were merged into a single ‘Defected (DF)’ category. This adjustment helps balance the dataset. As the result shows in Figure 18, the dataset was simplified into two categories: ‘Non-Defected (ND)’ and ‘Defected (DF)’. This data partitioning and preprocessing ensure an effective training and evaluation process.

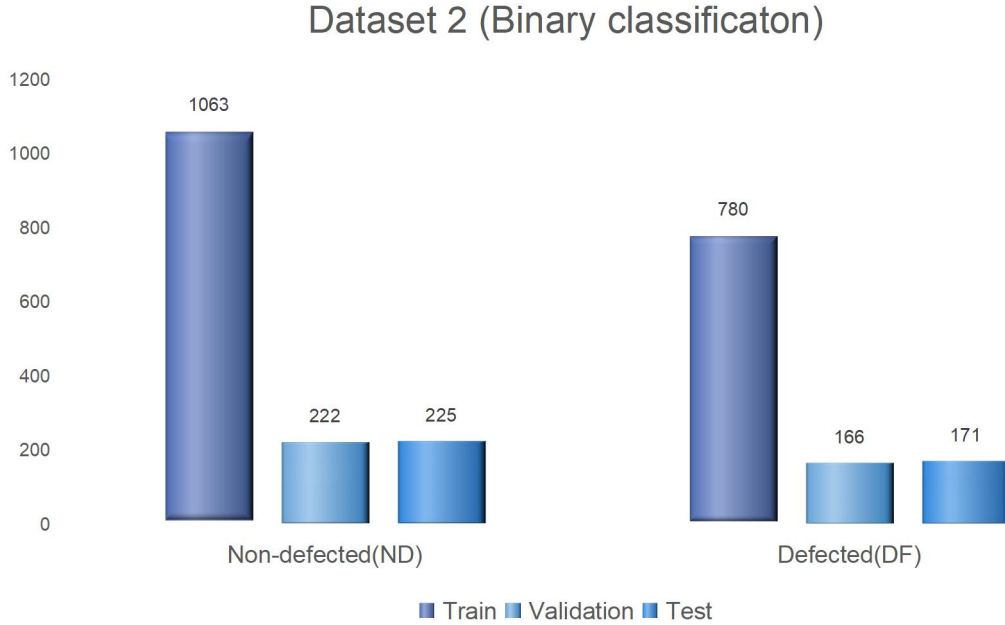


Figure 18. Balanced Data of Dataset 2 (Binary Classification)

3.3.3 Data Resize

As mentioned in the introduction, the initial resolution of the images in Dataset 1 is 24 * 40 pixels, while the images in Dataset 2 have an initial resolution of 300 * 300 pixels. These resolutions are not suitable for direct input into the proposed model. Therefore, in this study, all images were resized to 224 * 224 pixels. This preprocessing step ensures that the images meet the input size requirements of the model, thereby enabling proper training and inference.

3.3.4 Data Augmentation

In the processing of Dataset 1, data augmentation techniques such as random horizontal flipping, random rotation (up to $\pm 10\%$), and random zoom (up to $\pm 10\%$) were applied. In the processing of Dataset 2, data augmentation techniques such as random

horizontal flipping, random rotation (up to 20°), random width and height shifts (up to 20%), random shear (up to 20%), and random zoom (up to 20%) were applied.

3.4 Proposed Model Structure

The proposed CNN model, named SARNet, is built upon an enhanced architecture that incorporates StackNet as its backbone, integrating ResoNet modules and Squeeze-and-Excitation (SE) attention mechanisms. Together, these components enhance the model's representational power and focus on relevant features, improving classification accuracy and robustness in solar panel anomaly detection tasks.

3.4.1 StackNet

The proposed StackNet architecture builds upon the ResNet-18 backbone, with targeted modifications to enhance feature extraction efficiency while maintaining computational lightness. The model begins with a large-kernel convolutional layer for effective low-level feature capture, followed by normalization, activation, and pooling to reduce spatial resolution early and accelerate training.

StackNet's core consists of four residual stages that incrementally increase channel dimensions from 64 to 512 while reducing spatial dimensions through stride convolutions. As shown in Figure 19, each residual block employs shortcut connections to maintain direct information flow, mitigating the vanishing gradient problem. When dimensional mismatches occur, 1×1 convolutions adjust the shortcut path. Additionally, dropout is integrated into each block to prevent overfitting.

In Figure 20, StackNet strikes a balance between architectural depth and training efficiency, offering strong representational capacity with minimal increase in complexity. This makes it particularly suited for solar anomaly detection tasks where both performance and computational cost are critical.

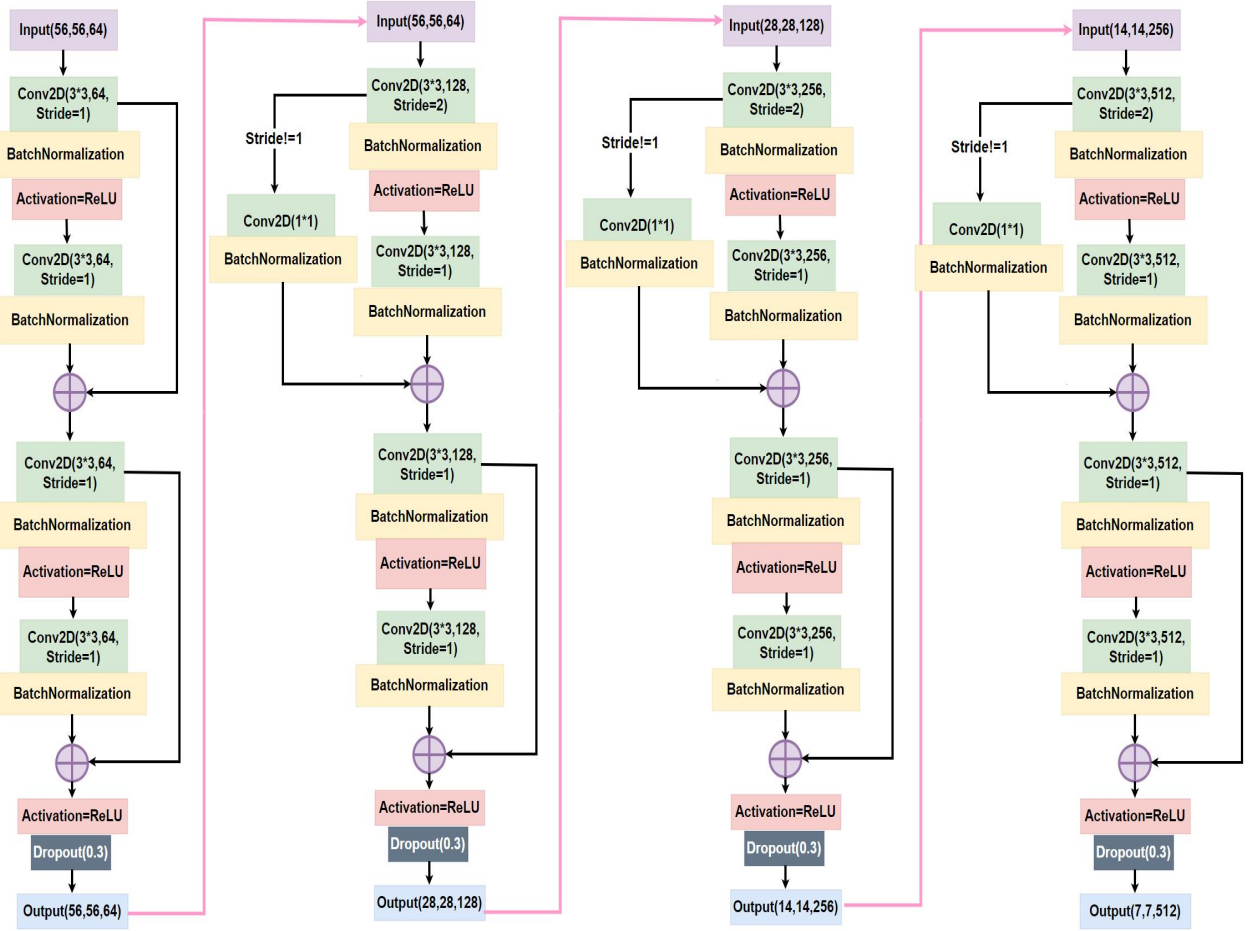


Figure 19. Residual block structure diagram for each stage

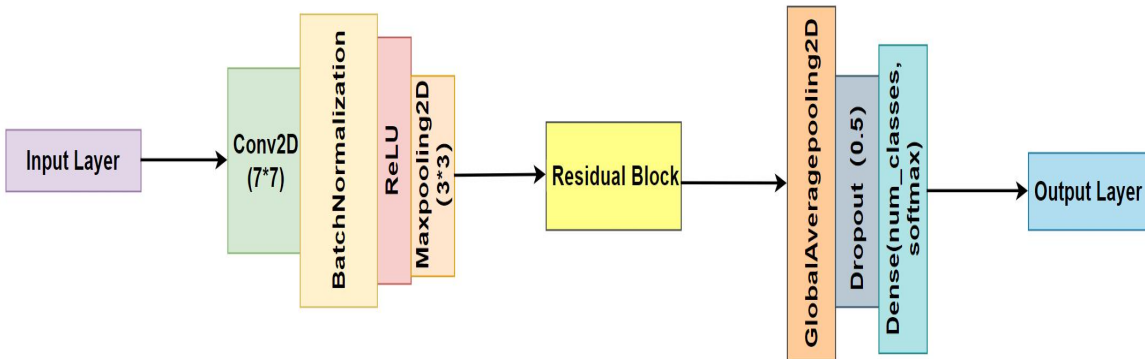


Figure 20. The proposed StackNet Structure

3.4.2 ResoNet (Resolution-aware module)

ResoNet is a resolution-aware module designed in this study to improve multi-scale feature extraction. As shown in Figure 21, it inspired by the Inception architecture,

processing features from different receptive fields in parallel to better detect anomalies with diverse structures.

This module is composed of four parallel branches, and each branch corresponds to a receptive field setting:

- A branch is used to extract local details, emphasizing information compression and rapid response;
- A structure focused on medium scale, suitable for identifying the contours of common defects;
- One is oriented towards large-scale regions and is used to capture relatively vague or diffusive anomalies;
- The last one combines pooling operations to enhance the understanding of spatial invariance.

After normalization and activation, outputs from all branches are concatenated to integrate multi-level features. This design allows the model to handle defects of varying sizes and shapes while maintaining a lightweight structure. Introducing ResoNet significantly improves the model's ability to recognize complex photovoltaic faults.

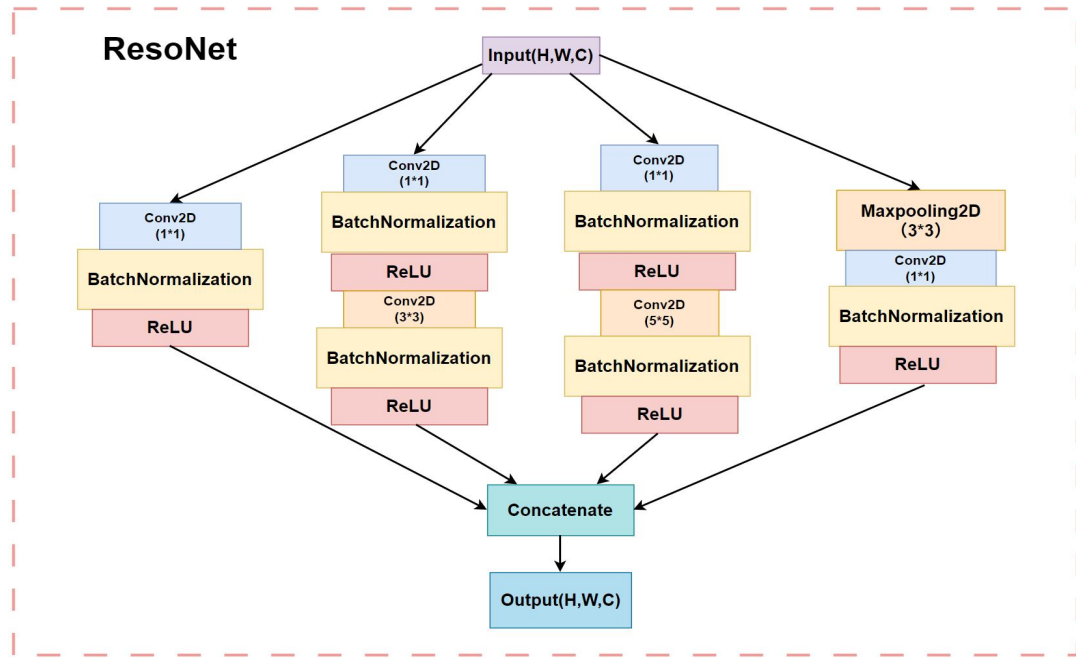


Figure 21. The Architecture of ResoNet

3.4.3 Attention Mechanism- Squeeze and Excitation (SE) module

The Squeeze-and-Excitation (SE) Block is a lightweight attention module designed to improve the representational power of a convolutional neural network by modeling interdependencies between channels [31]. It first applies global average pooling to each channel's feature map, compressing spatial dimensions into a single descriptor. Then, two fully connected layers are used: the first reduces the channel dimensions, and the second restores them, with a sigmoid activation function to model dependencies and adjust channel significance. The resulting weights are applied through element-wise multiplication, enhancing informative channels and suppressing less relevant ones. This attention mechanism displays in Figure 22 allows the model to focus on important features, improving its performance.

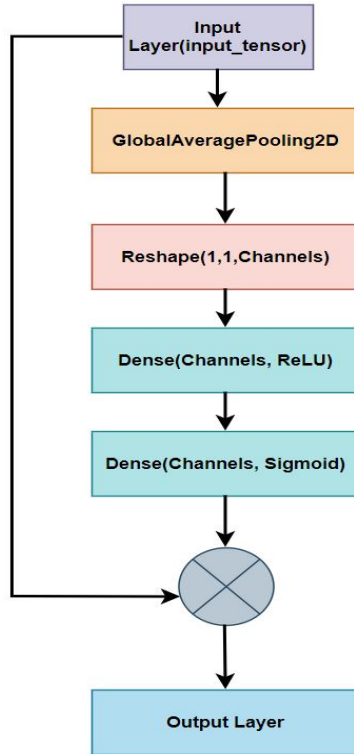


Figure 22. Attention Mechanism- Squeeze and Excitation (SE) module

3.4.4 SRNet (StackNet-ResoNet Model)

The SRNet model enhanced StackNet's residual block integrates a ResoNet module to better capture multi-scale features. Initially, it uses convolution, normalization, and activation to extract low-level features. The ResoNet module then processes features at

multiple scales in parallel, expanding the receptive field and improving sensitivity to image variations.

A subsequent convolutional layer refines the aggregated features and aligns them with the shortcut path. If there are discrepancies in spatial resolution or channel dimensions, the shortcut is adaptively adjusted. Finally, the merged output is activated and regularized to enhance generalization. The improved residual block of StackNet shows in Figure 23.

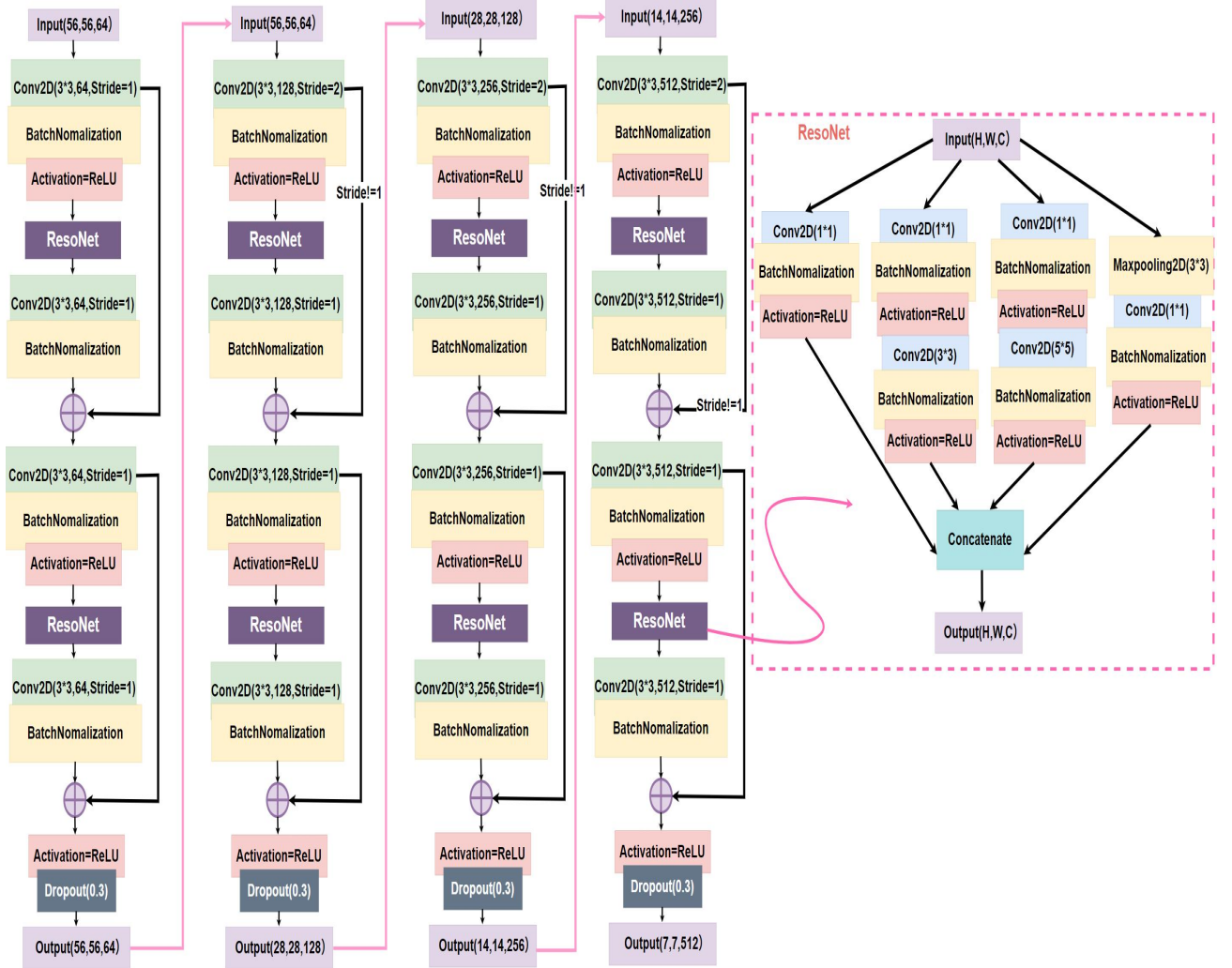


Figure 23. The Improved Residual Block Incorporating ResoNet

Overall, this modified block shows in Figure 24 retains residual learning efficiency and adds multi-scale feature extraction. It's highly effective for complex spatial pattern tasks like solar panel fault detection.

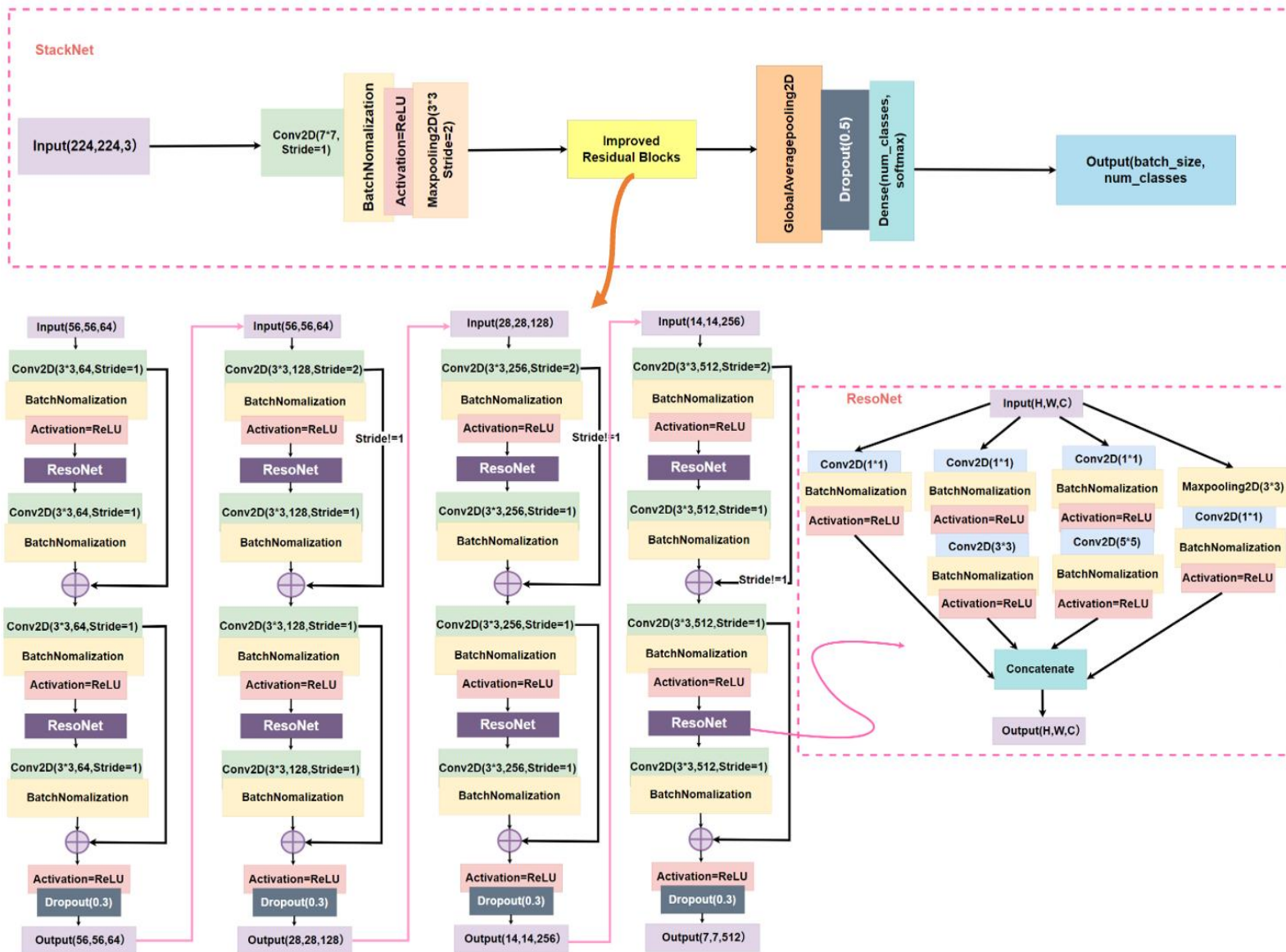


Figure 24. Overview of SRNet Structure

3.4.5 SARNet (StackNet-Attention Mechanism-ResoNet Model)

The proposed SARNet model extends the classical residual block to strengthen feature representation and training stability. It combines structural reuse and feature enhancement by retaining StackNet's residual learning, using convolution, batch normalization, and ReLU for effective gradient flow and deeper network training.

A ResoNet module as shown in Figure 25, is added to capture multi-scale features. It uses parallel convolutions and an attention mechanism to recalibrate channel responses, improving adaptability to complex patterns and enriching feature diversity.

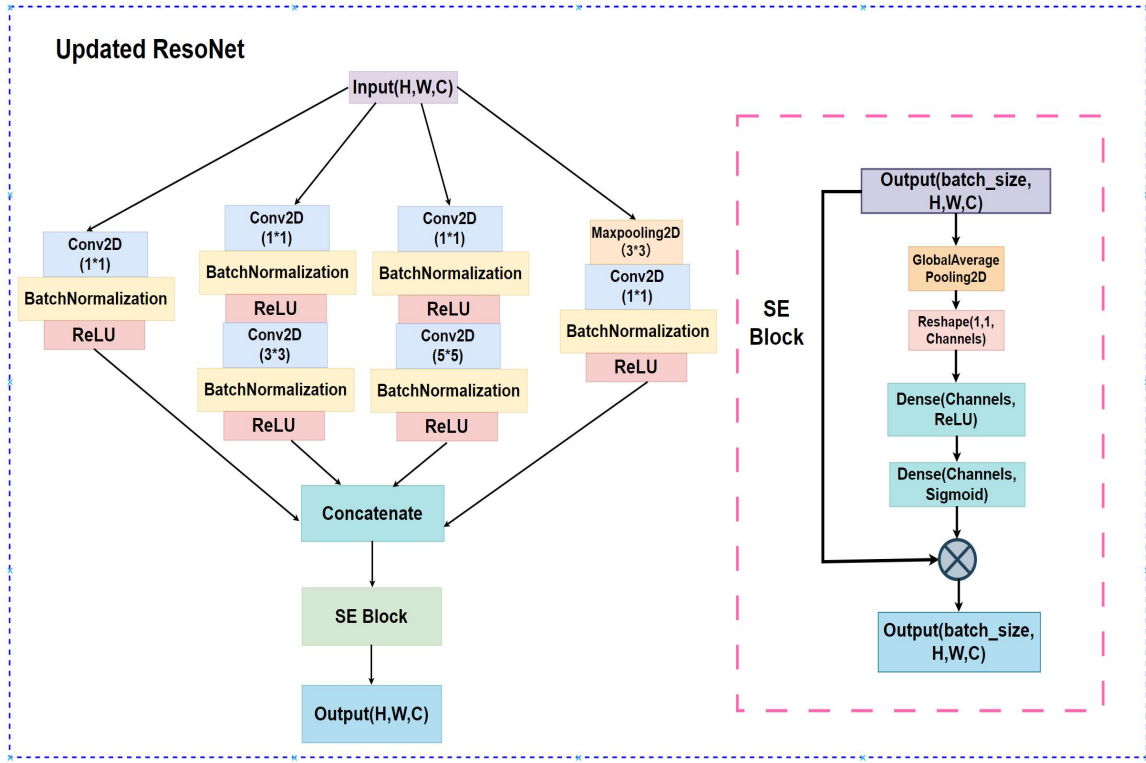


Figure 25. ResoNet Combined SE Block (Updated ResoNet)

Additionally, a Squeeze-and-Excitation (SE) attention mechanism to enhance feature maps, improving discriminative power and generalization. A 1×1 convolution ensures compatibility for residual addition when spatial or channel discrepancies occur. The output undergoes ReLU activation and dropout to reduce overfitting.

As shown in Figure 26 and Figure 27, SARNet combines multi-scale feature extraction (ResoNet with attention), adaptive attention (SE), and StackNet into a unified design, offering both expressive power and structural robustness.

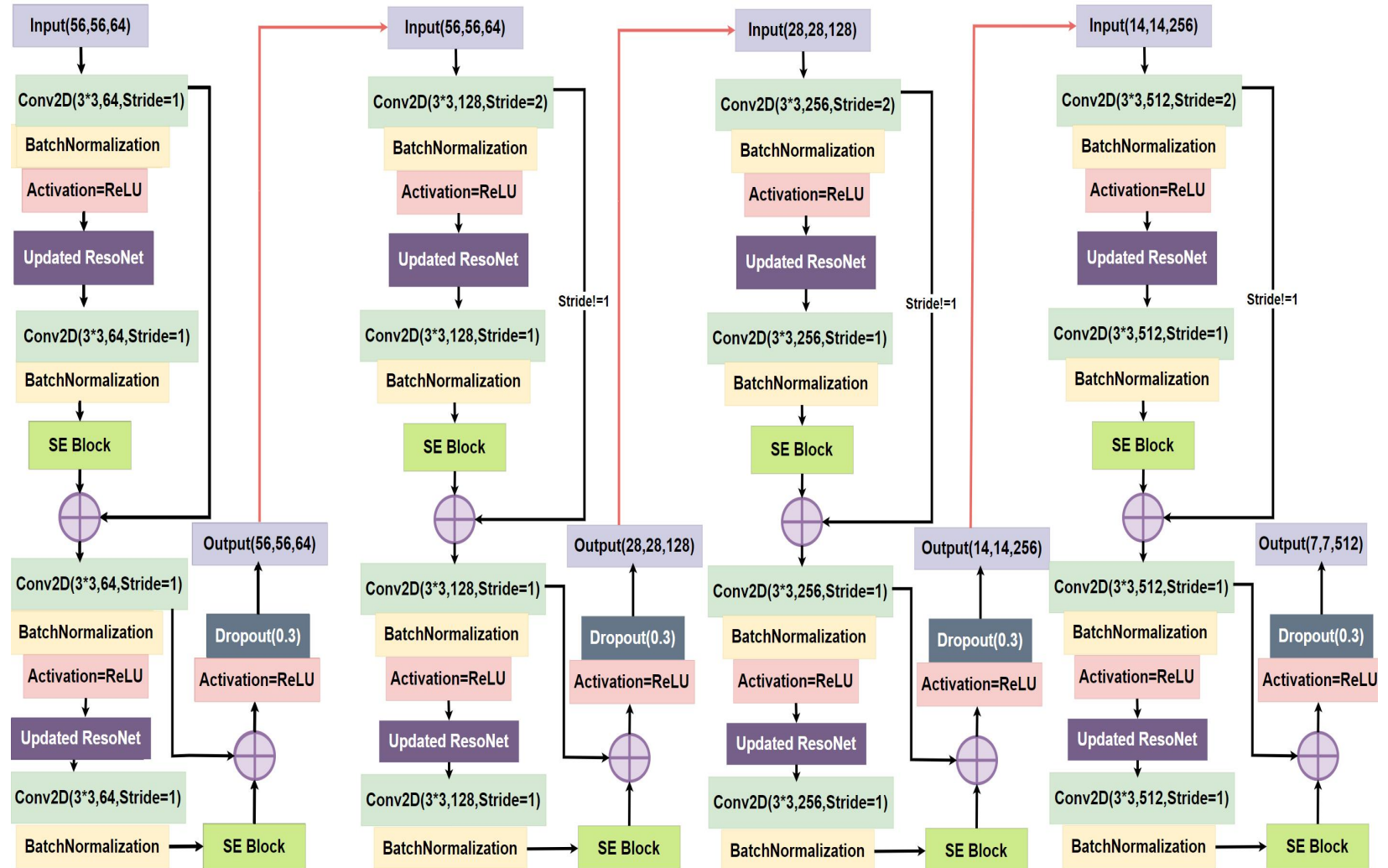


Figure 26. The Enhanced Residual Block Incorporating ResoNet and SE Block

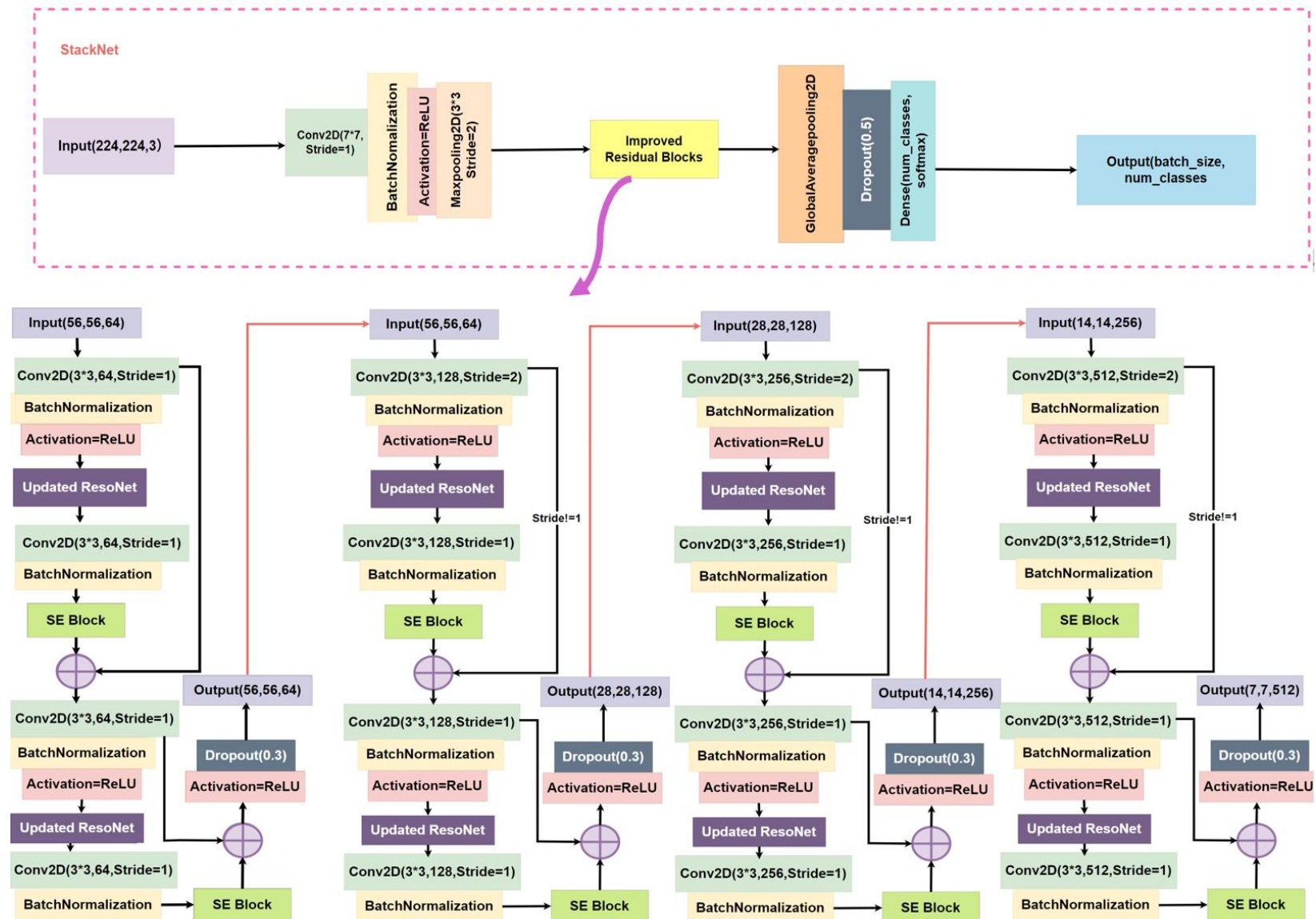


Figure 27. Overall Architecture of the SARNet

3.5 Experimental Setup & Technology

3.5.1 Experimental Setup

The experimental setup for training the model involves configuring key hyperparameters, the optimizer, and several callback functions to ensure effective learning and model generalization.

The model training process is configured with 100 epochs and an initial learning rate of 0.001, employing the Adam optimizer for its proven effectiveness in deep learning tasks. Batch sizes are adapted to task complexity and dataset characteristics: 438 for binary classification and 29 for six-class classification in Dataset 1, and 24 for Dataset 2. To enhance generalization and training efficiency, several callback mechanisms are employed. Early stopping monitors validation loss and terminates training after 30 consecutive epochs without improvement, restoring the best weights. The learning rate is adaptively reduced by a factor of 0.1 when no validation improvement is observed for 20 epochs, with a floor set at 0.000006 to maintain training stability. Model checkpointing ensures the best-performing weights, based on validation loss, are retained. These strategies collectively optimize convergence and mitigate overfitting, contributing to robust model performance.

3.5.2 Technology

The technology use in this project is displayed in Table 3:

Table 3. Summary of Relevant Technology involved in this project

Software	Framework	Tensorflow
	Language	Python
	Libraries	Numpy, Keras, Matplotlib, TensorFlow
Hardware	Central processing unit (CPU)	12th Gen Intel(R) Core (TM) i5-12500H 2.50 GHz
	Graphic Processing Unit (GPU)	Intel(R) Iris(R) Xe Graphics

3.6 Model Performance Evaluation Metrics

The 9 main evaluation metrics used in this experiment were: Loss, Accuracy, Specificity, Recall (Sensitivity), Precision, F1 score (Dice Score), Confusion Matrix, ROC-AUC curve and Precision-Recall curve. Each of these 9 metrics is described below.

3.6.1 Loss Function

Binary Cross-Entropy function is used, it is a loss function suitable for binary classification tasks, which guides the optimization process by measuring the difference between the predicted probability of the model and the actual label.

$$\text{Binary Cross - Entropy Loss} = -\frac{1}{N} \sum_{i=1}^N [y_i \log(p_i) + (1 - y_i) \log(1 - p_i)] \quad (1)$$

- y_i : the true label of the sample, taking values of 0 or 1.
- p_i : the model's predicted probability for the i-th sample being in class 1, typically output by the sigmoid activation function.
- N: the total number of samples.

Sparse classification cross entropy measures the quality of a model's predictions by taking the logarithm of its prediction probability for the correct category and taking a negative value. It is suitable for situations where the label is an integer representing the category index.

$$\text{Sparse Categorical Cross - Entropy} = -\sum_{i=1}^C y_i \log(p_i) \quad (2)$$

- y_i : the true label of the sample.
- p_i : the probability of the model predicting the category.
- C: the total number of categories in the classification task.

3.6.2 Accuracy

The proportion of correctly predicted samples by the model to the total sample size.

$$\text{Accuracy}(A, B) = \frac{1}{n} \sum_{i=0}^n \mathbf{1}_{(A_i=B_i)} \quad (3)$$

- A: the predicted values or predicted labels for the samples.
- B: the true or ground truth labels for the samples.
- n: the total number of samples.

3.6.3 Specificity (SP)

Specificity is used to measure the ability of classification models to correctly identify negative class samples.

$$\text{Specificity (SP)} = \frac{TN}{TN+FP} \quad (4)$$

- TN (True Negatives): The number of samples correctly predicted as negative by the model.
- FP (False Positives): The number of samples incorrectly predicted as positive by the model.

3.6.4 Sensitivity/Recall (SE)

Sensitivity/Recall is an indicator that measures how many actual positive class samples a classification model can recognize.

$$\text{Sensitivity/Recall (SE)} = \frac{TP}{TP+FN} = \frac{TP}{P} \quad (5)$$

- TP (True Positive): This represents the number of positive samples that were correctly identified as positive by the model.
- FN (False Negative): This represents the number of positive samples that were incorrectly identified as negative by the model.
- P: This is the total number of actual positive samples in the dataset, which is the sum of TP and FN.

3.6.5 Precision

Precision measures the proportion of samples predicted as positive by the model that are correct.

$$\text{Precision} = \frac{TP}{TP+FP} \quad (6)$$

3.6.6 F1 Score (Dice Score)

F1 Score is the harmonic mean of precision and recall.

$$F1 \text{ Score} = 2 \times \frac{\text{Precision} \times \text{Recall}}{\text{Precision} + \text{Recall}} \quad (7)$$

3.6.7 Confusion Matrix

Confusion Matrix like Table 11 is a tool used to evaluate the performance of classification models, especially for binary classification problems. It compares the

predicted results of the model with the actual labels to form a matrix that displays four possible outcomes:

	Predicted Positive (1)	Predicted Negative (0)
Actual Positive (1)	True Positive (TP)	False Negative (FN)
Actual Negative (0)	False Positive (FP)	True Negative (TN)

Table 4. Outcomes of Confusion Matrix

3.6.8 Receiver Operating Characteristic (ROC)

True Positive Rate (TPR): TPR represents the proportion of samples that are correctly predicted as positive among all samples that are actually positive:

$$TPR = \frac{TP}{TP+FN} \quad (8)$$

False Positive Rate (FPR): FPR represents the proportion of samples that are incorrectly predicted as positive among all samples that are actually negative:

$$FPR = \frac{FP}{FP+TN} \quad (9)$$

AUC (Area Under Curve): AUC represents the area under the ROC curve, and its value ranges from 0 to 1. The closer the AUC is to 1, the better the classification performance of the model.

3.6.9 Precision-Recall (PR)

The Precision-Recall curve shows the changes in precision and recall under different decision thresholds. Precision and recall will vary under different thresholds, so the Precision-Recall curve helps analyze the performance of the model under various decision boundaries. The PR curve plots the changes in recall and precision, and evaluates the performance of the model on a specific class through the area (AUC-PR).

3.7 Project Version Management

To ensure that no project document or code is misplaced or mismanaged, the following application will be used to effectively manage all documents.

URL is as follow: <https://github.com/Sienna-L/Deep-Learning-Project.git>

Chapter 4 Implementation and Result

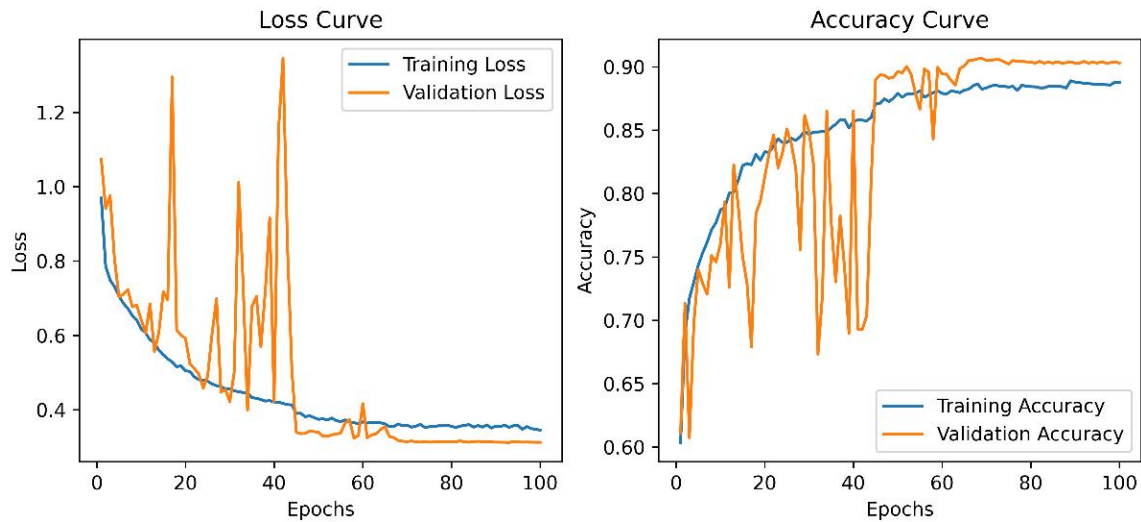
This study compares three CNN architectures under identical training settings to ensure fairness. StackNet employs residual connections for deep feature extraction and stable training. SRNet builds on StackNet by adding ResoNet modules to capture multi-scale spatial features. SARNet further introduces attention mechanisms to highlight task-relevant regions. All models are trained for 100 epochs at an initial learning rate of 0.001 using the Adam optimizer. Batch sizes are task-specific: 438 for binary classification, 29 for the six-class task in dataset 1, and 24 for binary classification in dataset 2. To enhance generalization, training incorporates early stopping after 30 stagnant epochs, checkpointing based on validation loss, and a learning rate reduction (by 0.1 after 20 stagnant epochs, with a minimum of 0.000006). These configurations ensure stable training and optimal model performance.

4.1 Experiment 1 - StackNet

The StackNet was trained on two datasets: Dataset 1 (Infrared Solar Modules) for both binary and 6-class classification tasks, and Dataset 2 (ELPV) for binary classification. This evaluation not only assesses StackNet's performance across varying datasets and classification tasks, but also provides insights into which dataset facilitates better model optimization.

4.1.1 StackNet on Dataset 1- Binary Class

In the binary classification task on Dataset 1, StackNet achieved the highest overall performance. As shown in Figure 28, The training loss reached 0.3492, while the validation loss was slightly higher at 0.3671, indicating minimal overfitting. In terms of accuracy, the model achieved 88.76 percent on the training set and 88.27 percent on the validation set, showing strong consistency. In Table 5 the test set achieved 88.3% accuracy and a loss of 0.367, confirming its effectiveness on unseen data.



(a) Train Loss = 0.3492, Val Loss = 0.3671 (b) Train ACC = 0.8876, Val ACC = 0.8827

Figure 28. (a) and (b) present StackNet model Accuracy and Loss Curve on Dataset 1 (Binary Class)

The model StackNet demonstrates strong classification performance with a high number of correct predictions. As shown in Figure 29, it correctly identified 1,373 true positives and 1,274 true negatives, while misclassifying 127 false positives and 226 false negatives. These results indicate a balanced performance with relatively low error rates, suggesting the model is effective at distinguishing between the two classes.

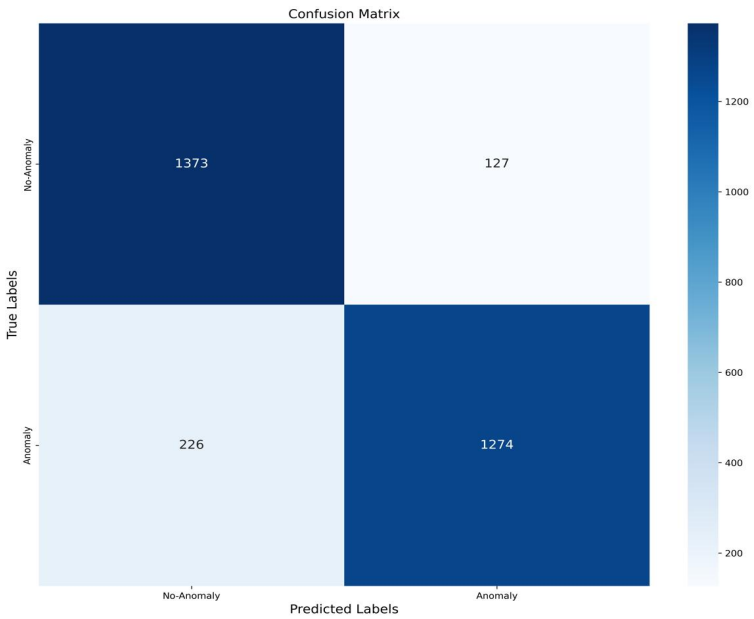
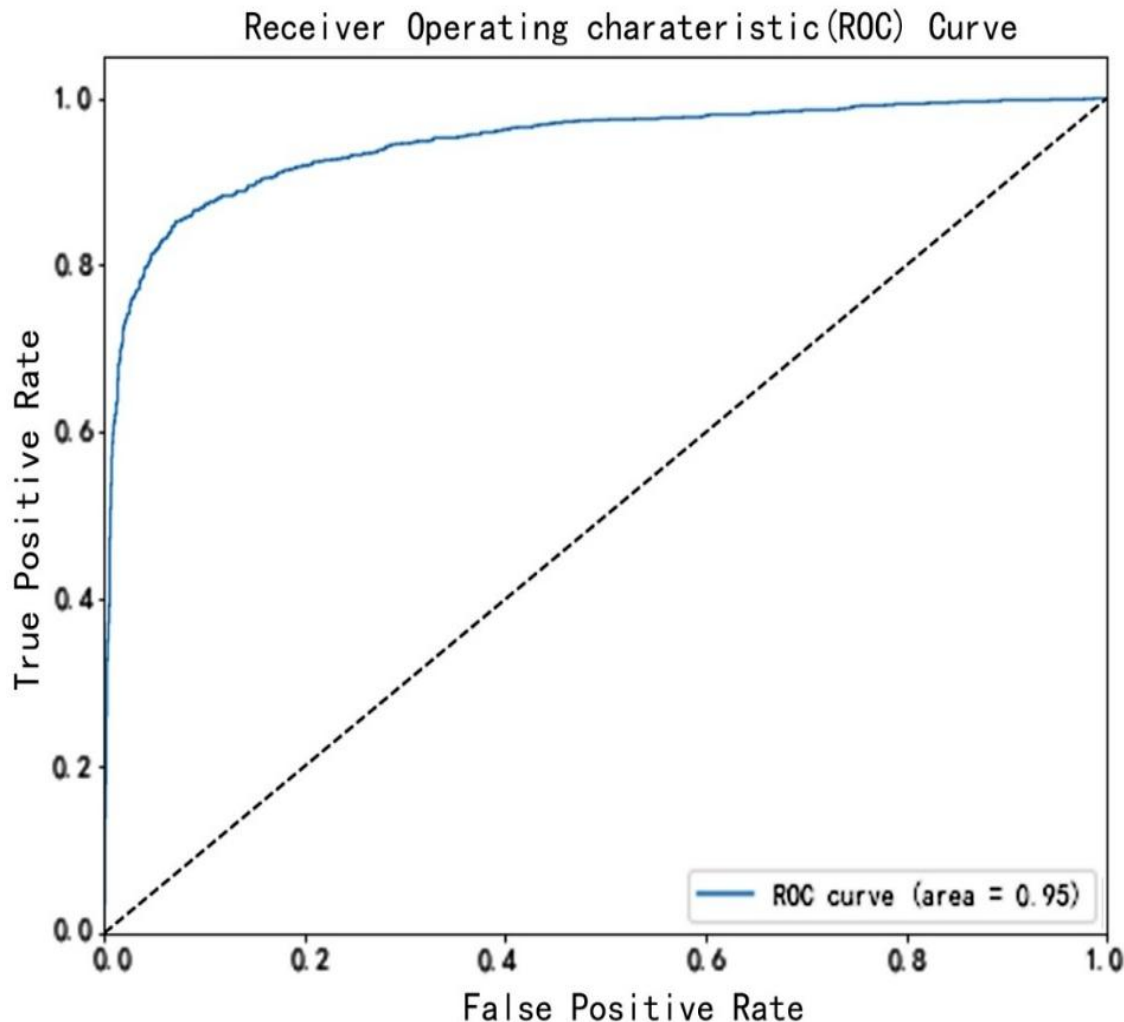


Figure 29. StackNet model Confusion Matrix for Dataset 1- Binary Class

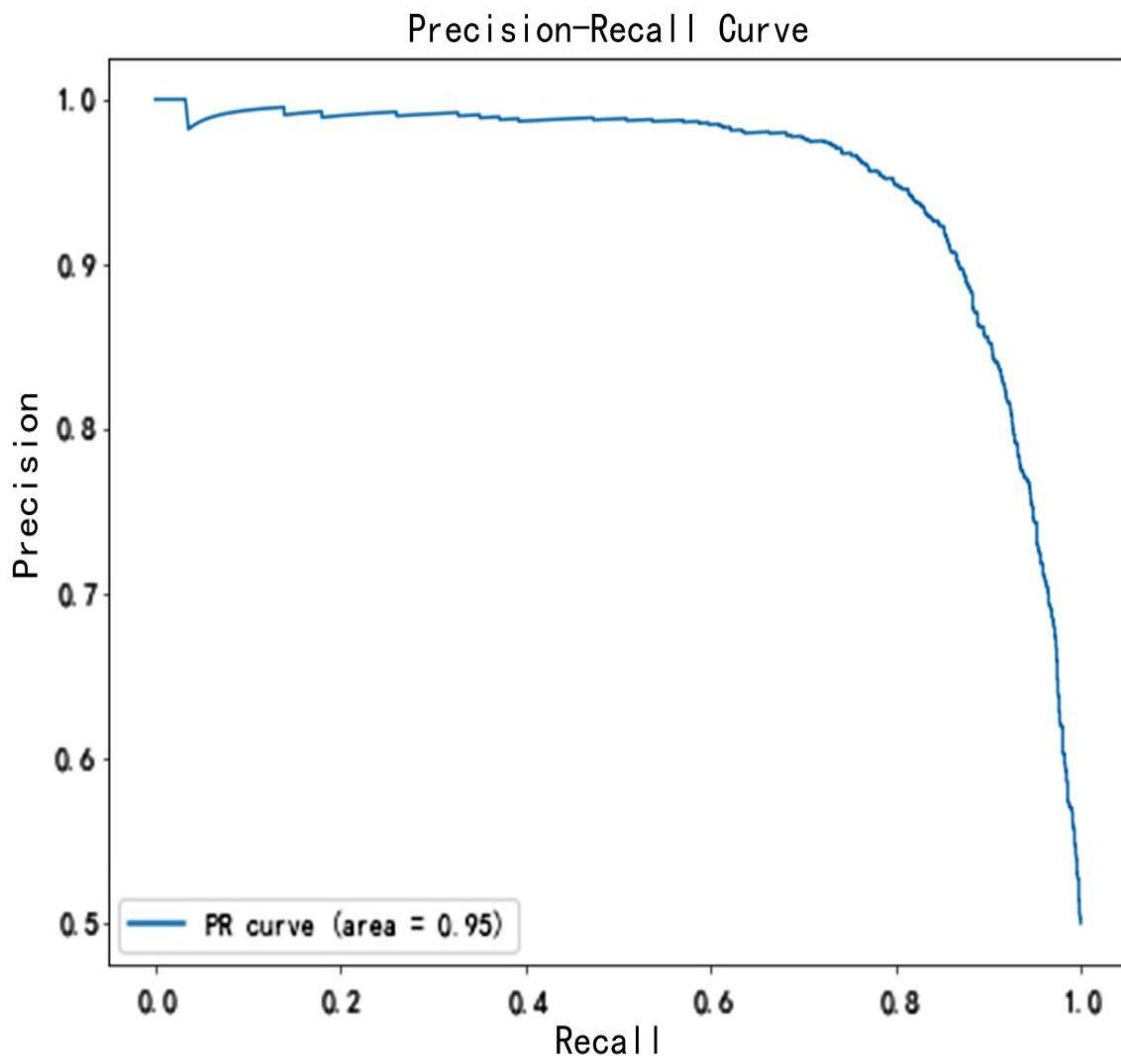
The model StackNet achieved a ROC-AUC score of 0.95, as shown in Figure 30, indicating excellent discriminatory power between the positive and negative classes. This high value reflects the model's ability to maintain a strong balance between sensitivity and specificity across various threshold settings, suggesting reliable overall performance.



(c) ROC-AUC = 0.95

Figure 30. (c) present StackNet model ROC Curve on Dataset 1- Binary Class

As shown in Figure 31, the StackNet model achieved a PR-AUC score of 0.95 in dataset 1 binary class, demonstrating excellent precision-recall performance. This indicates that the model maintains high precision while effectively capturing the majority of positive cases, making it well-suited for handling class imbalance and minimizing false positives and false negatives.

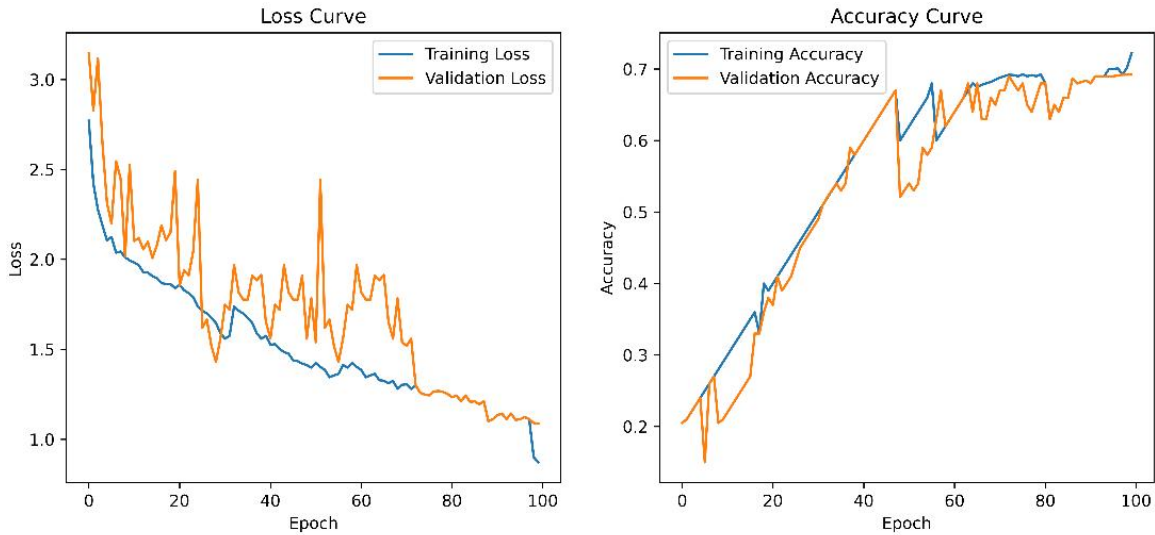


(d) PR-AUC = 0.95

Figure 31. (d) present PR Curve on Dataset 1- Binary Class

4.1.2 StackNet on Dataset 1- 6-Class

In contrast, the 6-class classification task on Dataset 1 posed greater challenges. As reflected in Figure 32, the training loss was 0.982 and the validation loss increased to 1.0872, indicating a moderate gap that may suggest some overfitting. The training accuracy reached 73.22 percent, while the validation and test accuracies both stood at 69.22 percent. The test loss matched the validation loss at 1.0872 from Table 5, confirming consistent but limited generalization. These results suggest that the model struggled to capture the complexity of the multi-class task compared to binary classification.



(e) Train Loss = 0.982, Val Loss = 1.0872 (f) Train ACC = 0.7322, Val ACC = 0.6922

Figure 32. (e) and (f) present StackNet model Accuracy and Loss Curve on Dataset 1 (6-Class)

The model shows varied performance across solar panel fault types, as shown in Figure 33. The model demonstrates strong performance in detecting class 2 diode and class 3 shadowing faults but faces challenges with class 6 cracking and class 4 cell faults. Class 1 vegetation and class 4 cell faults show some confusion with other categories. Overall, the model performs well on diode and shadowing but needs improvement for cracking and cell faults.

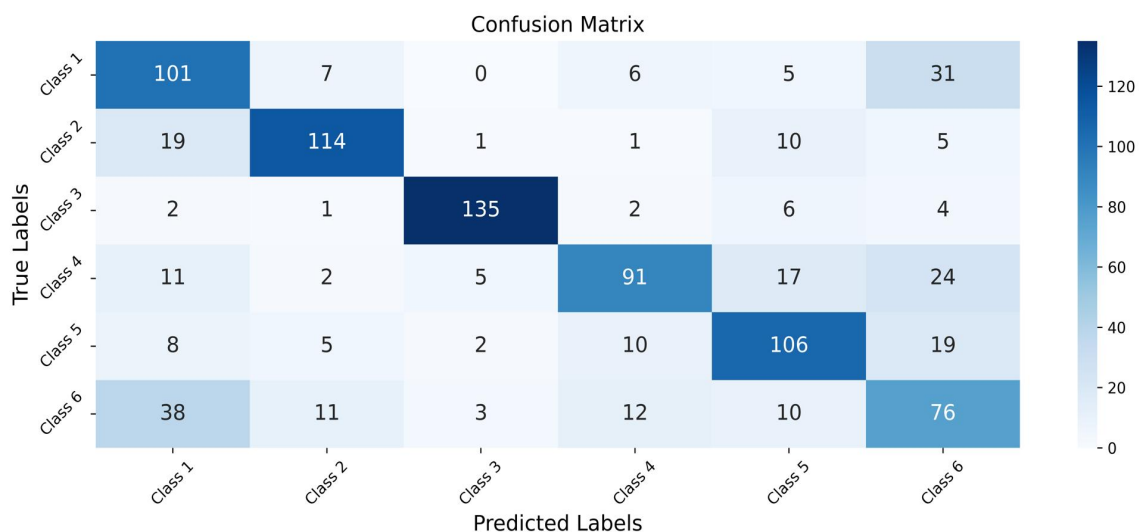


Figure 33. StackNet model Confusion Matrix for Dataset 1(6-calss)

As shown in Figure 34, the ROC curve shows a multi-class classification model's performance across six classes. The dashed diagonal line represents a random classifier. Class Shadowing has the highest AUC of 0.99. Vegetation, Diode, Cell, and Offline-Module have AUC values above 0.90. Class Cracking has a lower but acceptable AUC of 0.86. Overall, the model shows good discriminatory power, with Shadowing performing best.

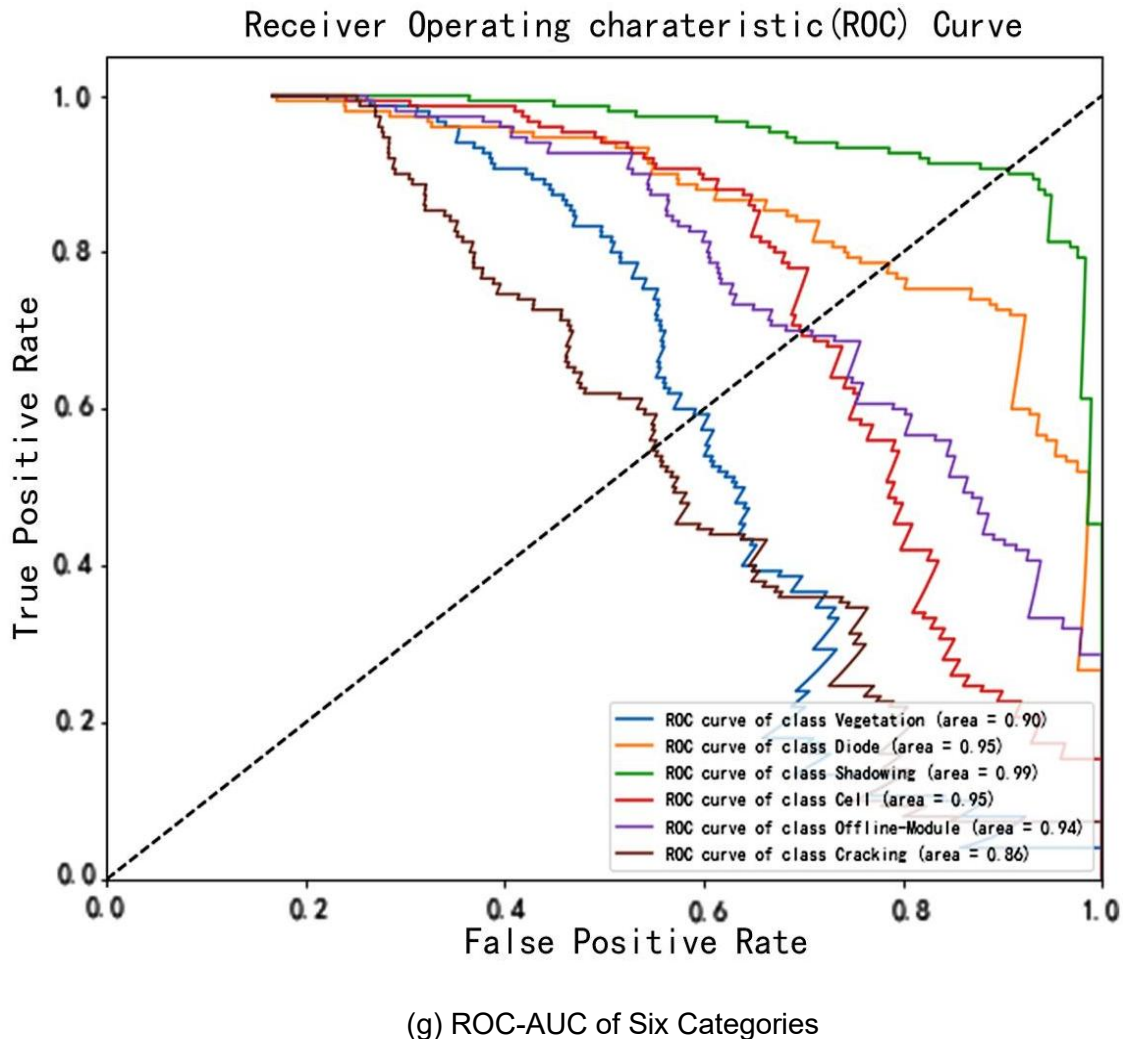


Figure 34. (g) present StackNet model ROC Curve on Dataset 1(6-Class)

Figure 35 presents the Precision-Recall curves for six classes in the multi-class model. Shadowing achieves the highest AUC value of 0.96, indicating excellent detection performance. Diode and Offline-Module follow with AUC values of 0.88 and 0.80, respectively. In contrast, Cracking and Vegetation yield lower AUC values of 0.59 and

0.62, highlighting their classification difficulty. Overall, the model performs well, though improvements are needed for specific fault types.

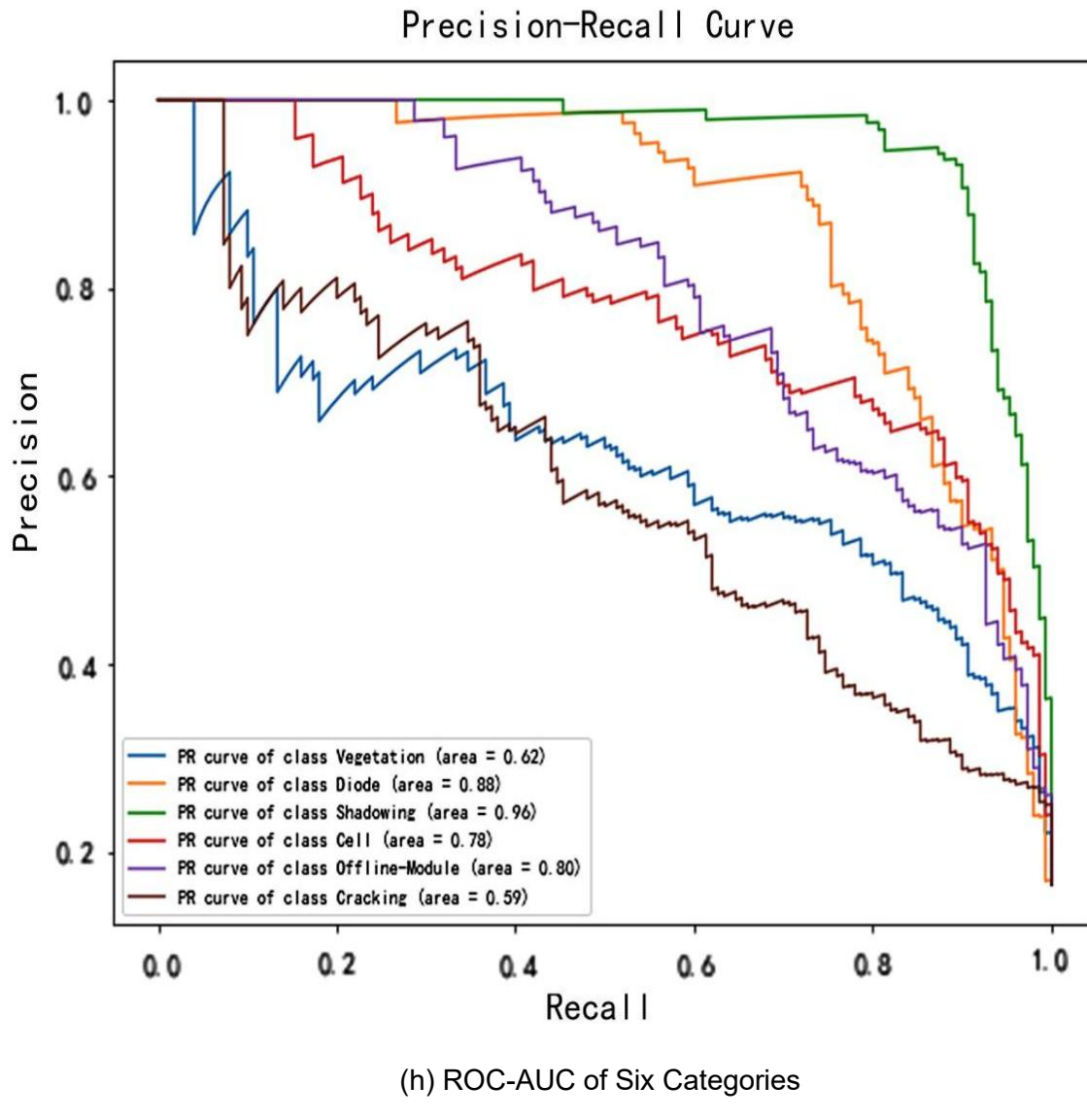
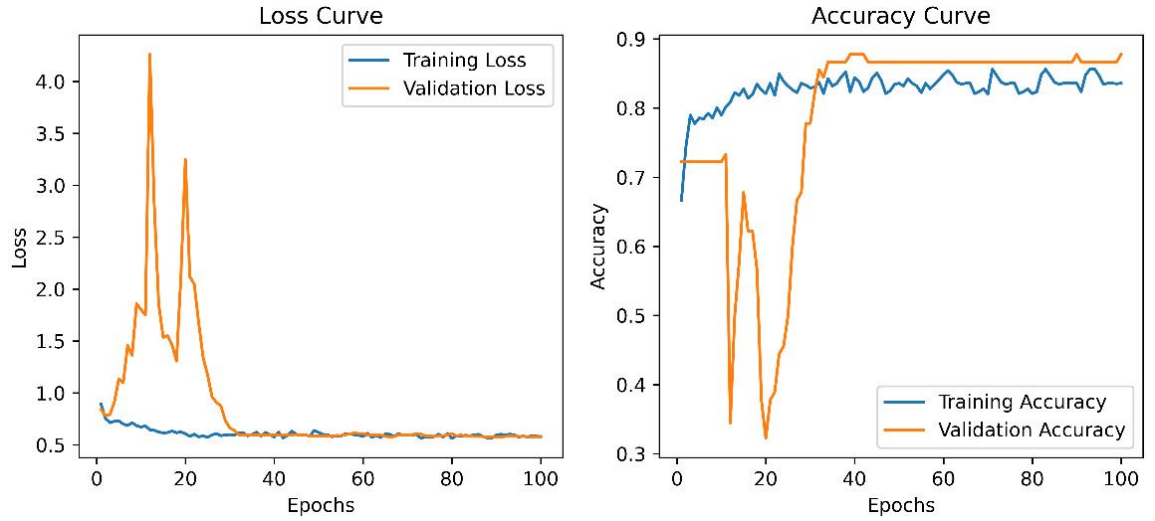


Figure 35. (h) present StackNet model PR Curve on Dataset 1(6-Class)

4.1.3 StackNet on Dataset 2- Binary Class

For Dataset 2, in the binary classification setting, StackNet continued to perform reliably. In Figure 36, the model shows a training loss of 0.5812 and a validation loss of 0.5744, indicating good generalization. With a training accuracy of 0.8358, validation accuracy of 0.8788, and a test accuracy of 0.8513 shown in Table 5, alongside a test loss of 0.680.



(i) Train Loss = 0.5812, Val Loss = 0.5744

(j) Train ACC = 0.8358, Val ACC = 0.8788

Figure 36. (i) and (j) present StackNet model Accuracy and Loss Curve Dataset 2

(Binary Class)

The model shows strong binary classification performance. In Figure 37, it correctly identified 47 true positives and 18 true negatives, while producing only 5 false positives and 4 false negatives. These results indicate high accuracy, with the model effectively distinguishing between the two classes and maintaining a low error rate.

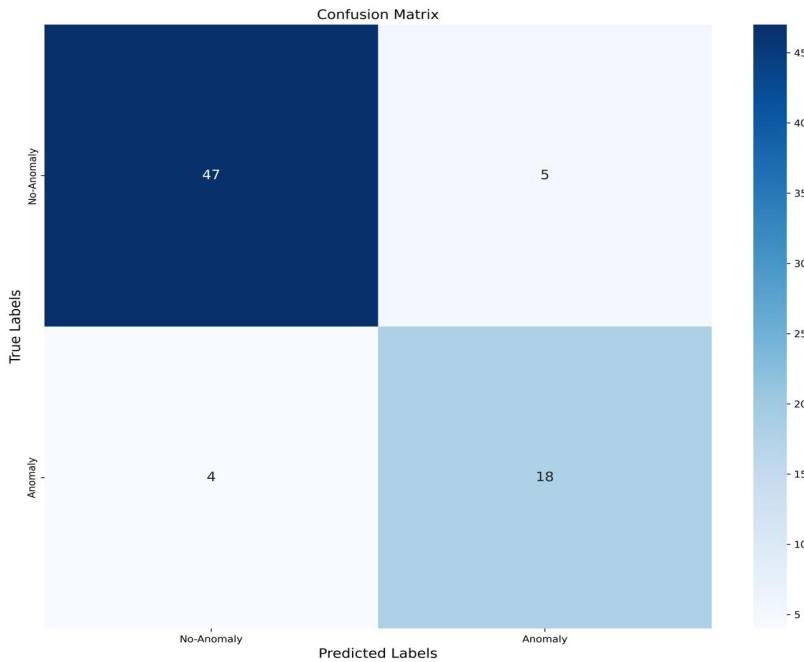
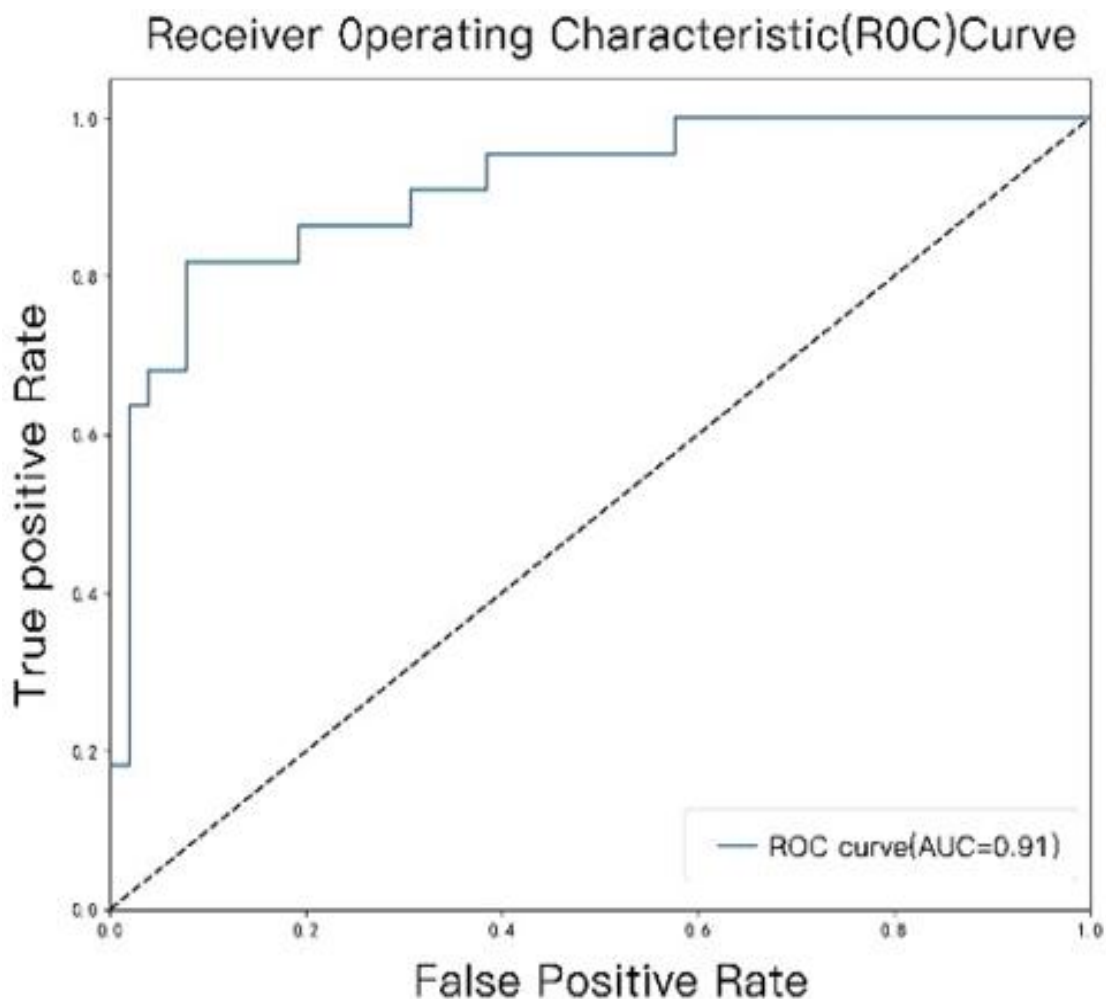


Figure 37. StackNet model Confusion Matrix for Dataset 2(Binary Class)

As shown in Figure 38, the model achieved a ROC-AUC score of 0.91, indicating strong ability to distinguish between the two classes. This high value reflects a good balance between sensitivity and specificity across different thresholds, demonstrating reliable overall classification performance.



(k) ROC-AUC = 0.91

Figure 38. (k) present StackNet model ROC Curve on Dataset 2(Binary Class)

The model achieved a PR-AUC score of 0.91 shown in Figure 39, indicating strong performance in precision and recall. This suggests the model effectively identifies positive cases while keeping false positives low, making it well-suited for tasks with class imbalance.

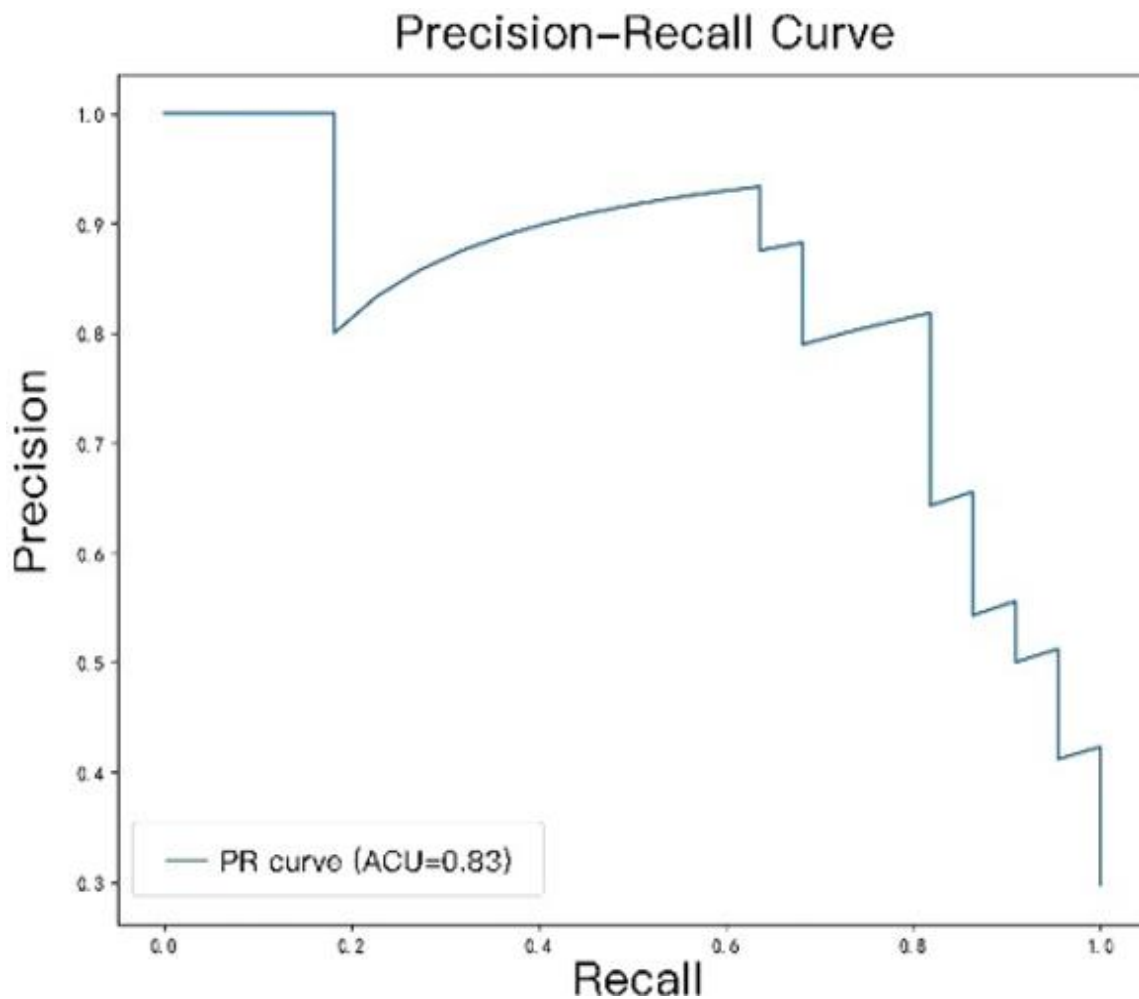


Figure 39. (I) present StackNet model PR Curve on Dataset 2(Binary Class)

Results and model for dataset 1 and dataset 2 across different classification tasks details are presented in Table 5 and Table 6.

Table 5. StackNet Model Performance Metrics-1

Dataset	Class	Loss	Accuracy	Recall	Precision	F1-Score
Dataset 1	2-class	0.3671	0.8827	0.8326	0.9251	0.8764
Dataset 1	6-class	1.0872	0.6922	0.6922	0.702	0.695
Dataset 2	2-class	0.571	0.878	0.818	0.783	0.800

Table 6. StackNet Model Performance Metrics-2

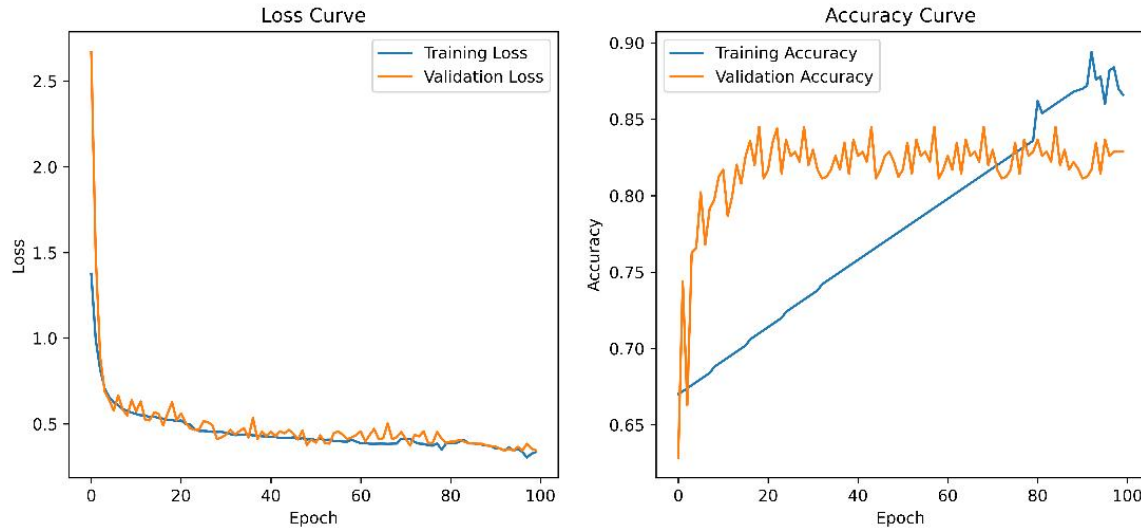
Dataset	Class	Specificity	ROC-AUC	PR-AUC
Dataset 1	2-Class	0.9326	0.9516	0.955
Dataset 1	6-Class	Cell:0.706 Cracking:0.506 Diode:0.76 Offline-Module:0.7066 Shadowing:0.90 Vegetation:0.673	Cell:0.90 Cracking:0.86 Diode:0.95 Offline-Module:0.94 Shadowing:0.99 Vegetation:0.90	Cell:0.78 Cracking:0.59 Diode:0.88 Offline-Module:0.80 Shadowing:0.96 Vegetation:0.62
Dataset 2	2-Class	0.9038	0.912	0.832

4.2 Experiment 2 - SRNet

The SRNet model is an architecture that combines StackNet with ResoNet was evaluated on two datasets: Dataset 1(Infrared Solar Module) for both binary and multi-class classification tasks, and Dataset 2(ELPV) for binary classification. This comprehensive evaluation assesses SRNet's ability to generalize across distinct data distributions and task complexities, while also identifying which dataset contributes more effectively to model optimization.

4.2.1 SRNet on Dataset 1- Binary Class

On Dataset 1, SRNet achieved its best performance in the binary classification task. As shown in Figure 40, the model demonstrates stable and effective learning. The training loss is 0.3676, and the validation loss is slightly higher at 0.4463, suggesting limited overfitting. Training accuracy reaches 86.38 percent, with validation accuracy at 82.88 percent, showing good consistency. As shown in Table 7, on the test set the model achieves a higher accuracy of 88.07 percent and a lower loss of 0.3467, confirming strong generalization and reliable performance on unseen data.



(m) Train Loss = 0.3676, Val Loss = 0.4463 (n) Train ACC = 0.8638, Val ACC = 0.8288

Figure 40. (m) and (n) present SRNet model's Accuracy and Loss Curve on Dataset 1
(Binary Class)

The model demonstrates reliable binary classification performance. As shown in Figure 41, it correctly predicts 1,373 true positives and 1,274 true negatives, indicating strong overall accuracy. With 127 false positives and 226 false negatives, the error rates remain moderate, suggesting the model effectively distinguishes between the two classes while leaving room for improvement in reducing missed positive cases.

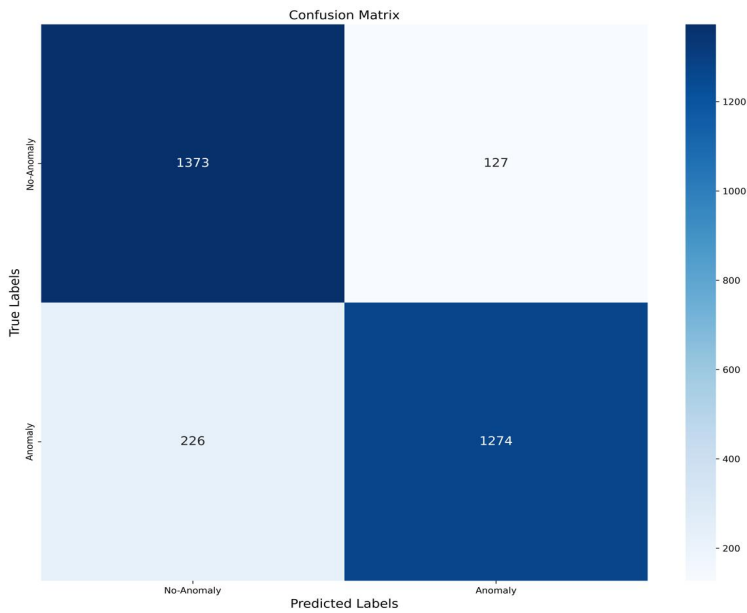
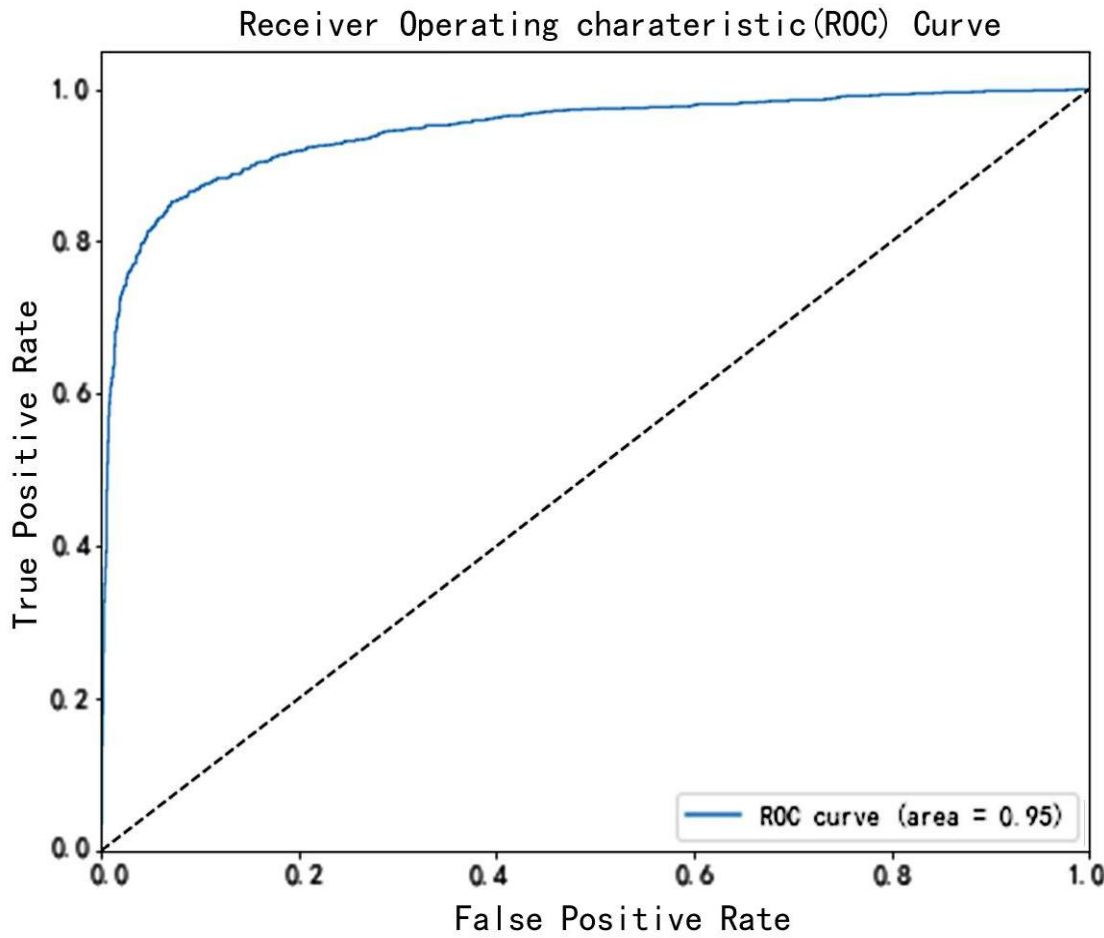


Figure 41. SRNet Model Confusion Matrix for Dataset 1- Binary Class

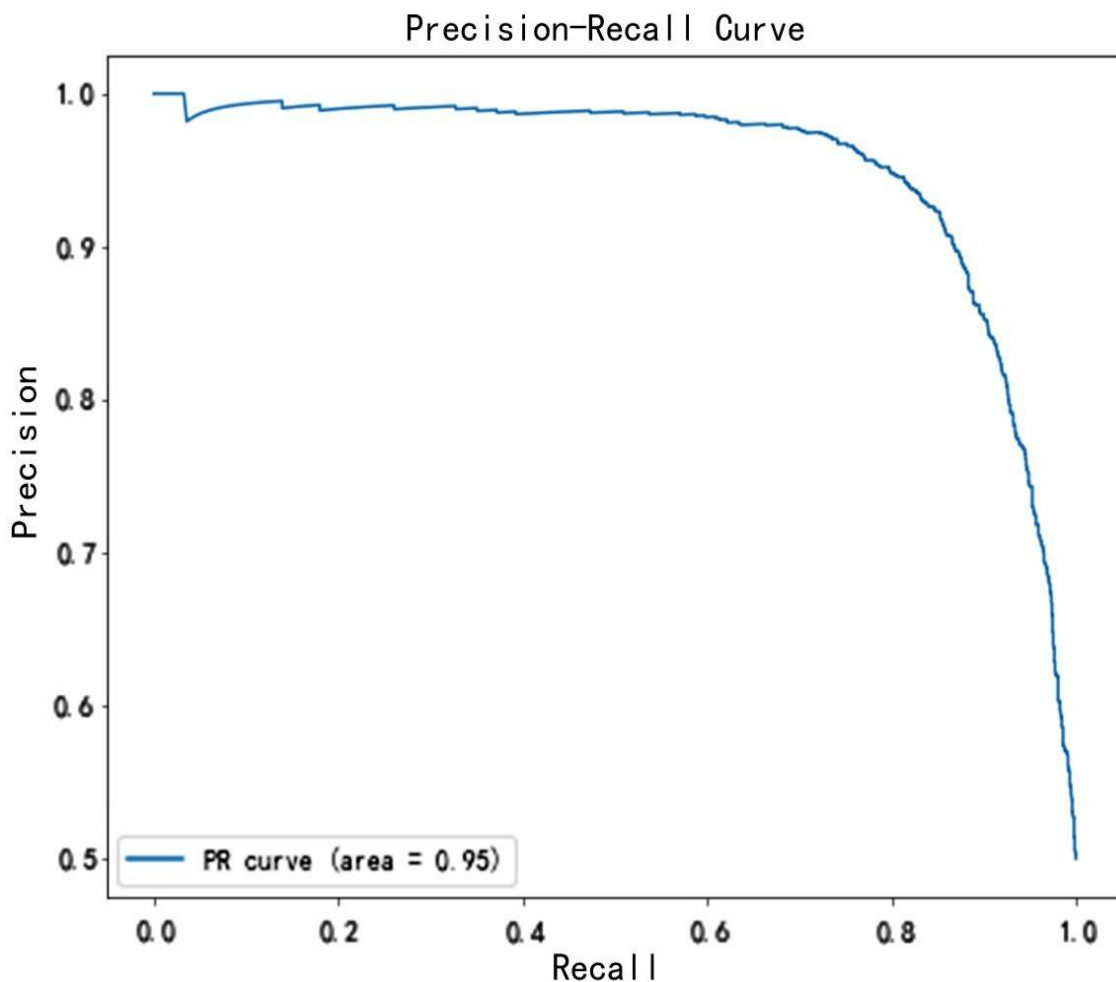
As shown in Figure 42, the ROC-AUC score of 0.95 reflects the model's strong discriminative capability. It demonstrates that the model consistently ranks positive instances higher than negative ones, maintaining reliable performance across various decision thresholds. This suggests a high level of classification confidence and robustness.



(o) ROC-AUC = 0.95

Figure 42. (o) present SRNet model ROC and PR Curve on Dataset 1(Binary Class)

As shown in Figure 43, the PR-AUC score of 0.95 indicates that the model maintains high precision while effectively capturing the majority of true positives. This strong performance suggests the model is well-suited for handling imbalanced data, with minimal trade-off between precision and recall.

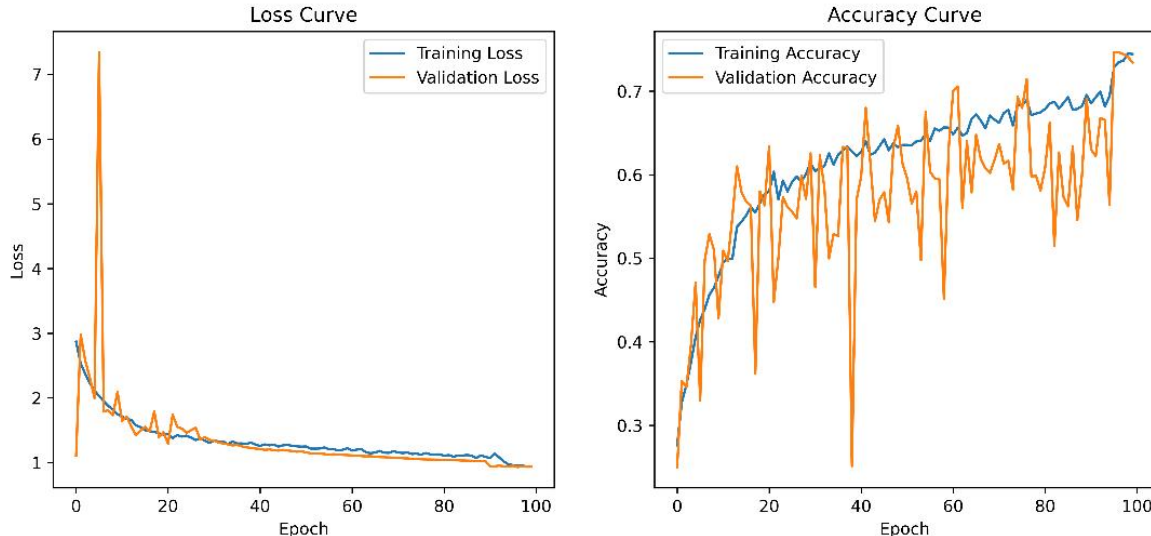


(p) PR-AUC = 0.95

Figure 43. (p) present SRNet model ROC and PR Curve on Dataset 1(Binary Class)

4.2.2 SRNet on Dataset 1- 6-Class

In the 6-class classification task on Dataset 1, SRNet also delivered balanced overall results. As shown in Figure 44, the model shows a training loss of 0.9397 and validation loss of 0.9380, indicating consistent performance with minimal overfitting. Training accuracy is 0.7745, validation accuracy is 0.7644, and from Table 7 test accuracy is 0.7522, reflecting stable generalization. The test loss of 0.9061 confirms the model's reliable performance on unseen data.



(q) Train Loss = 0.9397, Val Loss = 0.9380 (r) Train ACC = 0.7745, Val ACC = 0.7644

Figure 44. (q) and (r) present SRNet model's Accuracy and Loss Curve on Dataset 1

(6-Class)

From the Figure 45 confusion matrix analysis, Class 1 cell shows moderate performance with 93 true positives, 61 false positives, and 57 false negatives. Class 2 cracking achieves strong results with 120 true positives and only 14 false positives, indicating accurate detection. Class 3 diode performs best, with 142 true positives and just 11 false positives, showing excellent classification. Class 4 offline-Module also performs well with 128 true positives but suffers from a higher number of 41 false positives. Class 5 shadowing achieves 98 true positives and 52 false negatives, indicating some difficulty in recall. Class 6 vegetation records 96 true positives and 61 false positives, showing a pattern similar to cell, with room for improvement in precision.

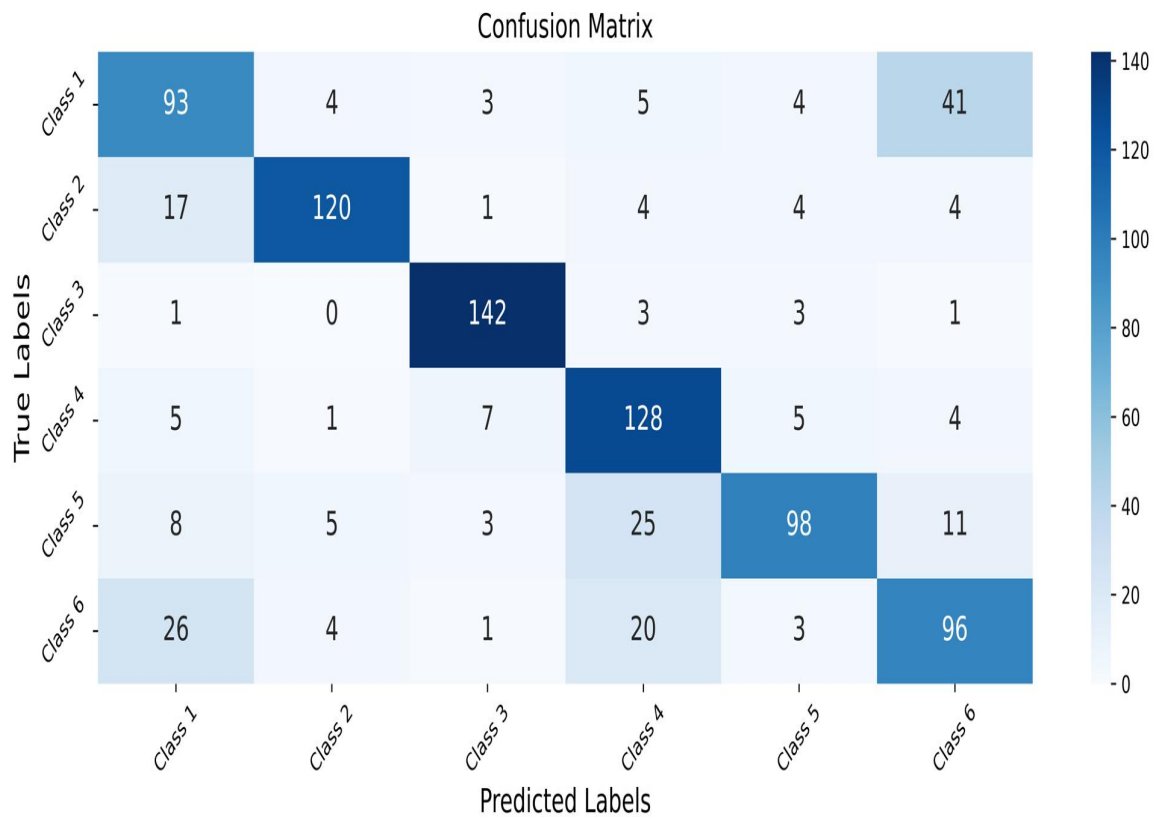
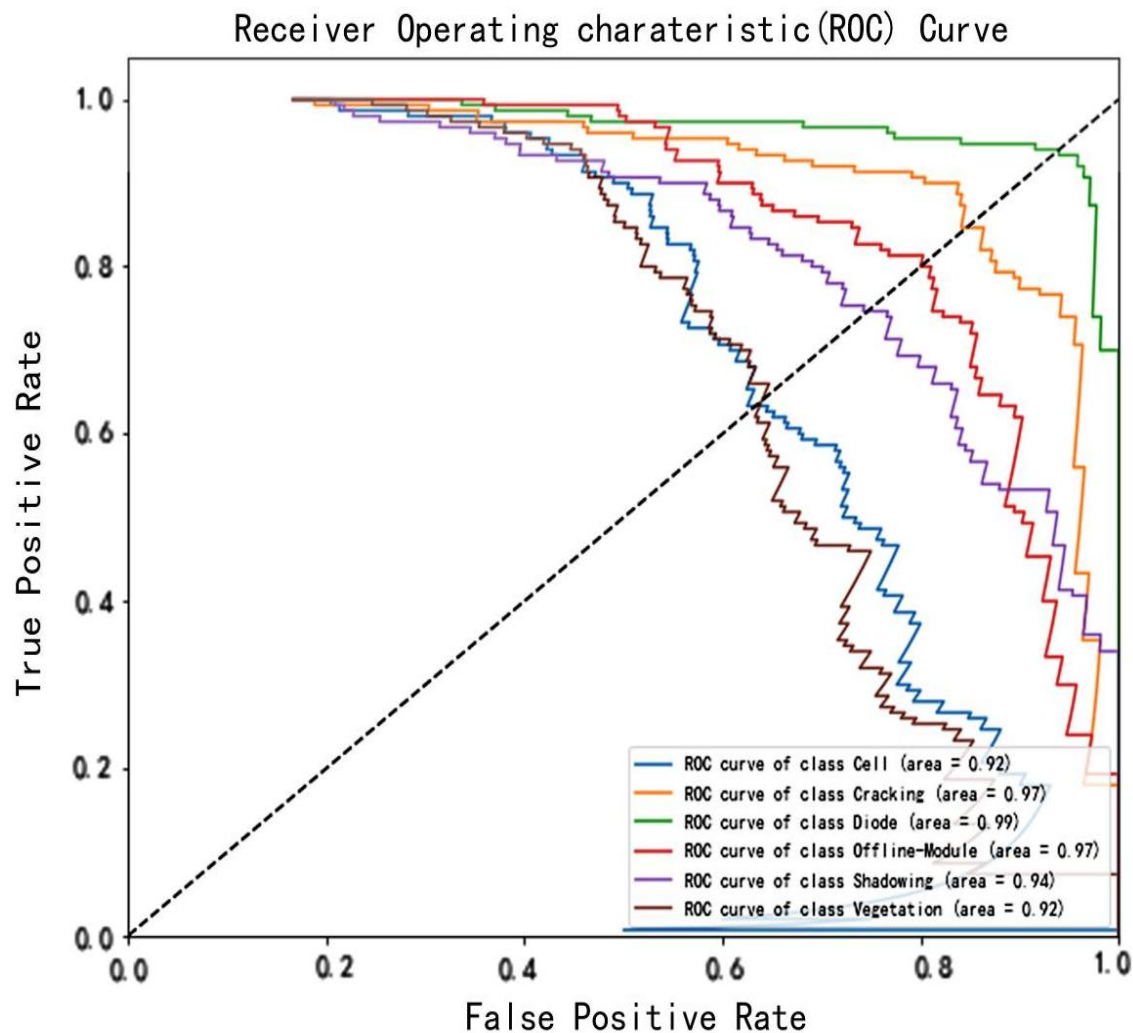


Figure 45. SRNet Model Confusion Matrix for Dataset 1(6-Class)

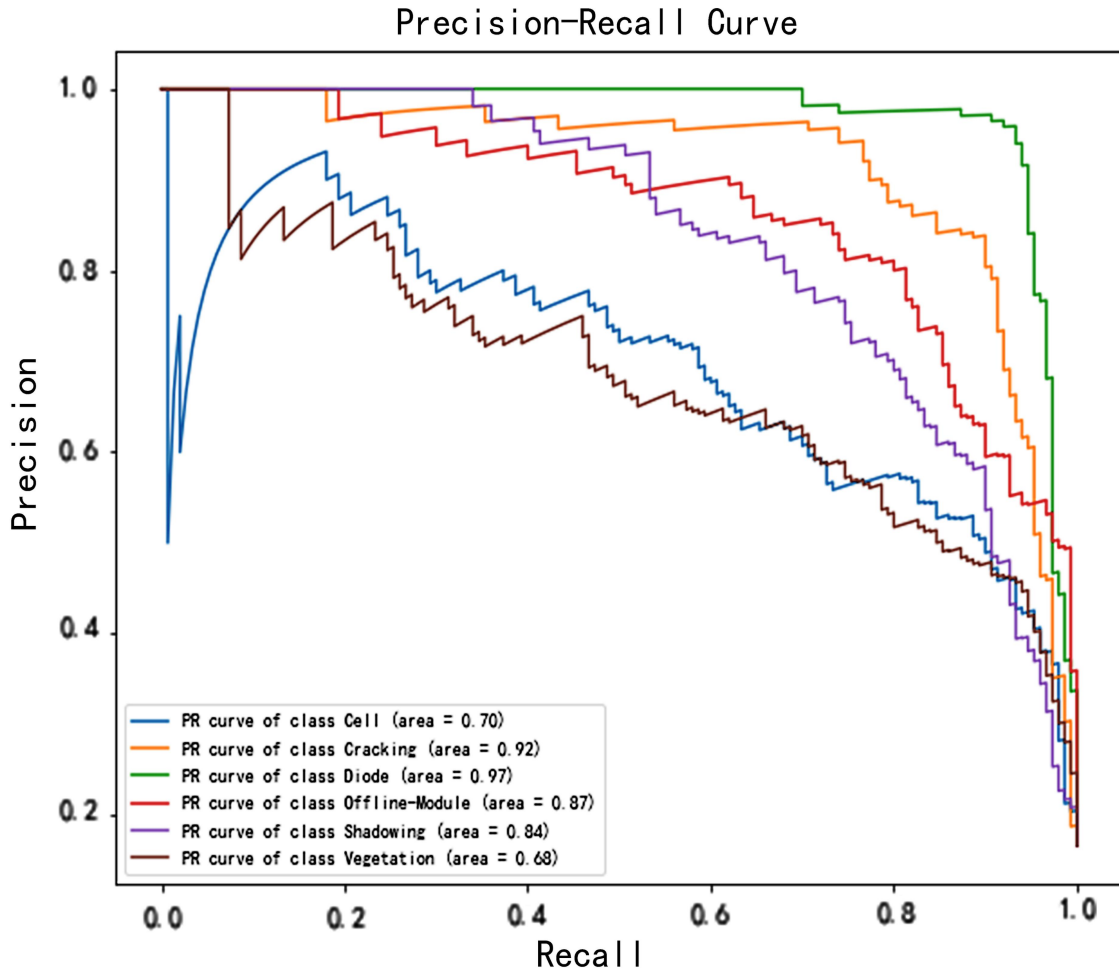
As shown in Figure 46, the ROC curve shows a classification model's performance across six classes. Each class has a line for True Positive Rate vs. False Positive Rate. Diode has the highest AUC of 0.99, with Cracking and Offline-Module at 0.97, Shadowing at 0.94, and Cell and Vegetation at 0.92. These values indicate the model effectively distinguishes classes, especially Diode. The curves stay close to the top-left corner, showing high true positive rates at low false positive rates.



(s) ROC-AUC of 6 Categories

Figure 46. (s) present SRNet model ROC Curve on Dataset 1(6-Class)

As shown in Figure 47, the Precision-Recall curve highlights the model's performance across six classes. Diode achieves the highest area under the curve with a value of 0.97, demonstrating excellent precision and recall. Cracking follows with 0.92, indicating strong performance. Offline-Module and Shadowing score 0.87 and 0.84, respectively, reflecting good balance. In contrast, Cell and Vegetation show lower values of 0.70 and 0.68, suggesting that these classes may require further refinement to improve classification accuracy.

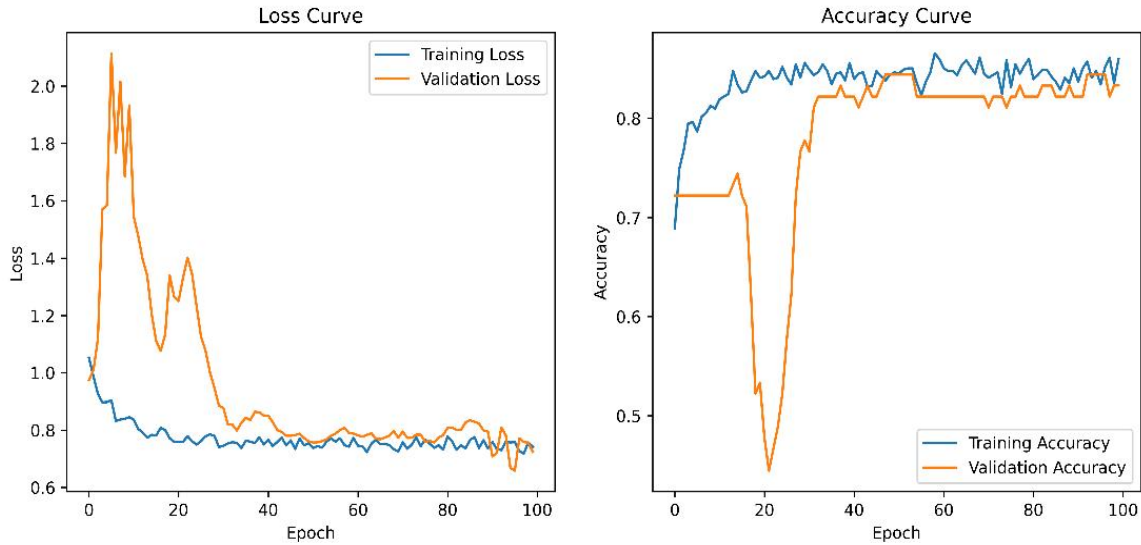


(t) PR-AUC of 6 Categories

Figure 47. (t) present SRNet model ROC and PR Curve on Dataset 1(6-Class)

4.2.3 SRNet on Dataset 2- Binary Class

On Dataset 2, SRNet maintained robust binary classification performance, although with slightly lower metrics compared to Dataset 1. As shown in Figure 48, the model shows strong performance with a training loss of 0.7418 and a validation loss of 0.7447, indicating minimal overfitting. The training accuracy is 86.02%, and the validation accuracy is slightly higher at 87.15%, demonstrating good consistency. From Table 7, on the test set, the model achieves an accuracy of 85.13% and a lower loss of 0.680, confirming its ability to generalize effectively to unseen data.



(u) Train Loss = 0.7418, Val Loss = 0.7447 (v) Train ACC = 0.8602, Val ACC = 0.8715

Figure 48. (u) and (v) present SRNet model's Accuracy and Loss Curve on Dataset 2
(Binary Class)

As shown in Figure 49, the model exhibits strong classification performance, correctly identifying 47 true positives and 18 true negatives. It has a low number of misclassifications, with only 5 false positives and 4 false negatives, indicating that the model effectively distinguishes between the two classes with minimal errors.

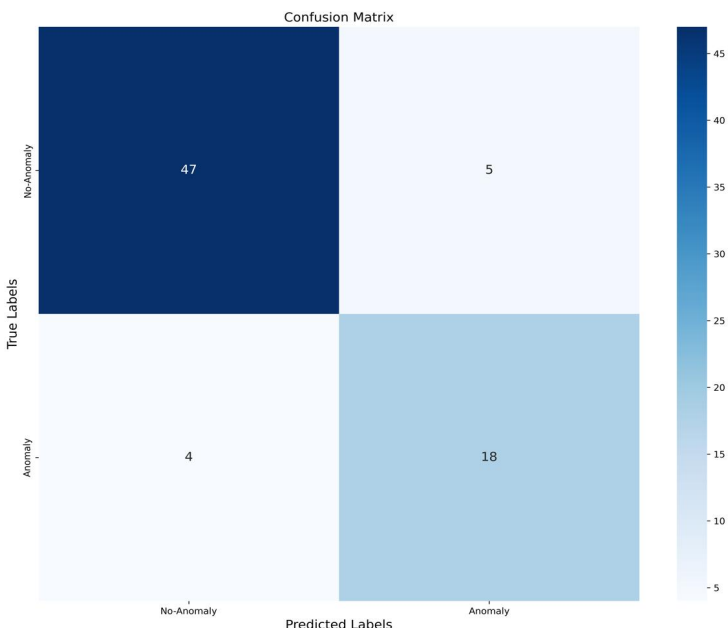
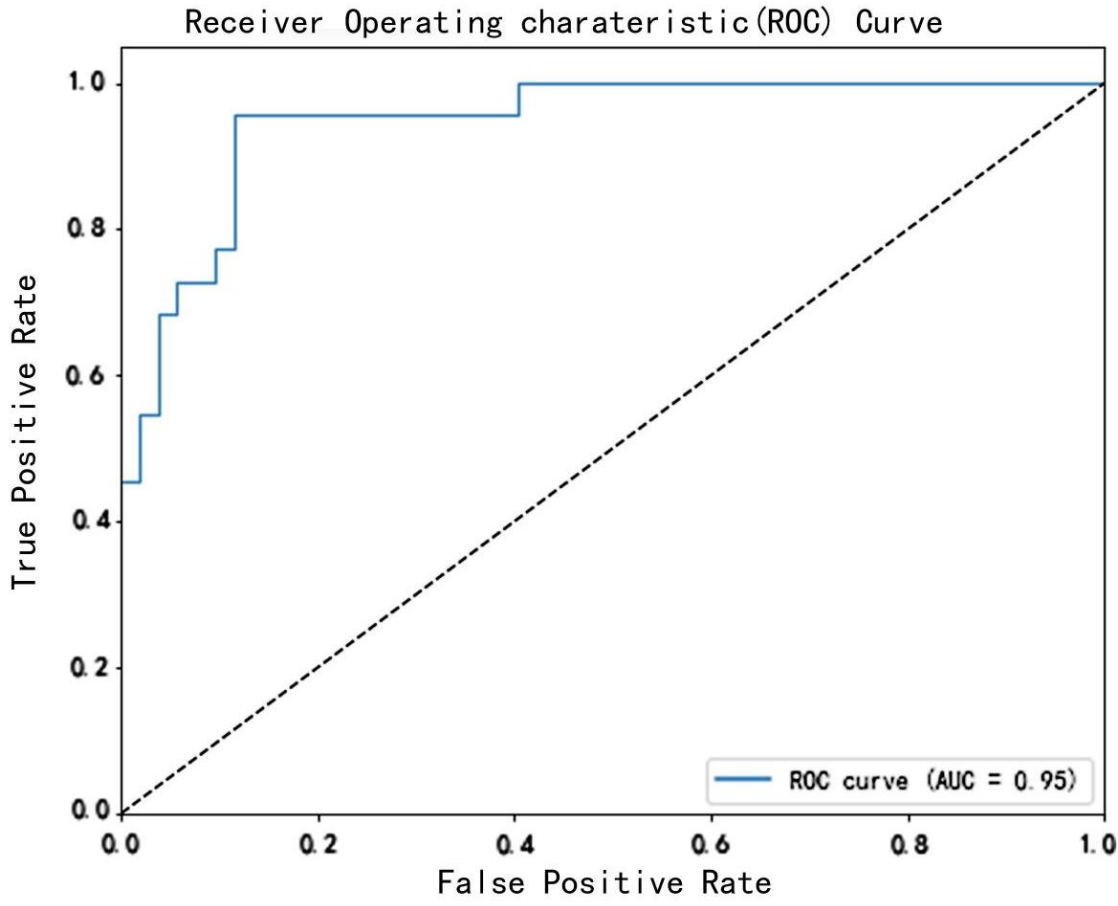


Figure 49. SRNet Model Confusion Matrix for Dataset 2- Binary Class

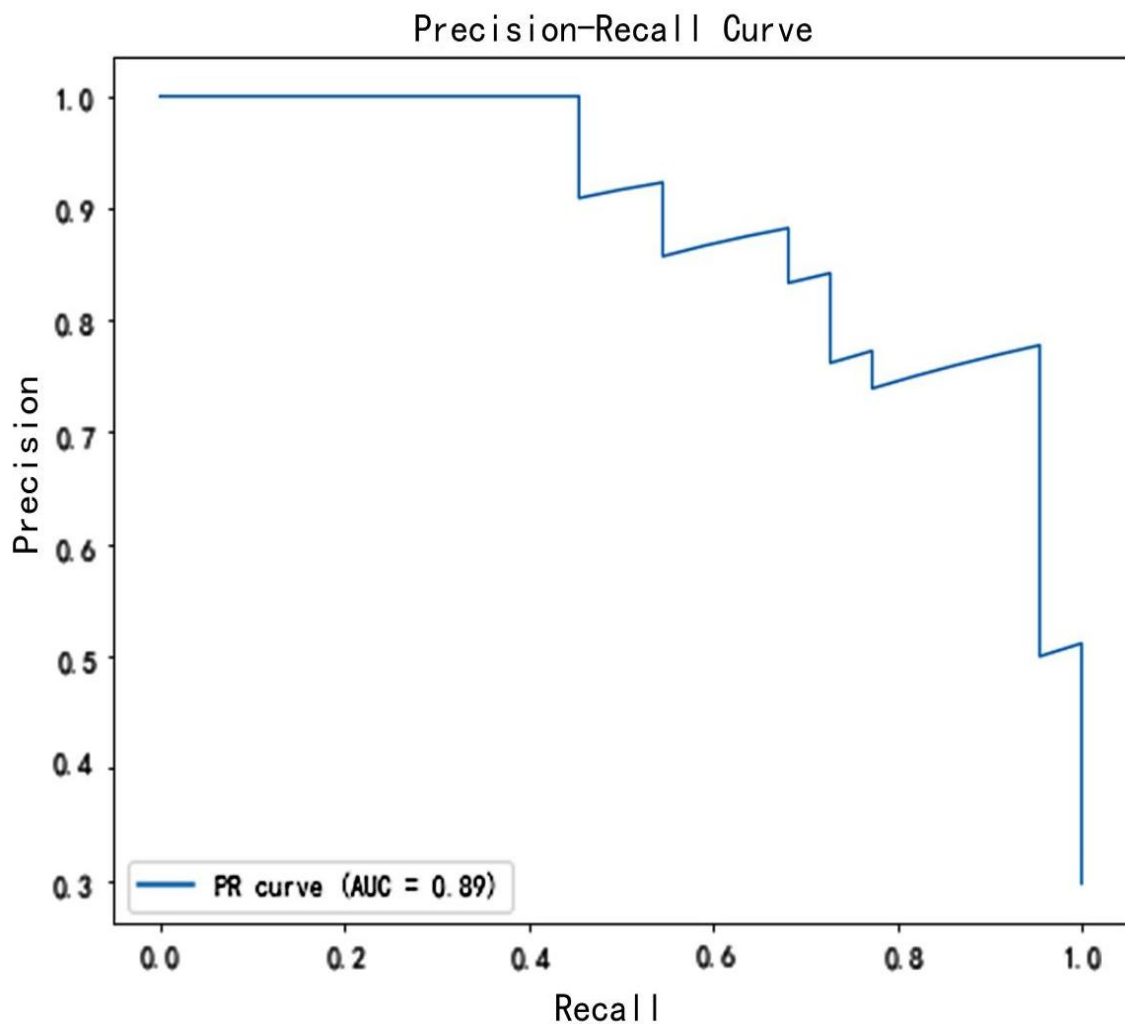
The ROC-AUC score of 0.95, shown in Figure 50, highlights the model's exceptional capability to distinguish between the positive and negative classes. This score reflects a high level of accuracy across various thresholds, suggesting that the model maintains strong performance in identifying true positives while minimizing false positives.



(w) ROC-AUC = 0.95

Figure 50. (w) present SRNet model ROC Curve on Dataset 2(Binary Class)

As shown in Figure 51, the Precision-Recall (PR) curve visually represents a model's performance, plotting precision against recall. The area under this curve is 0.89, indicating strong performance in balancing precision and recall. This AUC value reflects the model's effectiveness in classifying positive instances correctly across various thresholds. Overall, the model demonstrates good precision-recall trade-off, making it reliable for relevant predictive tasks.



(x) PR-AUC = 0.89

Figure 51. (x) present SRNet model PR Curve on Dataset 2(Binary Class)

Detailed results are provided in Table 7 and Table 8.

Table 7. SRNet Model's Performance Metrics-1

Dataset	Class	Loss	Accuracy	Recall	Precision	F1-Score
Dataset1	2-Class	0.3467	0.8807	0.8073	0.9460	0.8712
Dataset 1	6-Class	0.9061	0.7522	0.7522	0.760	0.7523
Dataset 2	2-Class	0.680	0.8513	0.727	0.761	0.744

Table 8. SRNet Model's Performance Metrics-2

Dataset	Class	Specificity	ROC-AUC	PR-AUC
Dataset1	2-Class	0.954	0.9458	0.9522
Dataset 1	6-Class	Cell:0.62 Cracking:0.80 Diode:0.9466 Offline-Module:0.8533 Shadowing:0.653 Vegetation:0.64	Cell:0.92 Cracking:0.97 Diode:0.99 Offline-Module:0.97 Shadowing:0.94 Vegetation:0.92	Cell:0.70 Cracking:0.92 Diode:0.97 Offline-Module:0.87 Shadowing:0.84 Vegetation:0.68
Dataset 2	2-Class	0.9038	0.946	0.890

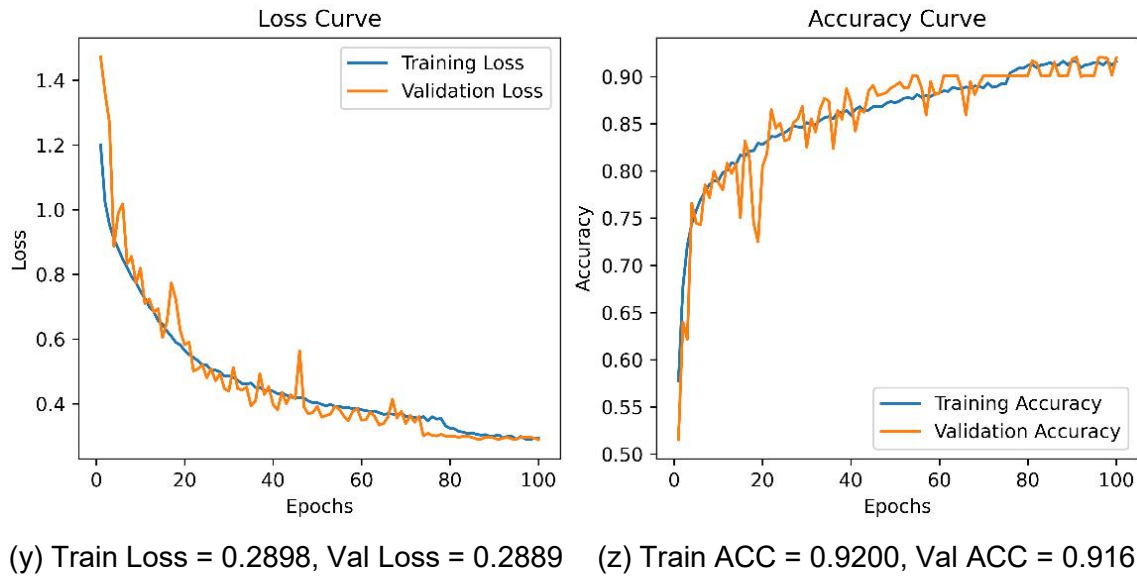
4.3 Experiment 3 - SARNet

The SARNet model is a hybrid architecture that integrates StackNet, improved ResoNet, and an Attention Mechanism to evaluate on two datasets: Dataset 1 (Infrared Solar Module) for both binary and 6-class classification tasks, and Dataset 2 (ELPV) for binary classification. This evaluation aimed not only to assess SARNet's performance across different data distributions and classification complexities, but also to identify the dataset that contributes most effectively to further optimization and deployment.

4.3.1 SARNet on Dataset 1- Binary Class

In the binary classification task on Dataset 1, SARNet exhibited exceptional performance across all key metrics. As shown in Figure 52, the model demonstrates robust performance with a training loss of 0.2898 and validation loss of 0.2889, indicating strong consistency and minimal overfitting. Training accuracy is 0.9200, while validation accuracy is 0.9161, further highlighting reliable generalization. As shown in

Table 9, the test accuracy of 0.917 and test loss of 0.298 confirm that the model maintains its performance on unseen data, ensuring practical effectiveness.



(y) Train Loss = 0.2898, Val Loss = 0.2889 (z) Train ACC = 0.9200, Val ACC = 0.9161

Figure 52. (y) and (z) present SARNet model Accuracy and Loss Curve on Dataset1
(Binary Class)

As shown in Figure 53, The model demonstrates strong overall performance, with 1,393 true positives and 1,294 true negatives, indicating a high level of accuracy in distinguishing both classes. The low false positive count of 107 and relatively few false negatives at 206 suggest that the model maintains a good balance between sensitivity and specificity, effectively identifying positive cases while minimizing misclassifications.

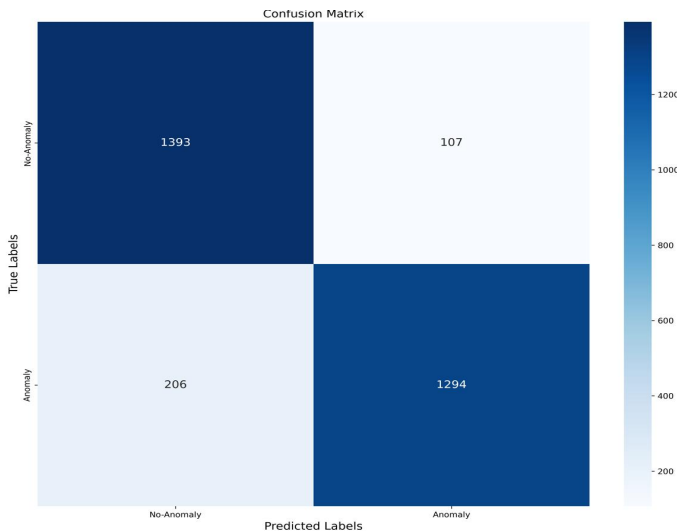
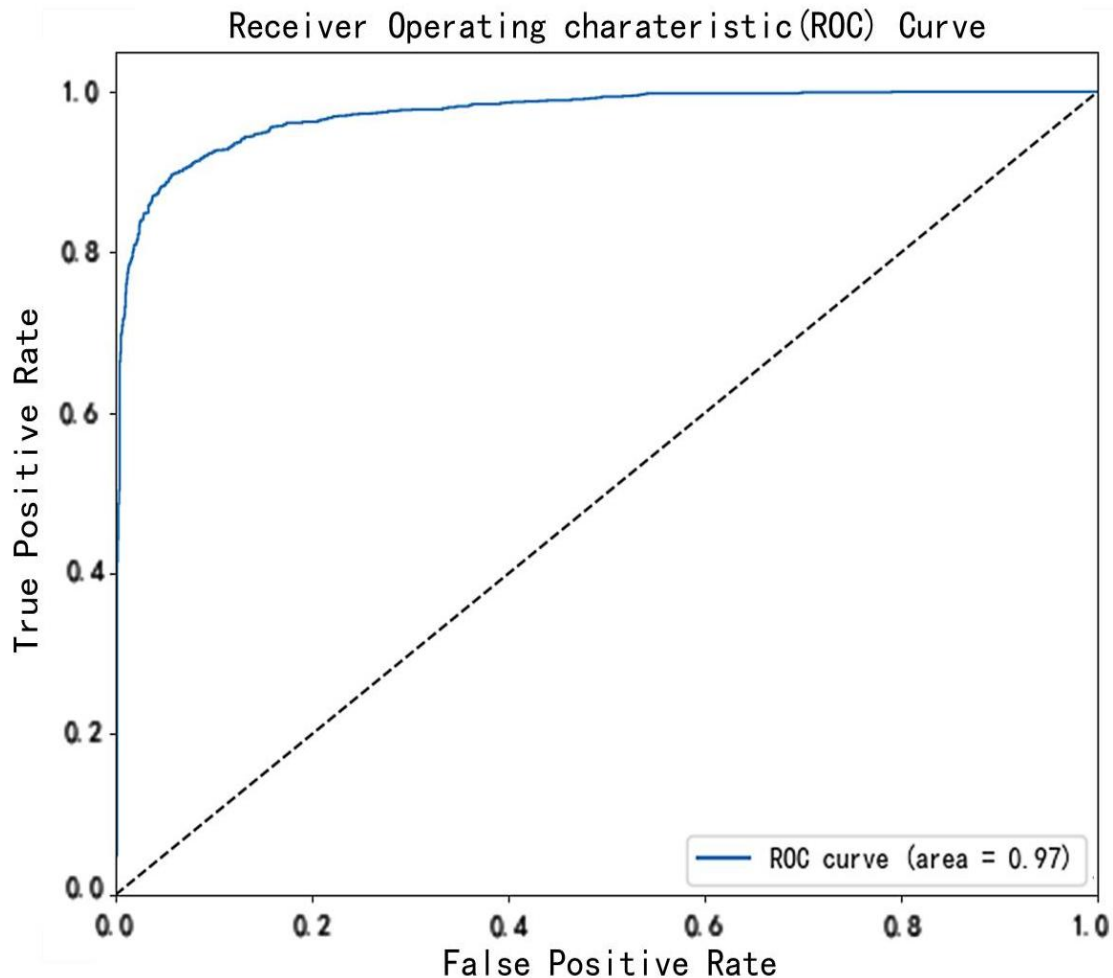


Figure 53. SARNet model Confusion Matrix for Dataset 1- Binary Class

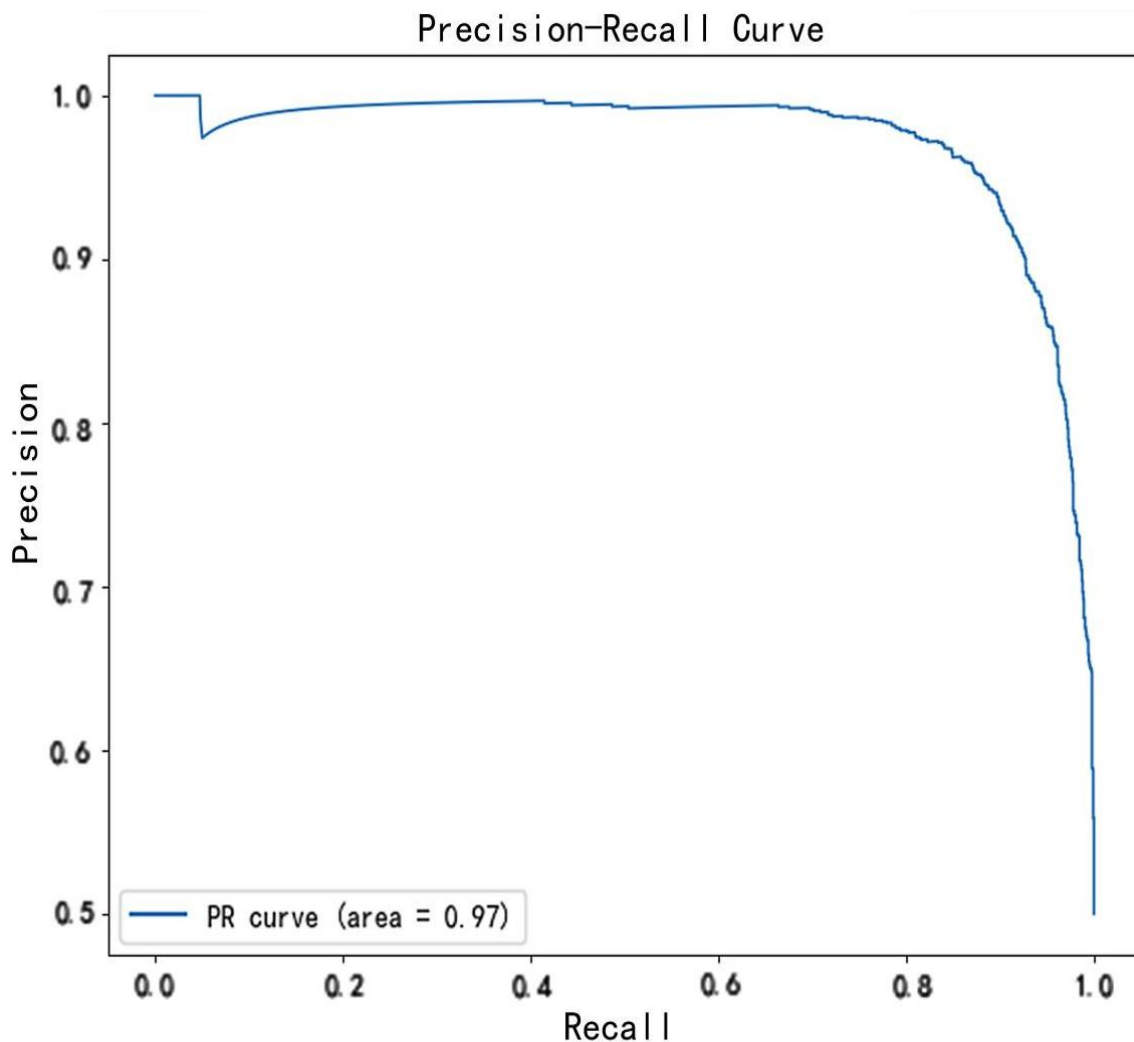
As shown in Figure 54, the ROC curve shows excellent model performance with an AUC of 0.97. The curve rises sharply near the top-left corner, indicating a high True Positive Rate and low False Positive Rate, which demonstrates the model's strong discrimination ability.



(aa) ROC-AUC = 0.97

Figure 54. (aa) present SARNet model ROC Curve on Dataset 1- Binary Class

As shown in Figure 55, the PR-AUC value of 0.97 indicates excellent precision-recall performance. This high score reflects the model's strong ability to maintain both high precision and high recall across different thresholds, suggesting it can accurately identify positive cases while minimizing false positives and false negatives.

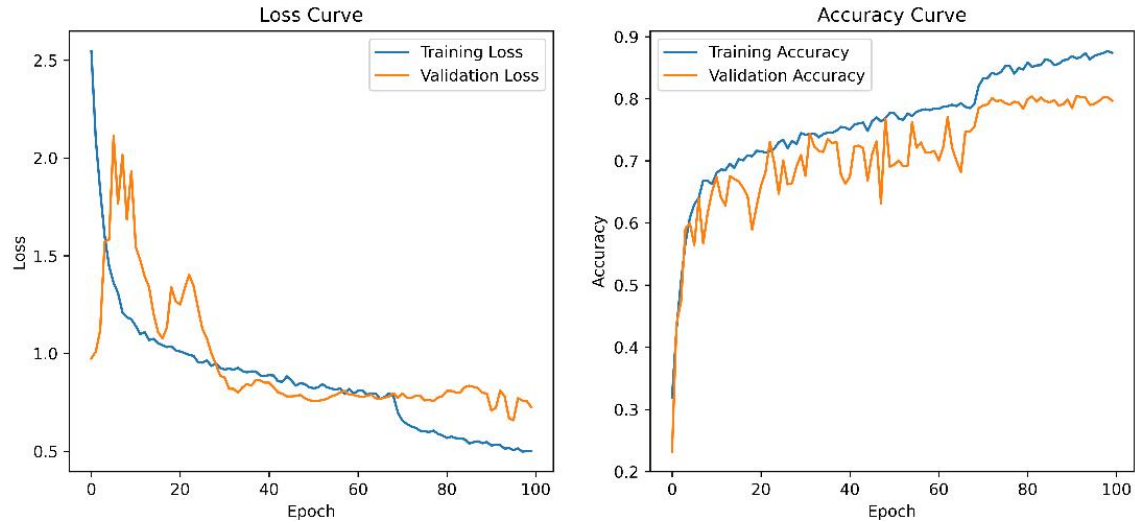


(ab) PR-AUC = 0.97

Figure 55. (bb) present SARNet model PR Curve on Dataset 1- Binary Class

4.3.2 SARNet on Dataset 1- 6-Class

In the 6-class classification task on Dataset 1, SARNet also delivered strong overall performance. As shown in Figure 56, the model achieves solid performance, with training accuracy at 87.39% and validation accuracy at 79.63%, indicating effective learning with some generalization gap. The training and validation losses, at 0.5005 and 0.5804 respectively, remain relatively close. In Table 9, on the test set, the accuracy reaches 81.63% with a loss of 0.6877, confirming that the model maintains stable performance on unseen data.



(ac) Train Loss = 0.5005, Val Loss = 0.5804 (ad) Train ACC = 0.8739, Val ACC = 0.7963

Figure 56. (cc) and (dd) present SARNet model Accuracy and Loss Curve on Dataset 1(6-Class)

The confusion matrix shown in Figure 57 evaluates the model's performance across six fault classes, each corresponding to specific issues in solar panels. The model performs best on Diode faults with 219 true positives and low misclassification. Cracking also shows high accuracy with 109 true positives and only 10 false positives. Cell and Offline-Module classes have moderate confusion, with 74 and 32 false negatives respectively. Shadowing and Vegetation show higher false positive rates, especially Vegetation, which has 102 misclassified cases, indicating room for improvement.

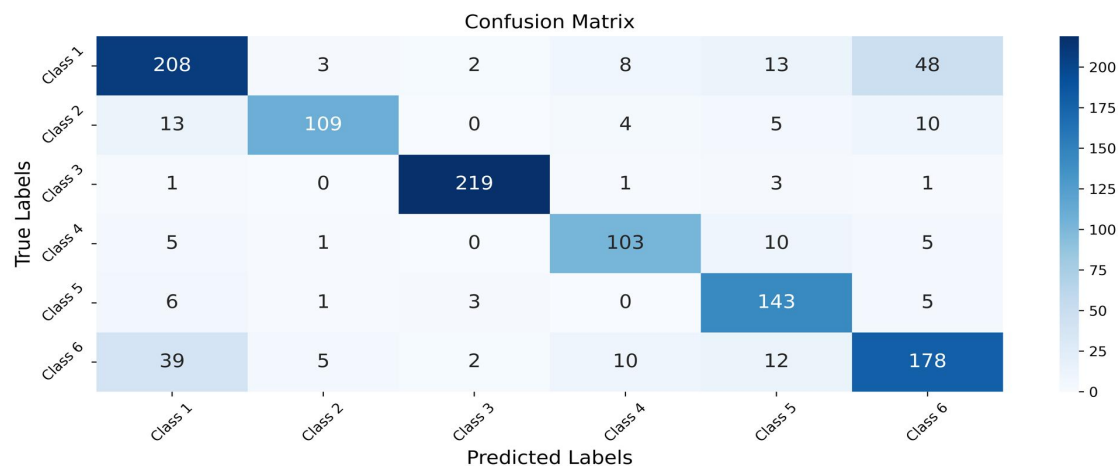
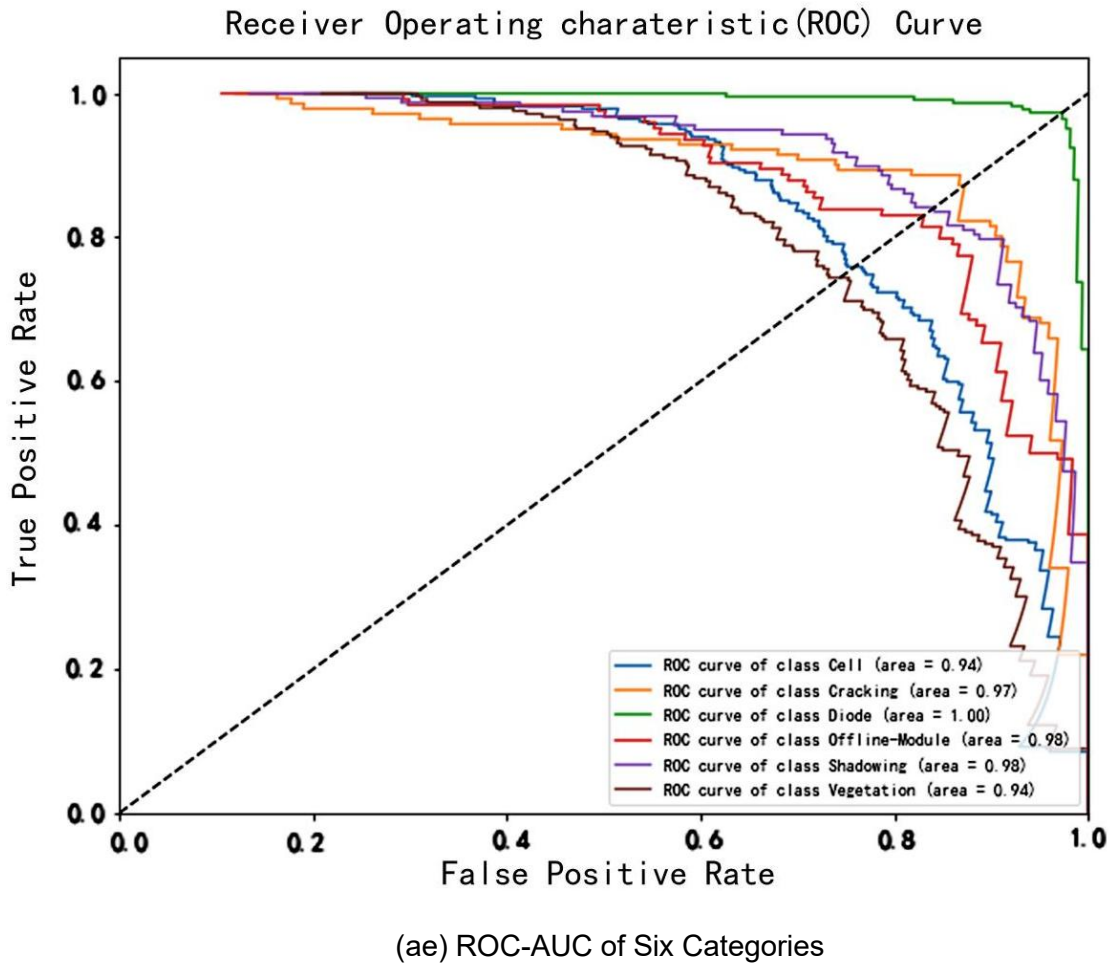


Figure 57. SARNet model Confusion Matrix for Dataset 1(6-Class)

As shown in Figure 58, the ROC curve shows the performance of a classification model across six classes. Each class has a line showing the True Positive Rate against the False Positive Rate. Diode has a perfect AUC of 1.00, Cracking is 0.97, Shadowing and Offline-Module both have 0.98, and Cell and Vegetation each have 0.94. These high AUC values indicate the model has excellent discriminatory power, effectively distinguishing between classes with minimal false positives. The curves generally hug the top-left corner, reflecting high true positive rates at low false positive rates.



(ae) ROC-AUC of Six Categories

Figure 58. (ee) present SARNet model ROC Curve on Dataset 1(6-Class)

In Figure 59, the Precision-Recall (PR) curve shows the model's performance across six classes. Class Diode has a perfect AUC of 1.00, Cracking is 0.97, Shadowing and Offline-Module both have 0.98, and Cell and Vegetation each have 0.94. These high AUC values indicate the model effectively balances precision and recall, making it reliable for classification. The curves also show high precision across varying recall

levels, reflecting strong performance in identifying relevant instances with minimal false positives.

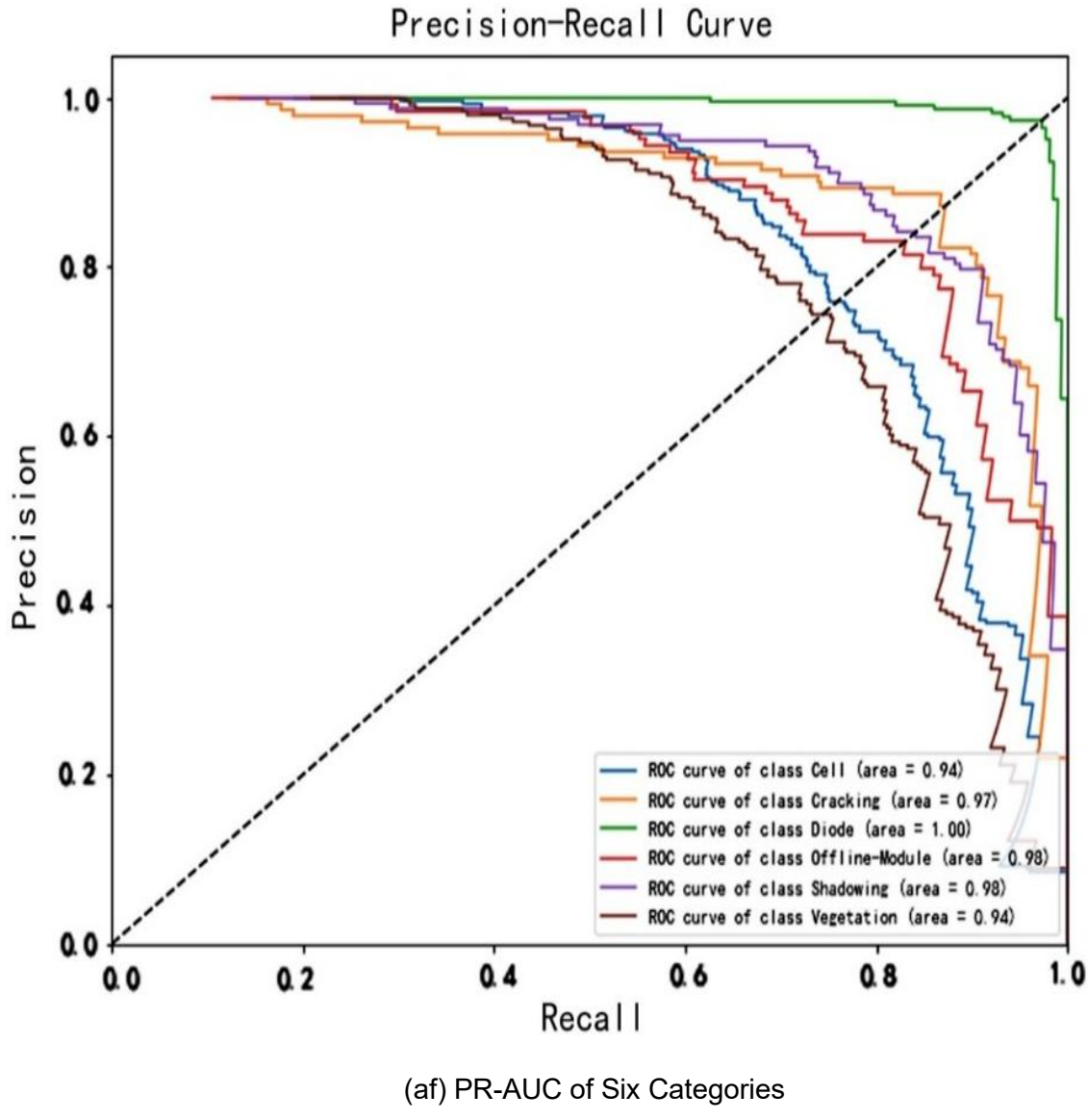
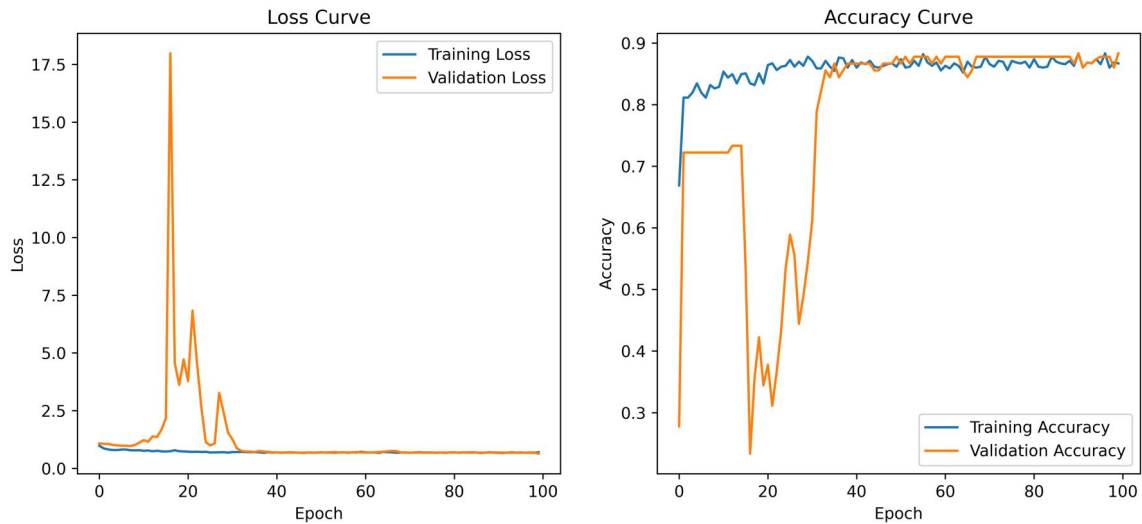


Figure 59. (ff) present SARNet model PR Curve on Dataset 1(6-Class)

4.3.3 SARNet on Dataset 2- Binary Class

On Dataset 2, SARNet achieved slightly lower yet still competitive binary classification results. As shown in Figure 60, The model shows good generalization with similar training and validation losses and no significant overfitting. Training accuracy is 88.57%, validation accuracy 89.78%, indicating effective learning. Test accuracy of 89.1% and test loss of 0.656 confirm strong performance on unseen data, though the loss is slightly

higher than in training and validation.



(ag) Train Loss = 0.3899 Val Loss = 0.3900 (ah) Train ACC = 0.8857, Val ACC = 0.8978

Figure 60. (gg) and (hh) present SARNet model Accuracy and Loss Curve on Dataset 2
(Binary Class)

As shown in Figure 61, the model correctly identified 48 positive cases with only 4 false positives, reflecting high precision. It also achieved 18 true negatives and 4 false negatives, indicating balanced sensitivity and specificity. Overall, the results suggest reliable performance in distinguishing between the two classes.

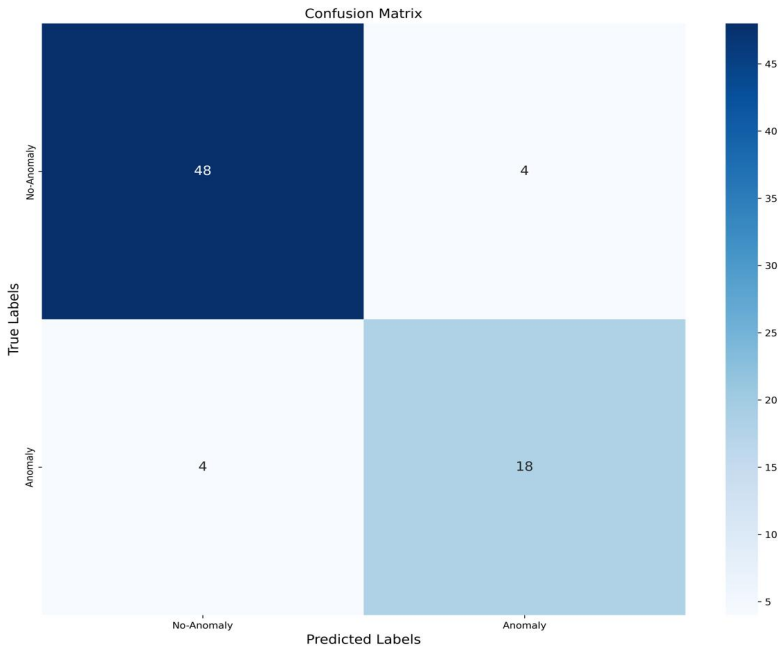
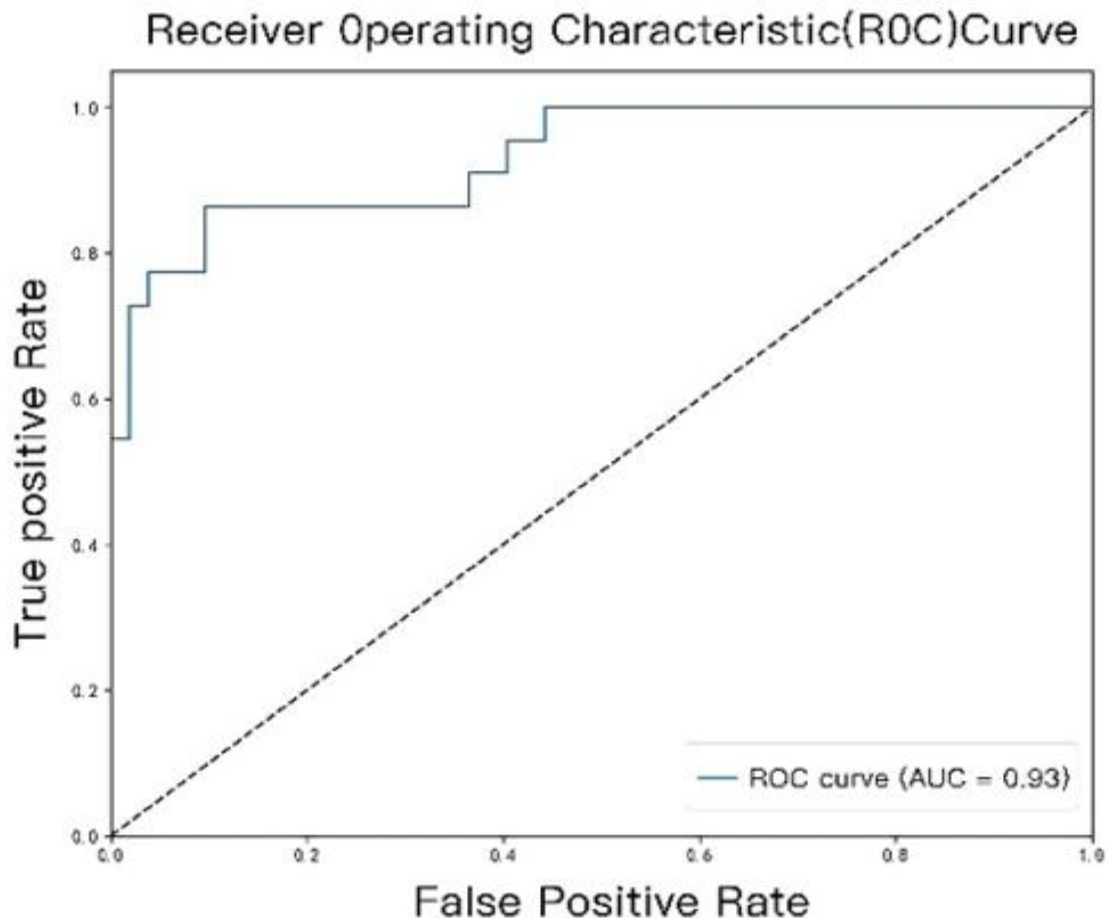


Figure 61. SARNet model Confusion Matrix for Dataset 2-Binary Class

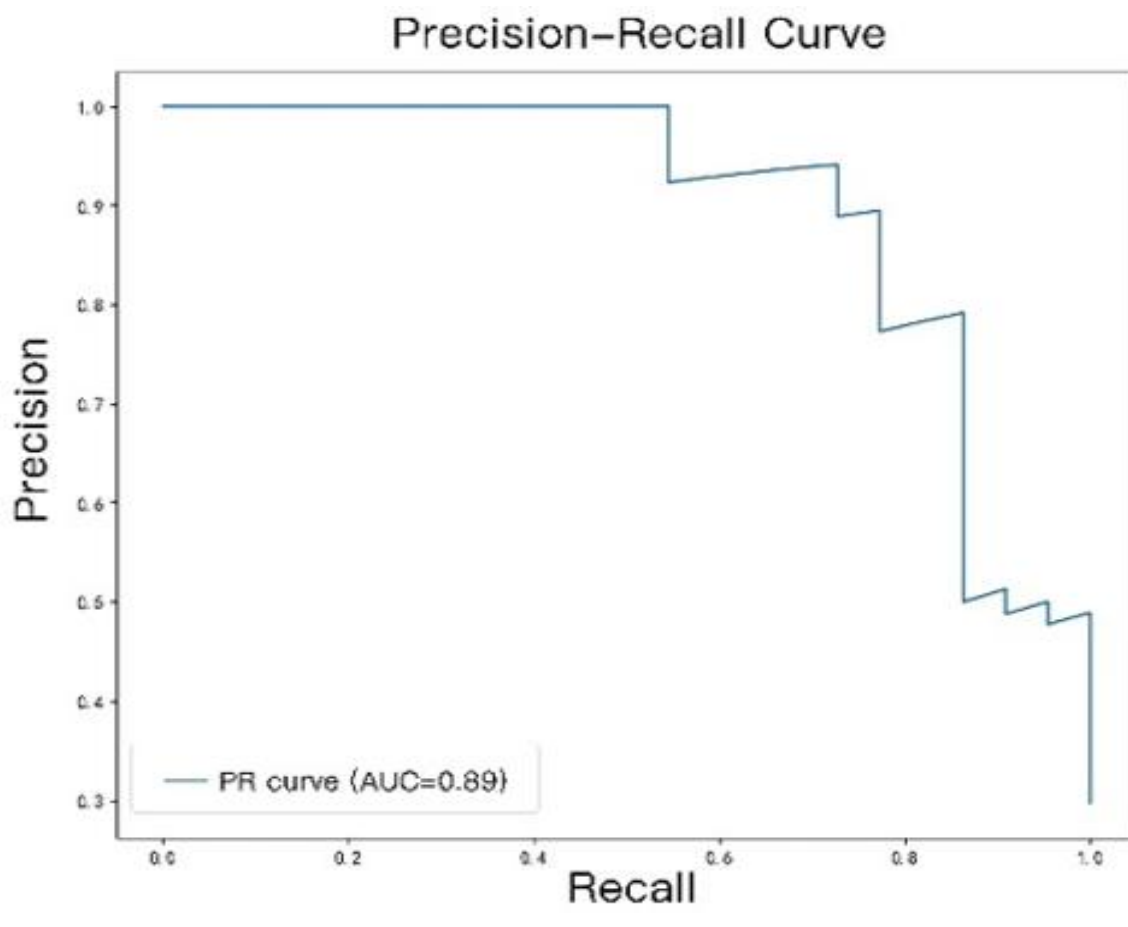
As shown in Figure 62, the ROC curve illustrates the model's performance in classification tasks. The solid line represents the ROC curve, plotting the True Positive Rate against the False Positive Rate. The area under the ROC curve is 0.93, suggesting strong performance in distinguishing between classes. This demonstrates the model's effectiveness in achieving good classification performance.



(ii) ROC-AUC = 0.93

Figure 62.(ii) present SARNet model ROC Curve on Dataset 2- Binary Class

The Precision-Recall (PR) curve in Figure 63, showing how precision changes with recall at different classification thresholds. The area under the curve is 0.89, indicating good performance in balancing precision and recall. The curve starts near a precision of 1.0 and gradually declines as recall increases, reflecting a typical trade-off where higher recall often leads to lower precision. This suggests the model effectively prioritizes precise predictions at lower recall levels.



(aj) PR-AUC = 0.89

Figure 63. (jj) present SARNet model PR Curve on Dataset 2- Binary Class

The full results and training details are presented in Table 9 and Table 10.

Table 9. SARNet Model's Performance Metrics-1

Dataset	Class	Loss	Accuracy	Recall	Precision	F1-Score
Dataset1	2-Class	0.298	0.917	0.888	0.942	0.914
Dataset 1	6-Class	0.6877	0.8163	0.8222	0.816	0.816
Dataset 2	2-Class	0.656	0.891	0.8580	0.8480	0.8720

Table 10. SARNet Model's Performance Metrics-2

Dataset	Class	Specificity	ROC-AUC	PR-AUC
Dataset1	2-Class	0.946	0.972	0.973
Dataset 1	6-Class	Cell:0.76 Cracking:0.92 Diode:0.97 Offline-Module:0.82 Shadowing:0.77 Vegetation:0.72	Cell:0.94 Cracking:0.97 Diode:1.0 Offline-Module:0.98 Shadowing:0.98 Vegetation:0.94	Cell:0.85 Cracking:0.91 Diode:0.99 Offline-Module:0.89 Shadowing:0.92 Vegetation:0.81
Dataset 2	2-Class	0.923	0.947	0.904

4.4 Current Experiments Results Summary

In this project, I sequentially compare three distinct model architectures: the StackNet, the SRNet combining StackNet with ResoNet, and the hybrid SARNet. Each architecture demonstrates varying levels of performance across datasets and classification tasks, emphasizing the critical influence of architectural design in solar panel fault classification.

The baseline StackNet serves as a reliable benchmark in the binary classification task on Dataset 1, achieving a loss of 0.3671 and an accuracy of 88.27%. However, StackNet struggles in the complex six-class classification, with PR-AUC scores dropping to 0.59 for Cracking and 0.62 for Vegetation. This indicates its limited ability to extract fine-grained features and handle faults with high spatial overlap or subtle visual signs, revealing its constraints in multi-class situations.

To overcome these limitations, SRNet adds ResoNet modules to StackNet to capture multi-scale features, enhancing fault pattern recognition. In Dataset 1's six-class task, SRNet outperforms StackNet in Offline-Module and Diode with ROC-AUC scores of 0.97 and 0.99, up from StackNet's 0.94 and 0.95. But in Dataset 2's binary task, SRNet's accuracy is 85.13% versus StackNet's 87.8%. While ResoNet improves spatial

sensitivity, its lack of dynamic focus adjustment weakens performance in binary tasks needing precise anomaly detection.

To address this bottleneck, the final architecture-SARNet. SARNet combines an Attention Mechanism with SRNet to focus on key image regions, boosting performance in complex classification. On Dataset 1, it gets an F1-score of 0.91 in Cracking, versus StackNet's 0.87, and an overall F1-score of 0.816 compared to StackNet's 0.695. In Dataset 2's binary task, SARNet achieves 89.1% accuracy. These improvements validate the role of attention in complementing multi-scale feature extraction, particularly in identifying subtle or overlapping faults.

Overall, the comparative experiments highlight the effectiveness of the proposed SARNet architecture. The integration of StackNet, ResoNet, and Attention modules significantly enhances both classification accuracy and robustness, especially under complex and diverse imaging conditions.

The results of each experiment are summarized in Table 11 and Table 12.

Table 11. Compare models' Performance Metrics-1

Model	Dataset	Class	Loss	Accuracy	Recall	Precision	F1-Score
StackNet Model	Dataset 1	2-class	0.3671	0.8827	0.8326	0.9251	0.8764
	Dataset 1	6-class	1.0872	0.6922	0.6922	0.702	0.695
	Dataset 2	2-class	0.571	0.878	0.818	0.783	0.800
SRNet Model	Dataset1	2-Class	0.3467	0.8807	0.8073	0.9460	0.8712
	Dataset 1	6-Class	0.9061	0.7522	0.7522	0.760	0.7523
	Dataset 2	2-	0.680	0.8513	0.727	0.761	0.744

		Class					
SARNet Model	Dataset1	2-Class	0.298	0.917	0.888	0.942	0.914
	Dataset 1	6-Class	0.6877	0.8163	0.8222	0.816	0.816
	Dataset 2	2-Class	0.656	0.891	0.858	0.848	0.872

Table 12. Compare models' Performance Metrics-2

Model	Dataset	Class	Specificity	ROC-AUC	PR-AUC
StackNet Model	Dataset 1	2-Class	0.9326	0.9516	0.955
	Dataset 1	6-Class	Cell:0.706 Cracking:0.506 Diode:0.76 Offline-Module:0.7066 Shadowing:0.90 Vegetation:0.673	Cell:0.90 Cracking:0.86 Diode:0.95 Offline-Module:0.94 Shadowing:0.99 Vegetation:0.90	Cell:0.78 Cracking:0.59 Diode:0.88 Offline-Module:0.80 Shadowing:0.96 Vegetation:0.62
	Dataset 2	2-Class	0.9038	0.912	0.832
SRNet	Dataset1	2-Class	0.954	0.9458	0.9522

Model	Dataset 1	6-Class	Cell:0.62 Cracking:0.80 Diode:0.946 Offline-Module:0.8533 Shadowing:0.653 Vegetation:0.64	Cell:0.92 Cracking:0.97 Diode:0.99 Offline-Module:0.97 Shadowing:0.94 Vegetation:0.92	Cell:0.70 Cracking:0.92 Diode:0.97 Offline-Module:0.87 Shadowing:0.84 Vegetation:0.68
	Dataset 2	2-Class	0.9038	0.946	0.890
SARNet Model	Dataset1	2-Class	0.946	0.972	0.973
	Dataset 1	6-Class	Cell:0.76 Cracking:0.92 Diode:0.97 Offline-Module:0.82 Shadowing:0.77 Vegetation:0.72	Cell:0.94 Cracking:0.97 Diode:1.0 Offline-Module:0.98 Shadowing:0.98 Vegetation:0.94	Cell:0.85 Cracking:0.91 Diode:0.99 Offline-Module:0.89 Shadowing:0.92 Vegetation:0.81
	Dataset	2-Class	0.923	0.947	0.904

	2				
--	---	--	--	--	--

4.5 Model Explainability

To enhance the interpretability of deep learning models in fault detection tasks, this project incorporates the Grad-CAM (Gradient-weighted Class Activation Mapping) algorithm as a post hoc visualization tool. Grad-CAM computes the gradients of the target class prediction with respect to the feature maps of a convolutional layer to produce a heatmap that highlights the regions the model focuses on when making a decision [32]. This method is model-agnostic and widely applicable, especially for CNNs.

The Grad-CAM visualization tool developed in this work involves the following key steps:

1. Convolutional Layer Selection: Automatically locates the last convolutional layer in the model to extract semantically rich spatial feature maps.
2. Forward Pass and Gradient Recording: Creates a model from input to the convolutional layer and final prediction, using `tf.GradientTape` to record gradients of the target class relative to the feature maps.
3. Heatmap Generation: Applies channel-wise global average pooling to the gradients, generating a weighted activation map which is then normalized.
4. Image Overlay and Display: Combines the heatmap with the original image for intuitive interpretation.
5. Batch Processing: Selects representative samples for each class from the test set and generates Grad-CAM visualizations in batches, enabling inter-class comparison and fault analysis.

In this study, Grad-CAM was applied to visualize and interpret three specific classification tasks derived from two datasets:

- Binary Classification on Dataset 1 (Infrared Images):

The model distinguishes between normal and abnormal solar modules. Grad-CAM visualizations like Figure 64 and Figure 65 reveal that when an image is classified as anomaly, the attention maps typically highlight critical fault regions such as cracks, hotspots, or dirt accumulation, indicating that the model is focusing on meaningful defect areas within the infrared spectrum.

Anomaly Sample 1 – Original Image Anomaly Sample 1 – Grad-CAM Heatmap

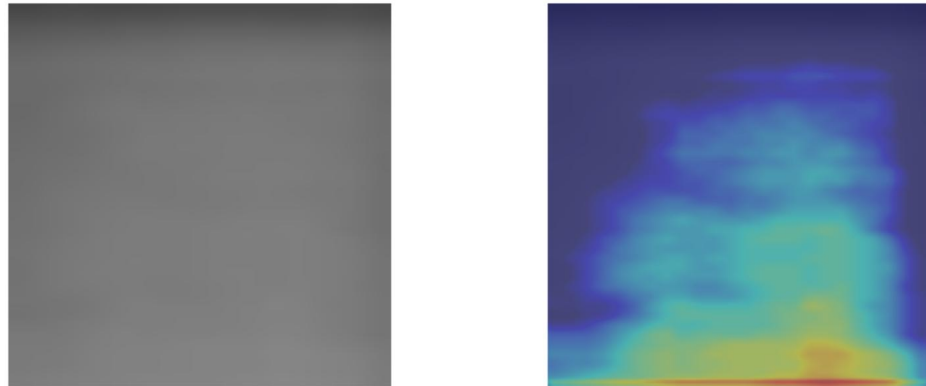


Figure 64. Grad-CAM Visualization of Dataset 1 Binary class (Anomaly)

NO-Anomaly Sample – Original Image NO-Anomaly Sample 1–Grad-CAM Heatmap



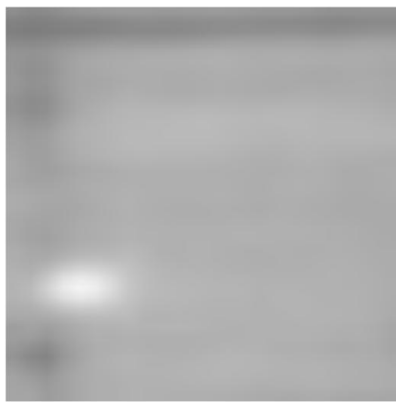
Figure 65. Grad-CAM Visualization of Dataset 1 Binary class (No-Anomaly)

- Six-Class Classification on Dataset 1 (Infrared Images):

The model categorizes faults into six types: Vegetation, Shadowing, Cell damage, Diode faults, Cracking, and Offline-Module. Heatmaps show the model can target regions for each fault type, such as plant-covered areas for Vegetation or structural breaks for Cracking, proving its ability to distinguish multiple fault types in thermal images.

Grad-CAM Visualization of six-class shows from Figure 66 to Figure 71:

Cell Sample 1-Original Image



Cell Sample 1- Grad-CAM Heatmap

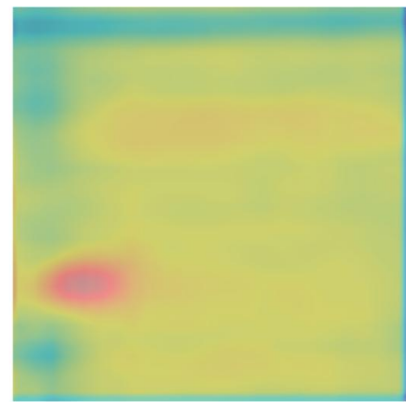


Figure 66. Grad-CAM Visualization of Cell

Cracking Sample 1-Original Image



Cracking Sample 1- Grad-CAM Heatmap

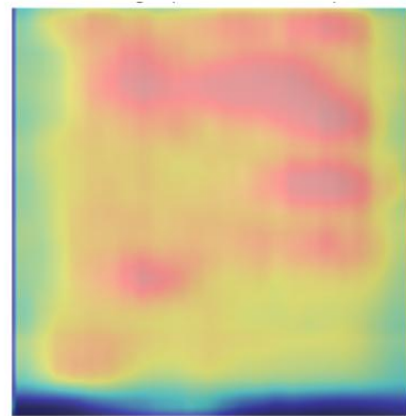
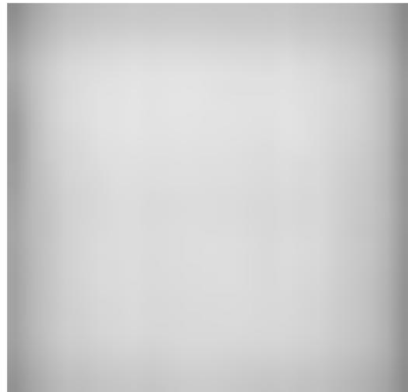


Figure 67. Grad-CAM Visualization of Cracking

Diode Sample 1-Original Image



Diode Sample 1- Grad-CAM Heatmap

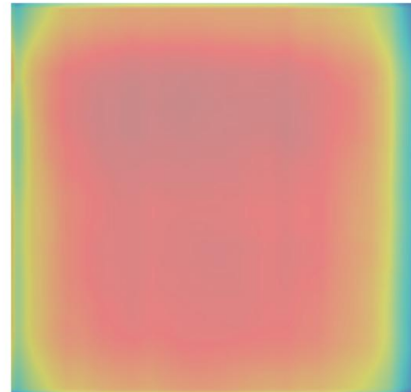


Figure 68. Grad-CAM Visualization of Diode

Offline-Module Sample 1-Original Image Offline-Module Sample 1- Grad-CAM Heatmap

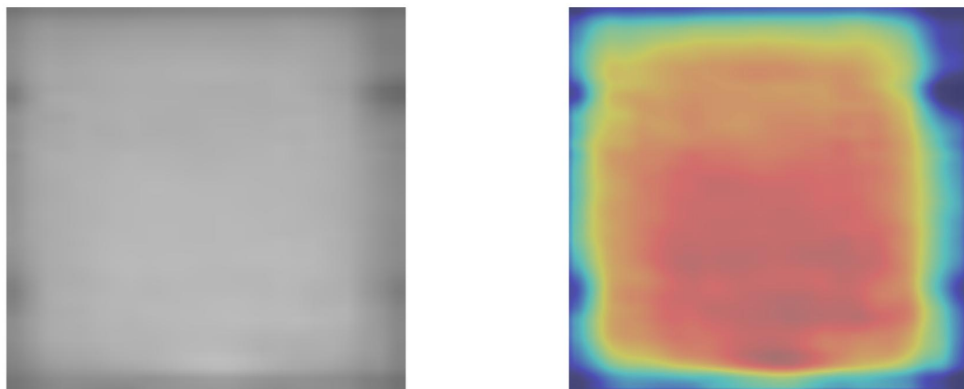


Figure 69. Grad-CAM Visualization of Offline-Module

Shadowing Sample 1-Original Image Shadowing Sample 1-Grad-CAM Heatmap

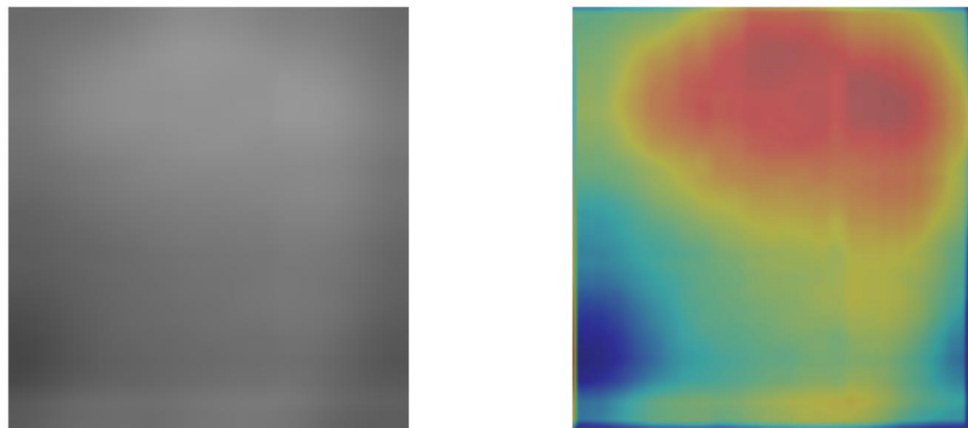


Figure 70. Grad-CAM Visualization of Shadowing

Vegetation Sample 1-Original Image Vegetation Sample 1-Grad-CAM Heatmap

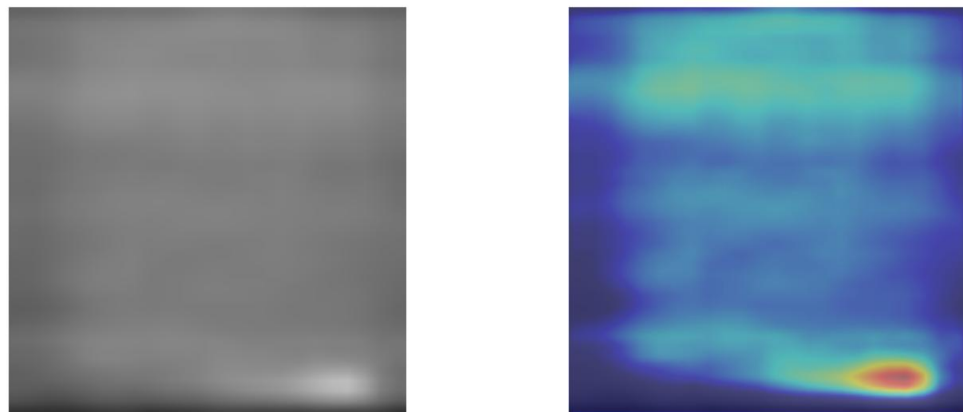


Figure 71. Grad-CAM Visualization of Vegetation

- Binary Classification on Dataset 2 (Electroluminescence (EL) Images):
This task involves detecting whether a solar panel is defected or non-defected. Grad-CAM results like Figure 72 show clear attention on visual anomalies such as surface contamination, shading, or physical damages in the visible spectrum, supporting the model's decision-making process in classifying defective modules.

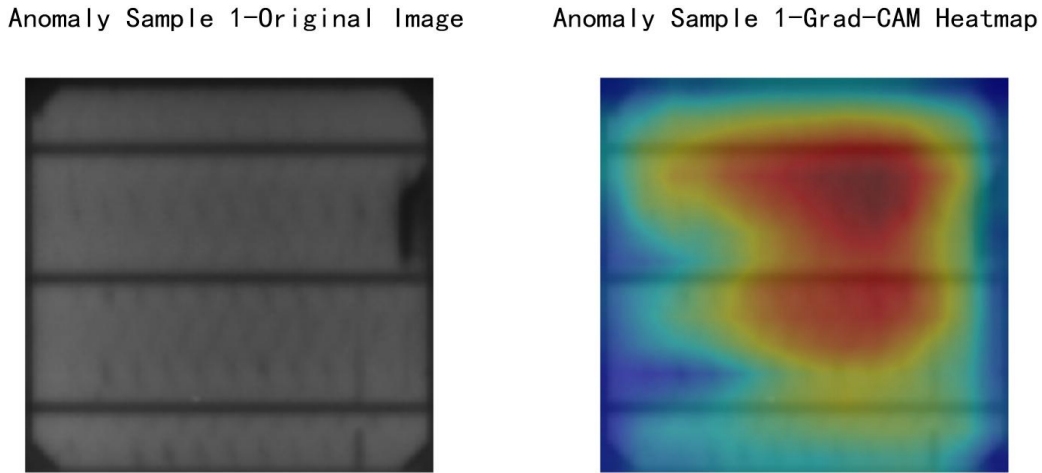


Figure 72. Grad-CAM Visualization of Dataset 2 Binary class (Anomaly)

Across all tasks, Grad-CAM visualizations provide valuable insights into the model's reasoning, helping to verify whether the network is attending to semantically relevant fault areas. This not only enhances interpretability but also supports greater trust in model predictions when deployed in real-world solar panel inspection systems.

4.6 Model Visualization - GUI Design

In order to improve the usability and interactivity of deep learning models in actual solar panel fault detection scenarios, this project built a web-based graphical user interface (GUI) to visualize the detection results and support users to upload images for automatic recognition.

As shown in Figure 73 and Figure 74, the homepage has a simple navigation bar with 'Home' and 'Model Prediction' options for easy switching. Users can scroll to view the website overview, application scenarios, usage steps, and project details, enabling quick understanding and efficient operation.

Solar Panel Anomaly Detection

1. Instruction of the website:

Introduction:

This website provides a visual and interactive platform for identifying faults in solar panels using deep learning-based image classification models. You can upload infrared or electroluminescence (EL) images of solar modules, and the system will automatically classify any potential anomalies.

When to Use:

This tool is especially useful for:

- Solar panel manufacturers inspecting quality during production.
- Field technicians or maintenance teams diagnosing faulty panels on-site.
- Researchers working on photovoltaic system health monitoring.
- Anyone using drones or monitoring systems that capture IR or EL images of panels.

Navigation

Go to

- Home
- Model Prediction

Model Information

- Dataset1-2: Binary Classification (IR)
- Dataset1-6: Six-class Classification (IR)
- Dataset2-2: Binary Classification (EL)

Classes

Binary Classes:

- No-Anomaly
- Anomaly

Six Classes:

Figure 73. Instruction of the website part of Home page

2. About the Project

Project Overview

Solar Panel Anomaly Classification: This project aims to improve solar panel inspection by using deep learning to classify faults from image data. By detecting defects early, it helps extend the lifespan and efficiency of solar panels and reduces maintenance costs.

The model supports two types of image input: infrared and electroluminescence (EL), using specialized datasets to train and validate anomaly detection.

Navigation

Go to

- Home
- Model Prediction

Model Information

- Dataset1-2: Binary Classification (IR)
- Dataset1-6: Six-class Classification (IR)
- Dataset2-2: Binary Classification (EL)

Datasets Used

Dataset 1: Infrared Solar Modules Dataset (Primary)

- | Type: Infrared images (IR)
- | Resolution: 24 × 40 pixels
- | Content: 7 classes – including 6 types of anomalies (e.g., Vegetation, Shadowing, Cell, Diode, Cracking, and Offline-Module) and 1 "No-Anomaly" class.
- | Usage: Main dataset for training and evaluating the classification model.
- | Purpose: Helps detect critical faults visible via temperature variations.

Dataset 2: EL PV Dataset (Supplementary)

- | Type: Electroluminescence (EL) images
- | Resolution: 300 × 300 pixels
- | Content: 2 categories – ND (non-defected) and DF (defected).
- | Usage: Supplementary training to enhance robustness and fault coverage.
- | Purpose: Electroluminescence Imaging is used to reveal defects such as micro-cracks, broken cells, and soldering issues in solar panels with high accuracy.

Figure 74. Project Introduction part of Home page

The ‘Model Prediction’ page from Figure 75 to Figure 76 serves as the main operational area of the system, offering a clean and user-friendly interface that allows users to upload images and select appropriate models for fault detection.

Key Features:

- **Image Upload:** Users click the ‘Browse Files’ button to upload images of solar panels in JPG, JPEG, or PNG format, up to 200MB each.
- **Model Selection:** A dropdown menu allows users to choose from different deep learning models for prediction, including:
 - Dataset1-2: Binary classification for infrared (IR) images;
 - Dataset1-6: Six-class classification for infrared (IR) images;
 - Dataset2-2: Binary classification for electroluminescence (EL) images.
- **Prediction:** After uploading an image and choosing a model, click the ‘Predict’ button to run the inference. The system will show the model’s name, image type, classification mode, and predicted class.
- **Clear All:** Users can reset the page by clicking the ‘Clear All’ button.

This page is designed with simplicity and usability in mind, enabling users to easily upload images, run predictions, and quickly obtain solar panel fault detection results.

Figure 75. Overview of model prediction page

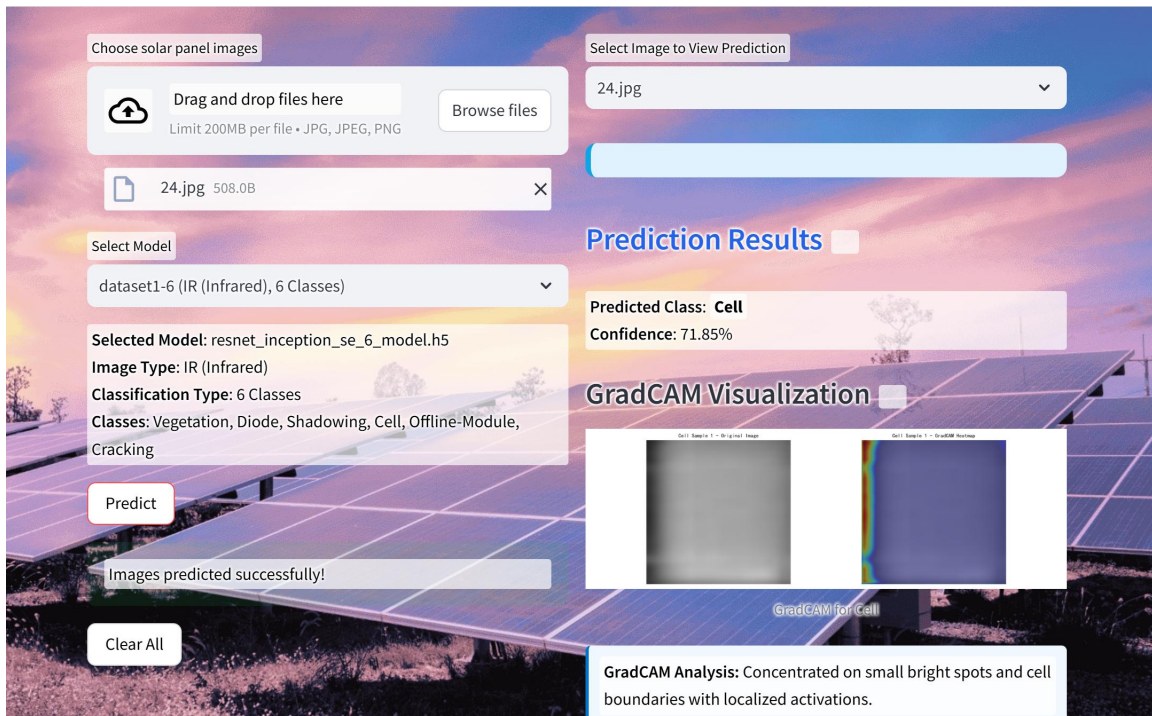


Figure 76. Prediction example

Chapter 5 Professional Issues

5.1 Project Management

The project follows a structured workflow with a clear timeline, using local storage and GitHub for data and code management. Risk analysis and professional considerations support responsible and sustainable execution.

5.1.1 Activities

To fulfill the requirements, the relevant tasks are outlined in the Table 13 below:

Table 13. Relevant Activities

Object	Activities
Research on deep learning models for solar panel fault detection.	<ol style="list-style-type: none">1. Survey Existing Models2. Identify Key Challenges3. Compare Traditional vs. Deep Learning Approaches
Select feasible deep learning models for classifying solar panel fault.	<ol style="list-style-type: none">1. Comparative Analysis of Existing Frameworks.2. Model Select: A CNN model integrates Attention Mechanism.
Gather suitable infrared imaging and Electroluminescence imaging dataset for solar panel fault classify.	<ol style="list-style-type: none">1. Dataset Prepare: Gather datasets from Infrared Solar Modules and ELPV dataset, which both focusing on abnormal classify of solar panel.2. Split dataset into different classes.3. Data Preprocessing: Convert images into a format suitable for deep learning model input.
Develop selected deep learning model.	<ol style="list-style-type: none">1. Model Design: Design the model architecture and determine the model's hyperparameters.
Evaluate the models using statistical techniques.	<ol style="list-style-type: none">1. Data Partitioning: The dataset will divide into a training set (75%) and a

	<p>test set (15%), and 15% is randomly selected from the training set as a validation set.</p> <ol style="list-style-type: none"> 2. Training Model: Using performance Metrics such as precision, recall, and F1 score. 3. Optimize Model: Adjust the model architecture or hyperparameters based on the evaluation results.
Summarize and finishing up	<ol style="list-style-type: none"> 1. Analyze the model's results 2. Suggestions for Improvement 3. Write Project Report and Prepare Presentation

5.2 Schedule

The Gantt chart shows in Figure 77 displaying each activity with deadline:

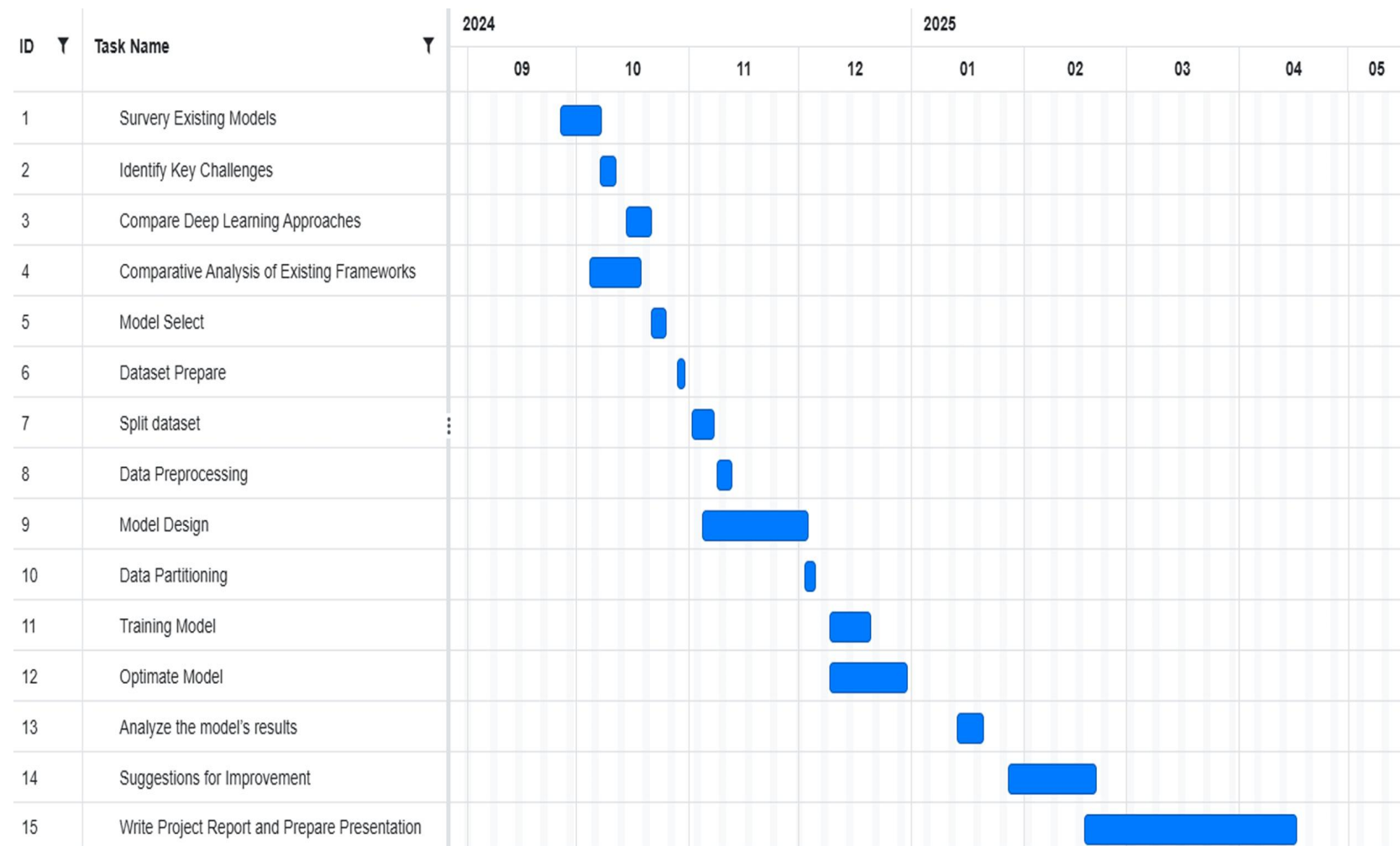


Figure 77. Schedule Plan

5.2.1 Project Data Management

- A. In Figure 78, all deliverables, except for code, will be saved locally and uploaded to Baidu Drive.
- B. Using Zotero to manage references, save all pdf files in a local folder.
- C. Upload the project codes on GitHub.

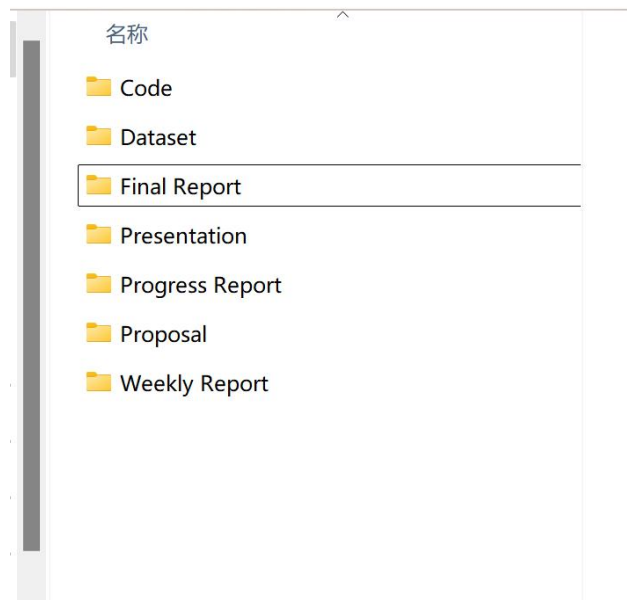


Figure 78. The local folder structure

5.2.2 Project Deliverables

- A. The project proposal
- B. Progress report
- C. Final project report
- D. Project codes
- E. Project presentation

5.3 Risk Analysis

Table 14 displays the analyzed risks during the project progress:

Table 14. Risk Analysis

Risk ID	Potential Risk	Cause ID	Potential Causes	Severity	Likelihood	Risk	Mitigation ID	Mitigation
R1.1	Data acquisition and quality risk	C.1.1.1	Difficulty in obtaining sufficient infrared imaging and EI data	4	3	12	M1.1.1	Utilize publicly available datasets or generate synthetic data through simulation to increase data volume.
		C.1.1.2	The data may contain noise or be inaccurate.	4	3	12	M1.1.2	Implement strict data preprocessing steps, including denoising and data validation, to improve data quality.
		C.1.1.3	The data of abnormal and normal solar panels may be unbalanced.	3	3	9	M1.1.3	Use data augmentation techniques or apply sampling strategies in model training to balance data.
R1.2	Model overfitting risk	C1.2.1	The model may perform well on training data, but have poor generalization ability on new data.	4	3	12	M1.2.1	Use cross validation, regularization techniques, and early stopping methods to avoid overfitting.
R1.3	Risk of insufficient computing resources	C1.3.1	Deep learning models may require a significant amount of computational resources.	3	2	6	M1.3.1	Optimize model architecture to reduce computing requirements, or use cloud services to obtain more computing resources
R1.4	Missed deadline	C1.4.1	Illness	1	3	3	M1.4.1	Register exceptional circumstances if ill.
		C1.4.2	Cannot choose topic	1	1	1	M1.4.2	Conduct research early and meet supervisor
		C1.4.3	Poor time management	4	3	12	M1.4.3	Make a Gantt plan early
R1.5	Software Bugs	C.1.5.1	Virtual Environment Errors	1	1	1	M1.5.1	Keep the virtual environment clean and do not change any unfamiliar files of the tool
R1.6	Loss of data	C1.6.1	Poor version control	4	4	16	M1.6.1	Implement version control strategy at start.

5.4 Professional Issues

In the development of a deep learning model for classifying anomalies in solar panels using infrared imaging and Electroluminescence Imaging (EI) data, several legal, social, ethical, and environmental considerations must be addressed to ensure responsible and sustainable outcomes.

5.4.1 Legal Issues

Legal issues primarily involve data privacy, intellectual property, and liability. If the data contains identifiable information, compliance with regulations such as GDPR is critical. Data used must be ethically sourced, respecting ownership rights and licensing agreements. Misclassification of faults could lead to operational or financial losses, raising the need for clearly defined accountability and transparent model performance to mitigate liability risks [33].

5.4.2 Social Issues

Social issues relate to the project's societal impact, including energy equity and job displacement. By improving solar panel efficiency, the project contributes to affordable and clean energy, aligning with UN Sustainable Development Goals. However, automation could replace manual inspection roles, emphasizing the importance of reskilling workers to collaborate with AI systems. Additionally, ensuring accessibility of the technology to small-scale solar energy users will prevent widening the technology gap and promote inclusive benefits [34].

5.4.3 Ethical Issues

Ethical issues focus on fairness, transparency, and responsible data usage. Biased datasets can compromise model fairness, violating the BCS Code of Conduct principle of inclusivity. Ensuring model transparency and explainability builds trust and accountability, adhering to ACM's Code of Ethics. Ethical considerations also extend to the responsible use of data, avoiding exploitation of proprietary or confidential information [35].

5.4.4 Environment Issues

Environmental issues underscore the project's role in supporting renewable energy and sustainability. By enhancing fault detection, the model helps improve solar panel efficiency, extend their lifespan, and reduce electronic waste(e-waste). This directly supports broader climate goals. However, the energy-intensive nature of training deep learning models must be addressed through optimized algorithms and the adoption of green computing practices to minimize environmental impact [35].

In summary, this project adheres to professional codes of conduct, such as the BCS Code and the ACM Code of Ethics, by emphasizing public interest, ethical responsibility, and sustainable practices. By addressing legal, social, ethical, and environmental concerns, the model aims to make a meaningful contribution to renewable energy advancements while maintaining fairness, transparency, and societal well-being.

Chapter 6 Conclusion

In this project, a deep learning-based solar panel fault detection system was developed and evaluated using two datasets: an infrared (IR) dataset and the ELPV electroluminescence (EL) dataset. The system employs a custom CNN with attention mechanisms for both binary and multi-class classification. Designed to handle low-and high-resolution images efficiently, the proposed SARNet model delivers accurate anomaly detection with strong deployment potential. On the Dataset 1 (IR) binary classification task, it reached an accuracy of 91.7%, precision of 94.2%, and an F1-score of 91.4%, demonstrating its strong ability to distinguish between normal and faulty panels. In the six-class classification task using the same dataset, the model achieved an accuracy of 81.63% and a consistent F1-score and precision of approximately 81.6%, reflecting its robustness in identifying diverse fault types such as cracks, diode issues, and vegetation. On the Dataset 2 (ELPV) binary classification task, the model maintained solid performance with an accuracy of 89.1% and F1-score values of 87.2%, showing its adaptability to different image modalities and fault patterns. The model's architecture was optimized to balance performance with computational efficiency, enabling faster inference without sacrificing accuracy. The user-oriented web-based GUI further enhances accessibility, allowing real-time prediction through simple image uploads, thus bridging the gap between deep learning research and field applications.

While the model performs well in both binary and multi-class classification scenarios, there remains room for further refinement. The primary limitation of the current model is its reduced precision in detecting faults with subtle or overlapping visual characteristics, particularly in categories such as Cracking and Vegetation. These faults often share similar visual patterns, making them difficult to distinguish. Additionally, the dataset suffers from annotation noise and inconsistent labeling, which may compromise model accuracy and generalization. This issue is especially problematic for the model's performance in fault detection across diverse real-world conditions. Furthermore, the absence of paired multimodal samples, such as aligned infrared (IR) and electroluminescence (EL) images, hinders the model's ability to exploit complementary features from both imaging modalities, preventing the model from fully benefiting from the combined insights they could provide for more accurate fault detection.

Future work will focus on improving model accuracy by implementing multi-label and refined classification techniques to better handle overlapping fault categories. To address annotation noise and inconsistent labeling, semi-supervised learning will be explored, along with refining the labeling process for greater reliability. Additionally, aligning infrared (IR) and electroluminescence (EL) images will be prioritized to enable true multimodal learning, allowing the model to benefit from both modalities simultaneously. Developing time-efficient models for industrial applications will also be key, ensuring the model's effectiveness while reducing computational overhead. Real-world validation through field testing and the use of drone-captured IR or EL images will be essential for validating generalization and enhancing the model's applicability in dynamic environments, promoting automated and reliable solar panel maintenance strategies.

References

- [1] Z. B. Duranay, 'Fault Detection in Solar Energy Systems: A Deep Learning Approach', *Electronics*, vol. 12, no. 21, Art. no. 21, Jan. 2023, doi: 10.3390/electronics12214397.
- [2] M. K. H. Rabaia *et al.*, 'Environmental impacts of solar energy systems: A review', *Sci. Total Environ.*, vol. 754, p. 141989, Feb. 2021, doi: 10.1016/j.scitotenv.2020.141989.
- [3] S. H. Han, T. Rahim, and S. Y. Shin, 'Detection of Faults in Solar Panels Using Deep Learning', in *2021 International Conference on Electronics, Information, and Communication (ICEIC)*, Jan. 2021, pp. 1–4. doi: 10.1109/ICEIC51217.2021.9369744.
- [4] R. Al-Mashhadani *et al.*, 'Deep Learning Methods for Solar Fault Detection and Classification: A Review', *Inf. Sci. Lett.*, vol. 10, p. 323, May 2021, doi: 10.18576/isl/100213.
- [5] S. Jaybhaye, V. Sirvi, S. Srivastava, V. Loya, V. Gujarathi, and M. D. Jaybhaye, 'Classification and Early Detection of Solar Panel Faults with Deep Neural Network Using Aerial and Electroluminescence Images', *J. Fail. Anal. Prev.*, vol. 24, no. 4, pp. 1746–1758, Aug. 2024, doi: 10.1007/s11668-024-01959-x.
- [6] S. Jaybhaye, O. Thakur, R. Yardi, V. Raut, and A. Raut, 'Solar Panel Damage Detection and Localization of Thermal Images', *J. Fail. Anal. Prev.*, vol. 23, no. 5, pp. 1980–1990, Oct. 2023, doi: 10.1007/s11668-023-01747-z.
- [7] M. Waqar Akram *et al.*, 'Improved outdoor thermography and processing of infrared images for defect detection in PV modules', *Sol. Energy*, vol. 190, pp. 549–560, Sep. 2019, doi: 10.1016/j.solener.2019.08.061.
- [8] S. Gallardo-Saavedra, L. Hernández-Callejo, M. del C. Alonso-García, J. Muñoz-Cruzado-Alba, and J. Ballestín-Fuertes, 'Infrared Thermography for the Detection and Characterization of Photovoltaic Defects: Comparison between Illumination and Dark Conditions', *Sensors*, vol. 20, no. 16, p. 4395, Aug. 2020, doi: 10.3390/s20164395.
- [9] O. K. Segbefia, N. Akhtar, and T. O. Sætre, 'Defects and fault modes of field-aged photovoltaic modules in the Nordics', *Energy Rep.*, vol. 9, pp. 3104–3119, Dec. 2023, doi: 10.1016/j.egyr.2023.01.126.

- [10] Y.-Y. Hong and R. A. Pula, ‘Methods of photovoltaic fault detection and classification: A review’, *Energy Rep.*, vol. 8, pp. 5898–5929, Nov. 2022, doi: 10.1016/j.egyr.2022.04.043.
- [11] H. Bhatia, ‘10 Causes of Solar Panel Damage and How to Avoid Them’, Sustvest Blog. Accessed: Mar. 11, 2025. [Online]. Available: <https://blog.sustvest.com/solar-panel-damage/>
- [12] M. Cubukcu and A. Akanalci, ‘Real-time inspection and determination methods of faults on photovoltaic power systems by thermal imaging in Turkey’, *Renew. Energy*, vol. 147, pp. 1231–1238, Mar. 2020, doi: 10.1016/j.renene.2019.09.075.
- [13] A. Triki-Lahiani, A. Bennani-Ben Abdelghani, and I. Slama-Belkhodja, ‘Fault detection and monitoring systems for photovoltaic installations: A review’, *Renew. Sustain. Energy Rev.*, vol. 82, pp. 2680–2692, Feb. 2018, doi: 10.1016/j.rser.2017.09.101.
- [14] S. R. Madeti and S. N. Singh, ‘Modeling of PV system based on experimental data for fault detection using kNN method’, *Sol. Energy*, vol. 173, pp. 139–151, Oct. 2018, doi: 10.1016/j.solener.2018.07.038.
- [15] S. S. Madani, A. Abbaspour, M. Beiraghi, P. Z. Dehkordi, and A. M. Ranjbar, ‘Islanding detection for PV and DFIG using decision tree and AdaBoost algorithm’, in *2012 3rd IEEE PES Innovative Smart Grid Technologies Europe (ISGT Europe)*, Oct. 2012, pp. 1–8. doi: 10.1109/ISGTEurope.2012.6465818.
- [16] K. Dhibi *et al.*, ‘Reduced Kernel Random Forest Technique for Fault Detection and Classification in Grid-Tied PV Systems’, *IEEE J. Photovolt.*, vol. 10, no. 6, pp. 1864–1871, Nov. 2020, doi: 10.1109/JPHOTOV.2020.3011068.
- [17] Z. Yi and A. H. Etemadi, ‘A novel detection algorithm for Line-to-Line faults in Photovoltaic (PV) arrays based on support vector machine (SVM)’, in *2016 IEEE Power and Energy Society General Meeting (PESGM)*, Jul. 2016, pp. 1–4. doi: 10.1109/PESGM.2016.7742026.
- [18] R. H. Fonseca Alves, G. A. de Deus Júnior, E. G. Marra, and R. P. Lemos, ‘Automatic fault classification in photovoltaic modules using Convolutional Neural Networks’, *Renew. Energy*, vol. 179, pp. 502–516, Dec. 2021, doi: 10.1016/j.renene.2021.07.070.

- [19] M. Le, V. S. Luong, D. K. Nguyen, V.-D. Dao, N. H. Vu, and H. H. T. Vu, 'Remote anomaly detection and classification of solar photovoltaic modules based on deep neural network', *Sustain. Energy Technol. Assess.*, vol. 48, p. 101545, Dec. 2021, doi: 10.1016/j.seta.2021.101545.
- [20] D. Korkmaz and H. Acikgoz, 'An efficient fault classification method in solar photovoltaic modules using transfer learning and multi-scale convolutional neural network', *Eng. Appl. Artif. Intell.*, vol. 113, p. 104959, Aug. 2022, doi: 10.1016/j.engappai.2022.104959.
- [21] H. Lee, Y. Park, and J. Yi, 'Enhancing Defective Solar Panel Detection with Attention-Guided Statistical Features Using Pre-Trained Neural Networks', in *2024 IEEE International Conference on Big Data and Smart Computing (BigComp)*, Feb. 2024, pp. 219–225. doi: 10.1109/BigComp60711.2024.00042.
- [22] Z. Liu, J. Gui, and H. Luo, 'Good Helper Is around You: Attention-Driven Masked Image Modeling', *Proc. AAAI Conf. Artif. Intell.*, vol. 37, no. 2, Art. no. 2, Jun. 2023, doi: 10.1609/aaai.v37i2.25269.
- [23] H. Zhang, Z. Yang, and N. Lei, 'Defect recognition of solar panel in EfficientNet-B3 network based on CBAM attention mechanism', in *Proceedings of the 2024 International Conference on Generative Artificial Intelligence and Information Security*, in GAIIS '24. New York, NY, USA: Association for Computing Machinery, Jul. 2024, pp. 349–352. doi: 10.1145/3665348.3665407.
- [24] A. Rico Espinosa, M. Bressan, and L. F. Giraldo, 'Failure signature classification in solar photovoltaic plants using RGB images and convolutional neural networks', *Renew. Energy*, vol. 162, pp. 249–256, Dec. 2020, doi: 10.1016/j.renene.2020.07.154.
- [25] S. Deitsch *et al.*, 'Automatic classification of defective photovoltaic module cells in electroluminescence images', *Sol. Energy*, vol. 185, pp. 455–468, Jun. 2019, doi: 10.1016/j.solener.2019.02.067.
- [26] U. Otamendi, I. Martinez, M. Quartulli, I. G. Olaizola, E. Viles, and W. Cambarau, 'Segmentation of cell-level anomalies in electroluminescence images of photovoltaic modules', *Sol. Energy*, vol. 220, pp. 914–926, May 2021, doi: 10.1016/j.solener.2021.03.058.

- [27] Y. Park, M. J. Kim, U. Gim, and J. Yi, ‘Boost-Up Efficiency of Defective Solar Panel Detection With Pre-Trained Attention Recycling’, *IEEE Trans. Ind. Appl.*, vol. 59, no. 3, pp. 3110–3120, May 2023, doi: 10.1109/TIA.2023.3255227.
- [28] R. Rahimzadeh, T. Brox, and J. Steinmetz, ‘State-of-the-art deep learning anomaly detection method for analyzing electroluminescence images of solar cells’, *AIP Conf. Proc.*, vol. 2826, no. 1, p. 060002, Jun. 2023, doi: 10.1063/5.0141116.
- [29] ‘Infrared Solar Modules’. Accessed: Dec. 18, 2024. [Online]. Available: <https://www.kaggle.com/datasets/marcosgabriel/infrared-solar-modules>
- [30] ‘Papers with Code - ELPV Dataset’. Accessed: Apr. 07, 2025. [Online]. Available: <https://paperswithcode.com/dataset/elpv>
- [31] J. Hu, L. Shen, S. Albanie, G. Sun, and E. Wu, ‘Squeeze-and-Excitation Networks’, May 16, 2019, *arXiv*: arXiv:1709.01507. doi: 10.48550/arXiv.1709.01507.
- [32] ‘Multilayer Grad-CAM: An effective tool towards explainable deep neural networks for intelligent fault diagnosis’, *J. Manuf. Syst.*, vol. 69, pp. 20–30, Aug. 2023, doi: 10.1016/j.jmsy.2023.05.027.
- [33] ‘Bridging the gap: Reintegrating legal perspectives into project management’, *Proj. Leadersh. Soc.*, vol. 5, p. 100154, Dec. 2024, doi: 10.1016/j.plas.2024.100154.
- [34] R. Wagner, ‘Projects and Project Management from a Social Perspective’, no. 1, 2022.
- [35] ‘Ethics in Project Management: Integrity and Accountability | IPM’. Accessed: Apr. 13, 2025. [Online]. Available: <https://institute-projectmanagement.com/blog/project-management-ethics-importance-of-integrity-and-accountability/>